Damping of Smart Systems by Shape Memory Alloys (SMAs)

Zur Erlangung des akademischen Grades eines

Doktors der Ingenieurwissenschaften (Dr.-Ing.)

von der KIT- Fakultät für Maschinenbau
des Karlsruher Instituts für Technologie (KIT)
angenommene

Dissertation

von

M.Sc. Kiran Jacob

Tag der mündlichen Prüfung: 17.09.2020

Erster Gutachter: Prof. Dr. Manfred Kohl
Zweiter Gutachter: Prof. Dr.-Ing. Thomas Sattel

This work is licensed under a Creative Commons Attribution-ShareAlike 4.0 International License.

Kurzfassung

Der rapide Fortschritt der mikroelektromechanischen Systeme (MEMS) und das stete Streben in Richtung Miniaturisierung förderten den Einbau zahlreicher elektronischer und mechanischer Komponenten in Kraftfahrzeuge, Maschinen und tragbare Geräte. Der Betrieb elektronischer und mechanischer Komponenten wird durch Vibrationen beeinflusst, die durch den Betrieb von Maschinen, die Bewegung von Fahrzeugen oder Menschen entstehen. Schwingungsdämpfung, -isolierung und -kontrolle sind wesentlich, um die Lebensdauer und Leistung empfindlicher Komponenten zu verbessern. Die meisten der existierenden Dämpfungslösungen und -konzepte sind aufgrund von Scaling-Down-Inkompatibilitäten nicht für Miniaturanwendungen geeignet. In dieser Arbeit wird ein neuartiges Konzept zur Schwingungsdämpfung und -kontrolle von Miniaturgeräten durch Formgedächtnislegierung (Shape Memory Alloy, SMA) vorgestellt.

SMA-Werkstoffe ermöglichen eine große Energiedissipation durch spannungs- oder temperaturinduzierte Phasenumwandlung zwischen Austenit- und Martensitphasen. Die Entwicklung eindimensionaler passiver und aktiver Dämpfer unter Verwendung von SMA-Bauteilen steht im Mittelpunkt dieser Arbeit. Die kaltgewalzten SMA-Folien ermöglichen die Herstellung von Bauelementen durch optische Lithographie mit einem Prozessablauf, der mit der MEMS-Batch-Verarbeitung kompatibel ist. Das Dämpfungsverhalten wird mit Brücken- und Spiralbauelementen unter quasistationären und dynamischen Belastungsbedingungen untersucht. Zur Bewertung des dynamischen Dämpfungsverhaltens des Bauelements wird die Freischwingungsprüfmethode verwendet.

Bei passiven Dämpfungsvorrichtungen zeigt die quasi-stationäre Prüfung eine Vorspannungsabhängigkeit bei der Energiedissipation. Die Energiedissipation folgt einem linearen Zusammenhang mit der Belastungsamplitude, wenn sie im pseudoelastischen Bereich vorgespannt wird. Die passiven Dämpfer unter Verwendung von Brückenvorrichtungen mit Vorspannung über die Länge haben eine maximale spezifische Dämpfungskapazität (SDC) von 72% während des ersten Schwingungszyklus gezeigt. Bei antagonistischem Betrieb passiver Brückenvorrichtungen wird aufgrund der Dissipation unter Be- und Entlastungsbedingungen eine erhöhte SDC von etwa 92% erreicht.

Bei der aktiven Dämpfung wird ein kurzer Heizimpuls verwendet, um das Material von Martensit zu Austenit umzuwandeln. Eine Verbesserung der SDC wird durch die Anwendung des Heizimpulses während der Testbedingung der freien Schwingung beobachtet. Die Brückendämpfervorrichtung mit lateraler Vorspannung hat einen hohen SDC von bis zu 92% unter Massenorientierung in horizontaler Richtung. Im Vergleich

zu einer ähnlichen passiven Dämpfungskonfiguration wird bei der aktiven Brückendämpferanordnung eine Erhöhung des SDC um 20% beobachtet.

Die Ansteuerung der Einweg-SMA wird zur Schwingungskontrolle einer Prüfmasse mit zwei gegenläufigen Aktuatoren genutzt. Der Faltbalkenaktuator mit einer Hublänge von 2 mm stabilisierte die Prüfmasse gegen harmonische Belastung, indem er die Schwingungsamplitude um 83% reduzierte. Die Schwingungskontrolle mit SMA-Aktuatoren ist effektiv bei der optischen Bildstabilisierung, z.B. bei Handkameras, bei denen die Anregung im Bereich von einigen Hz liegt.

Abstract

The rapid progress of microelectromechanical systems (MEMS) and drive towards miniaturization fostered incorporation of numerous electronic and mechanical components in automobiles, machineries and portable devices. The operation of electronic and mechanical components are affected by vibrations arising from the operation of machineries, movement of vehicles or humans. The vibration damping, isolation and control are essential to improve the lifetime and performance of sensitive components. Most of the existing damping solutions and concepts are not suitable for miniature applications due to scaling down incompatibility. In this work, a novel concept for vibration damping and control of miniature devices using Shape Memory Alloy (SMA) is presented.

SMA materials allow large energy dissipation by stress or temperature induced phase transformation between austenitic and martensitic phases. The development of one dimensional passive and active dampers using SMA devices are the focus of this work. The cold-rolled SMA foils allow for fabrication of devices by optical lithography with the process flow compatible with MEMS batch processing. The damping behaviour is investigated using bridge and spiral devices under quasi-stationary and dynamic loading conditions. The free oscillation testing method is used to evaluate the dynamic damping performance of the device.

In passive damper devices, the quasi-stationary testing reveals a pre-strain dependence in energy dissipation. The energy dissipation follows a linear relation with the loading amplitude when pre-strained in the pseudoelastic region. The passive dampers using bridge devices with pre-straining along the length has demonstrated a maximum specific damping capacity (SDC) of 72% during the first cycle of oscillation. An enhanced SDC of about 92% is achieved under antagonistic operation of passive bridge devices owing to the dissipation under loading and unloading condition.

In active damping, a short heating pulse is used to transform the material from martensite to austenite. An enhancement in SDC is observed by the application of heating pulse during free oscillation testing condition. The bridge damper device with lateral pre-straining has high SDC up to 92% under mass orientation along horizontal direction. In comparison with the similar passive damping configuration, an increase of 20% is observed in SDC of active bridge damper device.

The actuation of one-way SMA is exploited for vibration control of a proof mass using two counteracting actuators. The folded beam actuator with a stroke length of 2 mm stabilized the proof mass against harmonic loading by reducing the oscillation amplitude

by 83%. The vibration control using SMA actuators is effective in optical image stabilization, e.g. handheld camera, where the excitation is in the range of a few Hz.

Contents

Kurzfassung i

Abstract iii

Contents v

Publications vii

1 Introduction 1

1.1 Motivation 1
1.2 Objectives 2
1.3 Structure of this Dissertation 3

2 Basic Principles 5

2.1 Types of Vibrations in Single DoF Damper Systems 5
2.1.1 Free Vibration 5
2.1.2 Forced Vibration 7
2.2 Damping Parameters 9
2.3 Types of Damping 10
2.3.1 Internal (Material) Damping 10
2.3.2 Structural Damping 15
2.3.3 Fluid Damping 16
2.4 Vibration Isolators 17
2.5 Damping Parameters 19
2.5.1 Logarithmic Decrement Method 20
2.5.2 Step Response Method 21
2.5.3 Hysteresis Loop Method 21
2.5.4 Magnification Factor Method 22
2.5.5 Bandwidth Method 23
2.6 Shape Memory Alloy (SMA) 24
2.6.1 Martensitic Transformation in NiTi Alloy 25
2.6.2 One-way Shape Memory Effect 27
2.6.3 Pseudoelasticity 28

3 Damping using Smart Materials – State of the Art 29

3.1 Piezoelectric Damping 29
3.2 Magnetostrictive Damping 32
3.3 Electro- and Magneto-Rheological Fluidic Damping 33
3.4 Electro Active Polymer Damping 35
3.5 Shape Memory Alloy (SMA) Damping 37

3.5.1 Pseudoelastic SMA Damping 37
3.5.2 One-way SMA Vibration Control 40
3.5.3 Conclusion 41

4 Material Characterization and Device Fabrication 43

4.1 Pseudoelastic SMA Foil Characterization 43
4.2 One-way SMA Characterization 47
4.3 Device Fabrication 51
4.3.1 Lithography 51
4.3.2 Laser Micromachining 53

5 Pseudoelastic Damper Devices 55

5.1 Strip-based Four Bridge Damper Device 55
5.2 Cross Bridge Damper Device 57
5.2.1 Quasi-Static Behavior of Cross Bridge Damper Device 57
5.2.2 Dynamic Behavior of Cross Bridge Damper Device 60
5.2.3 Conclusion 63
5.3 Bridge Device with Lateral Pre-strain 63
5.3.1 Dynamic Testing of Bridge Damper Device 64
5.4 Spiral Damper Device 67

6 Damping using One-way Shape Memory Alloys 71

6.1 Bridge Device with Lateral Pre-strain 71
6.1.1 Estimation of Cooling Time for Bridge Device 72
6.1.2 Free Oscillation Test Setup 73
6.2 Spiral Device 81
6.2.1 Free Oscillation Testing of Spiral Damper Device 82
6.3 Vibration Control using SMA Strips 84
6.4 Vibration Control using Folded Beam 86
6.4.1 Test-Setup for Folded Beam Device 87
6.5 Scaling Effect on Cooling Time 89
6.5.1 Scaling Effect in Bridge Devices 89
6.5.2 Scaling Effect in Bridge Devices with Short Bridges 90
6.5.3 Scaling Effect in Bridge Devices with Short Bridges and Mass Holder ... 91

7 Conclusions and Outlook 93

7.1 Conclusions 93
7.2 Outlook 95

Acknowledgement 97

Publications

- Jacob K, Ahmadi S, Wendler F, Miyazaki S, Gueltig M, Kohl M. Shape Memory Foil-Based Active Micro Damping for Portable Applications. In 2019 20th International Conference on Solid-State Sensors, Actuators and Microsystems & Eurosensors XXXIII (Transducers & Eurosensors XXXIII), Berlin, Germany. 2019 Jun 23 (pp. 590-593). IEEE. DOI: 10.1109/TRANSDUCERS. 2019.8808494.

- Jacob K, Ahmadi S, Wendler F, Miyazaki S, Kohl M. Vibration Damping of Portable Devices by Pseudoelastic SMA Foils. In ACTUATOR 2018; 16th International Conference on New Actuators, Bremen, Germany. 2018 Jun 25 (pp. 1-5). IEEE. Print ISBN: 978-3-8007-4675-0.

- Ahmadi S, Jacob K, Wendler F, Kohl M. Mesoscale Simulation of Shape Memory Alloy Film Damping. Proceedings in Applied Mathematics and Mechanics" (PAMM) , Munich, Germany. 2018 Dec;18(1):e201800409. DOI:10.1002/ pamm.201800409.

- S. Ahmadi, K. Jacob, F. Wendler and M. Kohl, Shape memory alloy film damping for smart miniature systems, International Journal of Smart and Nano Materials 9:3 (2018) 199-215. DOI:10.1080/19475411.2018.1496953.

1 Introduction

1.1 Motivation

Vibrations are universal phenomena for storage and transfer of energy as emphasized by Albert Einstein in his renounced statement 'Everything in life is vibration'. Depending on the effect of vibration, it could be useful or undesirable. At a cosmic scale, gravitational waves, sound waves and electromagnetic waves reveal crucial information about the evolution of universe and distributes energy which sustains life on Earth. Vibration at atomic scale determines the thermal properties of materials. On the flip side, vibrations introduce energy losses and generate noise like in the case of brake squeal and electric motors. It even reduces the reliability and tool life time by triggering self-excited chatter vibrations in machining processes. Understanding the nature of vibration is crucial in identifying appropriate control measures. The scientific method of treating vibration is initiated by Galileo Galilei in 1602 through his discovery of 'isochronism of the pendulum' also known as 'law of the pendulum'. Since then, there is a huge interest in analytical formulations of vibratory systems. The modern theory of mechanical vibration is based on Lord Rayleigh's theory of sound [1]. In this research, the vibrations under consideration are mechanical vibrations below 10Hz, arising from human hand movements, which affects handheld devices like micro-camera.

The foundation of vibration control is based on the combined effects of stiffness, inertia and damping [2]. Stiffness and inertia are responsible for vibrations while damping reduces amplitude of vibration thereby limiting the transient vibrations. The vibrations impair with operational precision of devices like in telescopes, introduce discomfort like in faulty car suspension and even catastrophic structural failures during earthquakes [3]. Therefore, damping and isolation solutions are essential to protect sensitive devices, equipments or buildings from the vibration environment. Isolators prevent vibrations of machinery from propagating through the mounted surface thereby protecting sensitive devices or equipments in its vicinity. Elastomer mounts, pads and spring mounts are commonly used isolators for electric motors, and engines. On the other hand, dampers dissipate vibrational energy usually as heat like for example hydraulic dampers in automobiles and friction dampers for buildings. The advancements in micro-fabrication technologies and the drive towards miniaturization enhances the mechanical integration at wafer level introducing vibration influences in Micro Electro Mechanical Devices (MEMS). The damping solutions compatible with wafer-level batch processing of MEMS is of unprecedented interest.

The commonly used damping materials like polymers exhibits high damping capacity due to its viscoelastic behaviour and internal defects arising from dislocations, phase boundaries and grain boundaries. The most popular polymer passive damping material – elastomer exhibits a high damping capacity up to 67% [4]. However, elastomers have low specific stiffness and high stroke length requirement for high damping. For dampers at wafer scale, high damping at low strokes are desirable and the fabrication should be compatible with MEMS batch processing.

The category of materials called 'smart materials' capable of reversible alteration of its physical properties in presence of external stimuli is gaining high attention. High energy density, fast response, compact size and fewer moving parts of smart materials favours scaling down to chip scale [5]. The common smart materials are Shape Memory Alloys (SMA), piezoelectric materials, magnetostrictive materials and electro/magneto-rheological fluids [1]. Among them, SMAs show high strain recovery of about 5 to 8% strongly favouring damping applications. The work density of various material categories are shown in Fig 1.0. SMAs have a high actuation stress and strain behaviour with work density of about 10 MJ/m^3. In this work, the passive and active damping behaviour of SMAs are investigated.

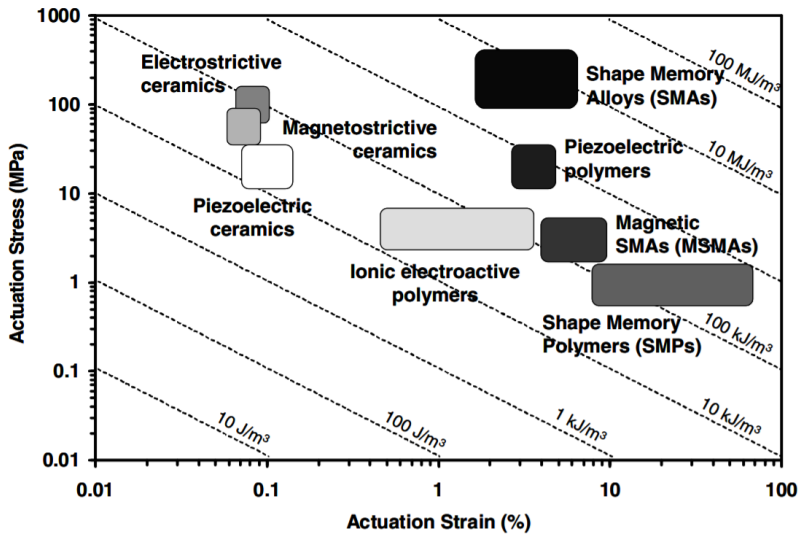

Figure 1.1: Work densities of various material categories. SMAs have a high work density of about 10 MJ/m^3 [6].

1.2 Objectives

The objective of this research is to investigate the damping behaviour of SMA devices using pseudoelastic and one-way SMA foils. The research objective is divided into three major areas of focus: material and device characterization under quasi-stationary test condition, dynamic damping behaviour of SMA damping devices and vibration control

operation of SMA devices. In material characterization, the focus is to identify the material parameters like, critical stresses, elastic modulus, transformation strain, latent heat, Clausius-Clapeyron coefficient and thermal relaxation time constant. Thermomechanical material behaviour is investigated using temperature controlled tensile testing together with infrared thermography and phase transformation is investigated using Differential Scanning Calorimetry (DSC) measurements. The damping behaviour of SMA devices with structures like bridge, spiral and folded beam is investigated under quasi-stationary loading condition to understand the structural dependency to achieve high damping.

The effectiveness of the SMA damper devices is studied under dynamic testing condition using free oscillation experiment. The objective of the experiment is to identify the effect of pre-straining and loading conditions on damping parameters like specific damping capacity (SDC) and damping ratio of SMA damper devices.

In the vibration control operation using SMA devices, the focus is to investigate the effectiveness of SMA devices against mass stabilization under harmonic loading condition. Besides, the operating frequency range and the device design criterion to enhance the mass stabilization are studied.

1.3 Structure of this Dissertation

In the following chapter, the theoretical backgrounds about different types of damping mechanisms and loading conditions are presented. Moreover, the fundamental mechanisms of phase transformation in NiTi based shape memory alloys are also discussed in detail.

In the third chapter, the smart materials used in vibration control are outlined along with their state-of-the-art applications. In the latter part of the chapter, the developments and application prospects of SMA in passive and active vibration control are mentioned.

The fourth chapter contains the characterization of the SMA material used in this work. The thermomechanical material behaviour is investigated for one-way and pseudoelastic SMA and the material parameters are estimated. The fabrication process flow of SMA damper devices are also outlined.

In the fifth chapter, the quasi-stationary behaviour of pseudoelastic damper devices with bridge and spiral structures are described. The dynamic performance of damper devices is evaluated under various pre-straining and loading conditions using free oscillation test setups.

The sixth chapter describes the dynamic performance of one-way SMA damper devices. The damper device behaviour under free oscillation condition is analysed using SDC and

damping ratio. and forced loading situations are presented. The vibration control operation of one-way SMA devices under harmonic loading condition is discussed.

The last chapter consolidates the insights gained from this research and discusses the future prospects of this work.

2 Basic Principles

In this section, the relevant basic information related to the nature of vibration, ways to control vibration and the measurement techniques to characterize the damping performance is explained. Towards the end of the chapter, the mechanism of martensite transformation in NiTi based shape memory alloys is outlined.

2.1 Types of Vibrations in Single DoF Damper Systems

There are different classifications of vibrations depending upon the nature of excitation and response of the damper system towards the excitation. Vibrations could be free or forced vibration, linear or non-linear vibration and deterministic or random vibration[1] [7]. In this research, free vibrations characterize the damping behavior of Shape Memory Alloy (SMA) damper devices.

2.1.1 Free Vibration

Free vibration refers to the movement of mass in a system when no external force is acting on it. The initial displacement of mass introduces loading energy into the system. After release of the mass, the elastic energy in the system leads to oscillations with respect to the equilibrium position. During the oscillation, if there is no loss of energy, it is called an undamped oscillation. On the other hand, if energy is lost while oscillating, it is called a damped oscillation. A second order differential equation is used to represent the free oscillation behaviour of a spring-mass-damper system. A simple spring-mass-damper system is represented in Fig. 2.1. The equation of motion for single DoF system is

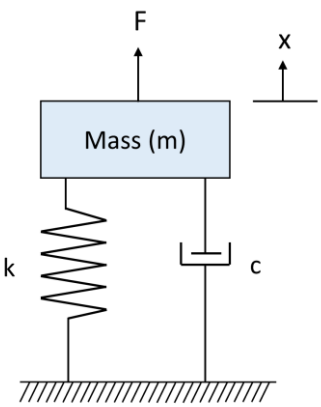

Figure 2.1: A second order spring-mass-damper system.

$$m\ddot{x} + c\dot{x} + kx = 0 \tag{2.1}$$

where, 'x' is the mass displacement, 'k' is the spring constant, 'c' is the damping coefficient.

The solution of Eqn. 2.1 is of the form $x = Ae^{qt}$. The roots of eqn. 2.1 becomes

$$\begin{aligned} q_1 &= -\zeta\omega_n + \omega_n\sqrt{\zeta^2 - 1} \\ q_2 &= -\zeta\omega_n - \omega_n\sqrt{\zeta^2 - 1} \end{aligned} \tag{2.2}$$

where, ω_n is the undamped angular frequency of the system, ζ is called the damping ratio, expressed as $\zeta = \frac{c}{C_c}$. The critical damping coefficient C_c is expressed as $C_c = 2m\omega_n = 2\sqrt{km}$

The nature of oscillation is classified as over damped, critically damped and under damped depending upon the value of ζ.

Case 1: When $\zeta > 1$, the roots in Eqn. 2.2 are real and represents an overdamped system. The response of the system is expressed as

$$x(t) = A_1e^{q_1t} + A_2e^{q_2t} \tag{2.3}$$

$A_1$and A_2 are arbitrary constants. The response of the system is an exponential function as represented by Eqn. 2.3. The high damping in this system results in small net restoring force and moves slowly towards the equilibrium position.

Case 2: When $\zeta = 1$, the roots in Eqn. 2.2 are identical and represents a critically damped system. The response of the system is represented as

$$x(t) = (A_1 + A_2t)e^{-\omega_nt} \tag{2.4}$$

The response of the system shows an exponential behaviour. At critical damping, the system reaches equilibrium at the fastest time without any oscillation.

Case 3: When $\zeta < 1$, the roots in Eqn. 2.2 are complex conjugates and could be expressed as

$$\begin{aligned} q_1 &= -\zeta\omega_n + i\omega_d \\ q_2 &= -\zeta\omega_n - i\omega_d \end{aligned} \tag{2.5}$$

Where ω_d is defined as the damped angular frequency and expressed as $\omega_d = \omega_n\sqrt{1 - \zeta^2}$. Then the response of the system is

$$x(t) = Xe^{-\zeta\omega_nt}\sin(\omega_dt + \phi) \tag{2.6}$$

Here X is the initial loading amplitude. The response consists of two parts: an exponential and an oscillatory part. The oscillations show an exponential decreasing trend depending upon the damping in the system.

2.1.2 Forced Vibration

In forced vibration, the system is subjected to excitation forces that is repetitive in nature. The forced excitation can be introduced by direct excitation on the mass, base excitation or rotor excitation [8]. In the following section, the direct excitation and base excitation systems are explained.

2.1.2.1 Direct Excitation

In direct excitation, a harmonic load is directly applied to the mass of the system as shown in Fig. 2.2 (a). The stationary platform on to which the mass is connected has no contribution to the response of the system. The governing equation of motion for this system could be expressed as [9]

$$m\ddot{x} + c\dot{x} + kx = F_o \sin(\omega t) \tag{2.7}$$

The general solution of Eqn. 2.7 could be expressed as a superposition of two oscillatory functions as

$$x = A_1 \sin(\omega t) + A_2 \sin(\omega t) \tag{2.8}$$

By substituting Eqn. 2.8 in Eqn. 2.7, the expressions for $A_1$and A_2 are obtained as

$$A_1 = \frac{(1-r^2)X_0}{(1-r^2)^2 + (2r\zeta)^2}$$
$$A_2 = \frac{-2r\zeta X_0}{(1-r^2)^2 + (2r\zeta)^2} \tag{2.9}$$

Where, $r = \frac{\omega}{\omega_n}, \zeta = \frac{c}{C_c} = \frac{c}{2m\omega_n}, X_0 = \frac{F_0}{k}$. ω_n is the undamped angular frequency.

The response of the system can be expressed as

$$x = \frac{X_0}{(1-r^2)^2 + (2r\zeta)^2}[(1-r^2)\sin(\omega t) - (2r\zeta)\cos(\omega t)] \tag{2.10}$$

A simplified representation of the response of the system is

$$x = X_0 \beta \sin(\omega t - \psi) \tag{2.11}$$

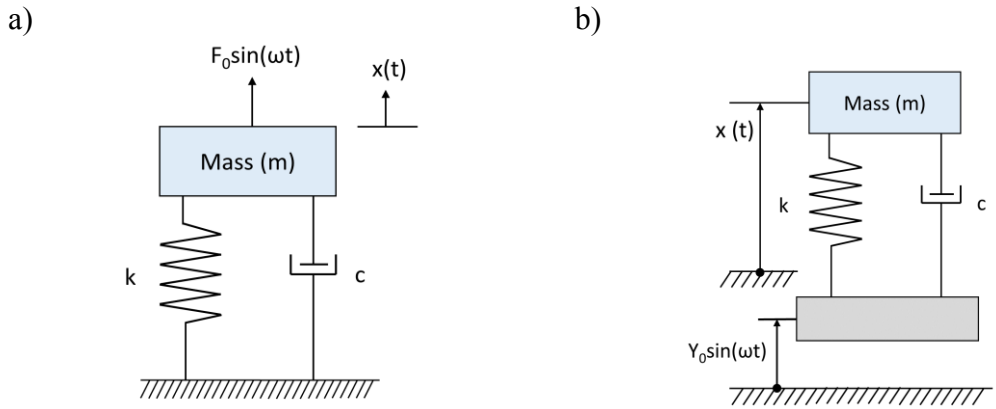

Figure 2.2: Mechanical equivalent of forced loading through direct excitation (a) and base excitation (b).

$$\psi = \tan^{-1}\left(\frac{2r\zeta}{1-r^2}\right)$$
$$\beta = \frac{1}{\sqrt{(1-r^2)^2 + (2r\zeta)^2}} \tag{2.12}$$

where, ψ and β are the phase angle and magnification factor respectively. It could be observed that at resonance ($r = 1$) the response of the system is strongly dependent on the damping ratio. In the absence of any damping, the response of the system tends to infinity at resonance.

2.1.2.2 Base Excited Systems

In the base excited systems, the excitation is applied on the mass through mountings, which could be modelled as a combination of elastic and damping components as shown in Fig. 2.2(b). Base excited systems are relevant for vibration isolation applications. A harmonic excitation (y) is applied to the base of the system and response is analysed by the mass movement (x). The governing differential equation of the system is expressed as

$$m\ddot{x} + c\dot{x} + kx = c\dot{y} + ky \tag{2.13}$$

Since the excitation is harmonic in nature, it can be expressed as $y = Y_0 \sin(\omega t)$. The resulting equation of the system is

$$m\ddot{x} + c\dot{x} + kx = cY_0\omega\cos(\omega t) + kY_0\sin(\omega t) \tag{2.14}$$

The system could be considered as a spring-mass-damper system with two harmonic excitations. The combined response could be obtained by the superposition of individual responses. The steady state solution of the system could be expressed as [9]

$$x = X_0 cos(\omega t - \theta_1 - \theta_2) \tag{2.15}$$

where, X_0, θ_1, θ_2 are

$$X_0 = \omega_n Y_0 \sqrt{\frac{{\omega_n}^2 + (2\zeta\omega)^2}{({\omega_n}^2 - \omega^2)^2 + (2\zeta\omega\omega_n)^2}}$$

$$\theta_1 = \tan^{-1} \frac{2\zeta\omega\omega_n}{{\omega_n}^2 - \omega^2} \tag{2.16}$$

$$\theta_2 = \tan^{-1} \frac{\omega_n}{2\zeta\omega}$$

The transmissibility ratio, defined as $\frac{X_0}{Y_0}$, represents the maximum response of the system to the maximum excitation amplitude. From Eqn. 2.16, the transmissibility ratio is expressed as

$$\frac{X_0}{Y_0} = \sqrt{\frac{1 + (2\zeta r)^2}{(1 - r^2)^2 + (2\zeta r)^2}} \tag{2.17}$$

where, $r = \frac{\omega}{\omega_n}$, ω_n is the undamped angular frequency.

2.2 Damping Parameters

The damping performance of material or system are compared using various damping parameters. The commonly used damping parameters are introduced in this section.

Damping capacity (ΔE): Damping capacity is defined as the energy dissipated per cycle of operation. Damping capacity is measured from the area of hysteresis loop in force-displacement behavior.

$$\Delta E = \oint F dx \tag{2.18}$$

Damping capacity per unit volume (ΔE_v): Damping capacity per unit volume is the area of hysteresis loop in stress-strain behavior.

$$\Delta E_v = \oint \sigma d\varepsilon \tag{2.19}$$

Specific damping capacity (D): Specific damping capacity is defined as the ratio of energy dissipated per cycle to the maximum loading energy (E_{max}) [10].

$$\mathrm{D} = \frac{\Delta E}{E_{max}} \tag{2.20}$$

Loss factor (η): Loss factor is defined as the ratio of specific damping capacity per radian to the maximum loading energy in a cycle.

$$\eta = \frac{\Delta E}{2\pi E_{max}} \tag{2.21}$$

2.3 Types of Damping

Damping is a crucial factor determining the response of a system under external excitation. There are different damping mechanisms which are utilized in the development of dampers. The damping mechanisms are broadly classified as internal (material) damping, structural damping and fluid damping [10].

2.3.1 Internal (Material) Damping

Internal or material damping is the inherent energy dissipation of a material arising from microstructural defects such as impurities, grain boundaries and movement of dislocation. The energy is dissipated by local thermal gradients and eddy currents. In polymers, the energy is dissipated by the movement of polymer chain. The material damping behaviour shows a strong dependence on temperature and frequencies. By modification of molecular structure of materials or introducing additional materials by alloying could enhance the damping behaviour. The material damping is, in general, a combination of various mechanisms at microscopic scale. Therefore, numerous modelling approaches exists to predict the material behaviour depending upon the dominant dissipation mechanism. The general classification of material damping is thermoelastic, viscoelastic and hysteresis damping [10].

2.3.1.1 Thermoelastic Damping

In a homogeneous elastic material, the external loading introduces temperature change in the material. The material undergoes thermal relaxation under isothermal loading condition by the heat exchange with environment. However, under harmonic loading condition at increased loading rates, temperature gradients are observed on the material. This phenomenon increases the entropy, leading to an increase in internal energy thereby reducing the mechanical energy [7,8]. This type of damping mechanism is called

thermoelastic damping. The maximal thermoelastic damping is obtained when the thermal relaxation time is close to the time period of vibration. Thermal relaxation plays a crucial role in the quality factor of MEMS and NEMS resonators. The quality factor of a resonator is the ratio of resonance frequency to the 3dB Bandwidth. The quality factor (also known as Q-factor) of a beam with flexural vibration at angular frequency, ω, is represented by Zener (1938) as [8, 9]

$$Q^{-1} = \frac{\alpha_T^2 TE}{\rho c_p} \frac{\omega \tau_r}{1 + \omega^2 \tau_r^2} \tag{2.22}$$

where, Q is Quality factor, α_T is the coefficient of linear expansion, c_p is the specific heat at constant pressure, E- modulus of elasticity, ρ- density of the material, τ_r is the thermal relaxation time constant expressed as

$$\tau_r = \frac{\rho c_p w^2}{\pi^2 \kappa} \tag{2.23}$$

where, w - width of the beam and κ is the thermal conductivity of the beam.

2.3.1.2 Viscoelastic Damping

Viscoelastic materials exhibit both elastic and viscous characteristics under loading conditions. In elastic material the excitation (stress) and response (strain) are in phase. The governing equation of elastic materials is the Hooke's law. Whereas, a perfect viscous material dissipates the input energy completely, resulting in 90° phase shift between excitation and response. The stress depends on the rate of strain in a viscous material. In viscoelastic material, the material recovers the elastic energy upon unloading while the remaining input energy is dissipated as heat. The phase difference of a viscoelastic materials lies between 0 and 90°. The behaviour of shape memory polymers is predicted using various viscoelastic models [14]. There are different linear viscoelastic models predicting the material behaviour under different stress and strain loading conditions. In Kelvin-Voigt model, the material is represented by a parallel combination of elastic and damping element as shown in Fig. 2.3(a). The stress-strain relation of viscoelastic material is expressed as

$$\sigma = Y_m \varepsilon + \mu \dot{\varepsilon} \tag{2.24}$$

where, Y_m corresponds to modulus of elasticity and μ is the viscosity. Among the elastic and viscous constituents in the stress relation, only the viscous part contributes to damping. Therefore the damping capacity per unit volume (ΔE_v) could be expressed as

$$\Delta E_v = \mu \oint \frac{d\varepsilon}{dt} d\varepsilon \tag{2.25}$$

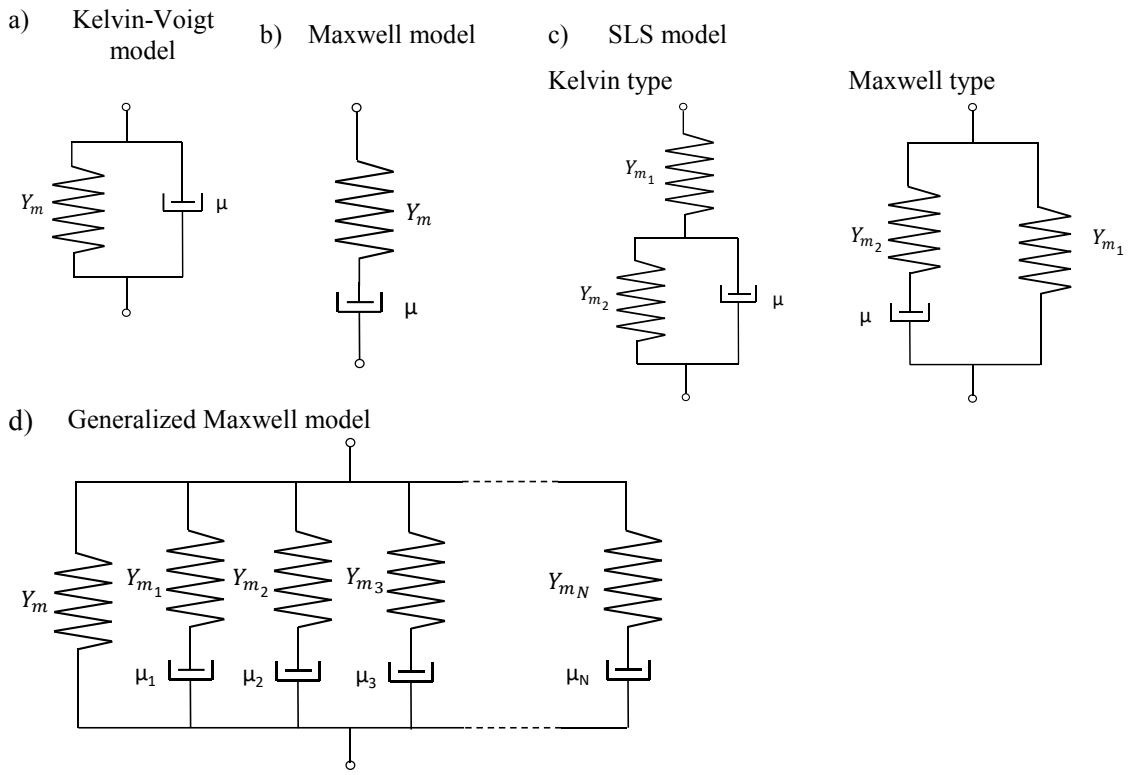

Figure 2.3: Linear viscoelastic models consisting of elastic and damper elements.

For a harmonic loading the strain could be expressed as $\varepsilon = \varepsilon_0 \cos(\omega t)$. So Eqn. 2.25 could be expressed as

$$\Delta E_v = \pi \omega \mu \varepsilon_0^2 \tag{2.26}$$

Therefore, the damping capacity of a viscoelastic material is dependent on the loading frequency. Kelvin-Voigt model accurately predicts the creep mechanism (loading under constant stress condition). However, the stress relaxation of the material under constant strain condition is not accurately represented in this model [10].

In Maxwell model of viscoelasticity, the material is represented as a series elastic and damper elements as shown in Fig. 2.3(b). This model predicts the stress relaxation under constant strain loading condition in viscoelastic materials. However, the creep is not accurately included in this model. The stress-strain relation in this model is formulated as

$$\sigma + \frac{\mu}{Y_m}\dot{\sigma} = \mu \dot{\varepsilon} \tag{2.27}$$

A combination of both Maxwell model and Kelvin-Voigt model called the Standard Linear Solid (SLS) model includes both creep and stress relaxation mechanism. This model is more accurate than the other two models. The equivalent circuit of standard linear solid model is shown in Fig. 2.3(c). The stress-strain relation of standard linear solid model based on Maxwell model and Voigt model are represented by Eqn. 2.28 and Eqn. 2.29 respectively.

$$\sigma + \frac{\mu}{Y_{m_2}}\dot{\sigma} = Y_{m_1}\varepsilon + \frac{\mu(Y_{m_1} + Y_{m_2})}{Y_{m_2}}\dot{\varepsilon} \tag{2.28}$$

$$\sigma + \frac{\mu}{Y_{m_1} + Y_{m_2}}\dot{\sigma} = \frac{Y_{m_1}Y_{m_2}}{Y_{m_1} + Y_{m_2}}\varepsilon + \frac{\mu Y_{m_1}}{Y_{m_1} + Y_{m_2}}\dot{\varepsilon} \tag{2.29}$$

The most general form of viscoelastic model is the generalized Maxwell model indicated in Fig. 2.3(d).The multiple time dependent relaxation mechanism is accounted in this model by parallel arrangement of Maxwell viscoelastic elements. The isolated spring element introduces creep behaviour in the model. Generalized Maxwell model is extended with William-Landel-Ferry equation to describe the time and temperature based behaviour of Shape Memory Polymer materials [15].

2.3.1.3 Hysteretic Damping

Hysteretic damping is a type of material damping where the damping force does not depend upon the frequency of excitation [10, ch.1, pg.4]. Many previous research has observed that in certain frequency ranges the energy dissipation remains almost constant for pseudoelastic shape memory alloy material [16][17]. The energy dissipated in pseudoelastic material is equivalent to an ideal hysteresis loop constructed according to the loading condition [9]. The term 'hysteretic' is apparently a misnomer, since hysteresis is observed in viscoelastic damping as well and energy dissipation is estimated from the enclosed hysteresis loop. However, they differ in their behaviour to cyclic loading. Hysteretic damping is proportional to displacement whereas viscoelastic damping is proportional to velocity [113]. For a harmonic strain excitation, $\varepsilon = \varepsilon_0 \sin(\omega t)$, the stress response leads the strain by an angle, α [6],[18]. The resulting stress is expressed as

$$\sigma = \sigma_0 \sin(\omega t + \alpha)$$

$$\sigma = \sigma_0 \cos(\alpha)\sin(\omega t) + \sigma_0 \sin(\alpha)\sin\left(\omega t + \frac{\pi}{2}\right) \tag{2.30}$$

According to this expression, the stress has two components, one in phase with the loading and the other 90° out of phase with the loading condition. The out-of-phase component is responsible for the damping. So the complex notation of Eqn. 2.30 is expressed as

$$\sigma = \sigma_0 \cos(\alpha)\sin(\omega t) + j\,\sigma_0 \sin(\alpha)\sin(\omega t) \tag{2.31}$$

The complex modulus, $Y_m{}^* = \frac{\sigma}{\varepsilon}$, could be formulated as $Y_m{}^* = Y_m{}' + j\, Y_m{}''$. $Y_m{}'$ is the storage modulus and $Y_m{}''$ is the loss modulus. The hysteretic damping loss factor (η_H) of the material is defined as

$$\eta_H = \tan(\alpha) = \frac{Y_m{}''}{Y_m{}'} \tag{2.32}$$

Accordingly, the complex stiffness of the material is represented as

$$k^* = k(1 + j\,\eta_H) \tag{2.33}$$

So, a general force balance equation of hysteretic damping system is of the form

$$m\ddot{x} + k^* x = 0 \tag{2.34}$$

A hysteretic damping system could be represented by a spring, mass and hysteretic damper as shown in Fig. 2.4. The system is similar to a second order system with spring, mass and damper element. However, the second order equation consisting of the damping force, $c\dot{x}$ as in Eqn. 2.1, is modified as a frequency independent component as $\frac{\mu_H \dot{x}}{\omega}$. The corresponding force balancing equation is of the form

$$m\ddot{x} + \frac{\mu_H \dot{x}}{\omega} + kx = 0 \tag{2.35}$$

Comparing, Eqns. 2.34 and 2.35, a suitable substitution for Eqn. 2.35 is selected as $x = Xe^{j\omega t}$ resulting in the formulation $\dot{x} = j\omega x$. So Eqn. 2.35 is re-written as

$$m\ddot{x} + k\left(1 + j\frac{\mu_H}{k}\right)x = 0 \tag{2.36}$$

Comparing Eqn. 2.33, 2.36 shows that the loss factor, $\eta_H = \frac{\mu_H}{k}$.

The energy dissipated per loading cycle is estimated from $\int F\, dx$, where $F = k^* x$ is the loading force. Under harmonic loading, $x = Xsin(\omega t)$, the force expression from Eqn. 2.33 becomes

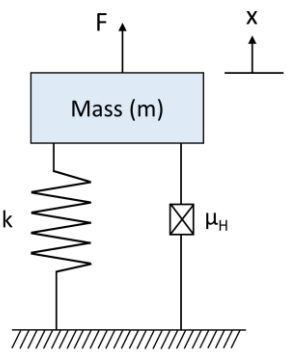

Figure 2.4: Spring-mass-damper model of hysteretic damping.

$$F = kXsin(\omega t) + \eta_H kXcos(\omega t)$$
$$F = kx + \eta_H k\sqrt{X^2 - x^2} \tag{2.37}$$

The energy dissipated per cycle is $\Delta E_H = \int_0^X F dx$

$$\Delta E_H = \pi X^2 \eta_H k \tag{2.38}$$

Fig. 2.5(a) reperesents the stress-strain behaviour of pseudoelastic SMA material and an idealized hysteresis loop constructed for the loading condition. Interestingly, even though there is shape mismatch between these curves, the energy estimated using both these approaches are well matching as shown in Fig. 2.5(b) [9].

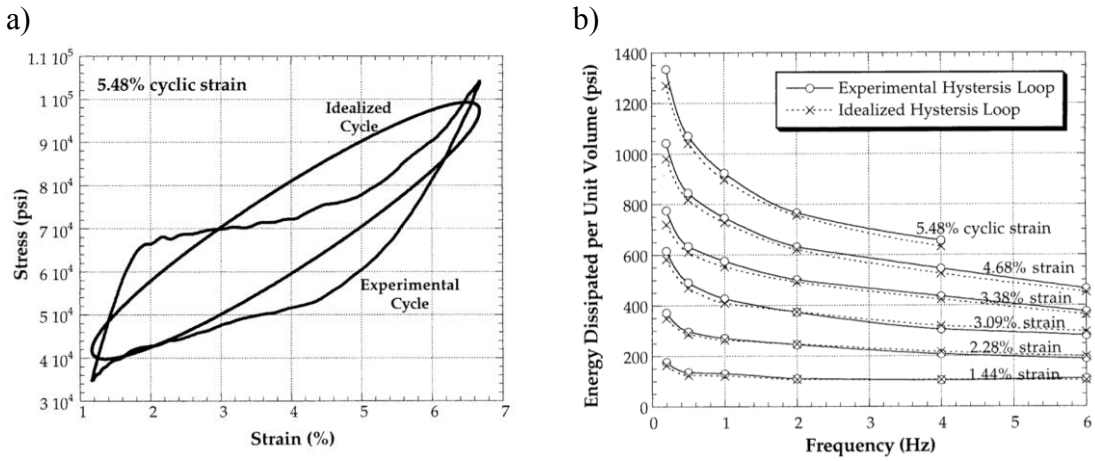

Figure 2.5: Stress-strain behaviour of pseudoelastic SMA material and the idealised hysteresis loop for an identical loading condition is shown in (a). The comparison of energy dissipated per unit volume using experimental hysteresis loop and the idealized hysteresis loop is shown in (b) [9].

2.3.2 Structural Damping

Structural damping is the energy dissipation due to friction arising from relative movement at joints of the mechanical systems or civil structures. Owing to the strong dependence on the nature and type of contact between the mechanical or structural components, a modelling approach requires suitable adaptations based on experimental observations. Moreover, the structural damping depends upon the interface materials, load conditions and aging effects introducing time dependent damping behaviour [10]. The predominant structure damping mechanisms are slip and slide frictions [12]. Energy dissipation by slip friction arises from shear movements in structural joints. Sliding friction, also known as dry friction, exists at relative movement of surfaces. Coulomb friction model is an approach used to model the energy dissipation by sliding friction. In

coulomb damping, the amplitude decay in a free oscillation test condition follows a linear behaviour and could settle down to an equilibrium position different from the starting position.

A typical structural damping encloses large hysteresis as shown in Fig. 2.6(a). The damping behaviour is modelled using idealized Coulomb sliding friction model as indicated in Fig. 2.6(b). Coulomb friction model is a basic model predicting the temperature distribution in bearings [19]. In this model, the force (F) – relative displacement (x) behaviour could be expressed as

$$F = c\ sgn(\dot{x}) \tag{2.39}$$

c is the friction parameter, sgn is the signum function defined as

$$sgn(r) = \begin{cases} 1 & r \geq 0 \\ -1 & r < 0 \end{cases} \tag{2.40}$$

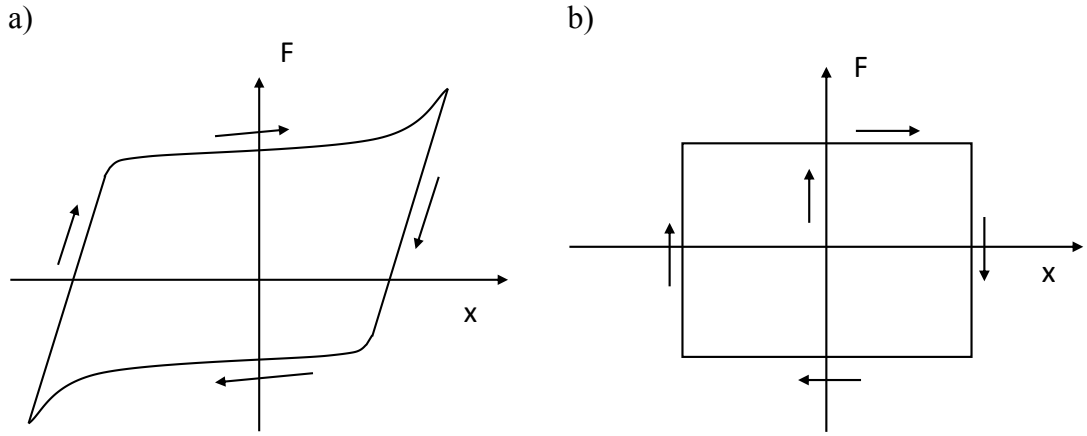

Figure 2.6: The force-displacement behaviour of a system with structural damping (a) and its equivalent model [10].

2.3.3 Fluid Damping

The movement of a body or system in a fluid medium experiences a drag force resulting in energy dissipation. For a body moving in fluid medium along y-direction, as shown in Fig. 2.7(a), experiences a drag force. Consequently, the body experiences movement in x and z directions. The force of damping is

$$F = \frac{D\rho\dot{q}^2\ sgn(\dot{q})}{2} \tag{2.41}$$

$\dot{q} = \frac{\partial q(x,z,t)}{\partial t}$ is the time dependent relative velocity along x and z directions, ρ is the density of the fluid, D is the drag coefficient which depends on Reynold's number and cross sectional dimension. The drag force arises from the viscous effects at the boundary and turbulent effects at the wake as indicated in Fig. 2.7(b) [10].

The damping capacity per unit volume could be expressed as

$$\Delta E_v = \frac{\oint \int_0^{L_x} \int_0^{L_z} f \; dz \, dx \, dq \; (x, z, t)}{L_x L_z q_0} \tag{2.42}$$

L_x, L_z are the cross-sectional dimensions along x and z directions, q_0 is the normalized relative displacement parameter.

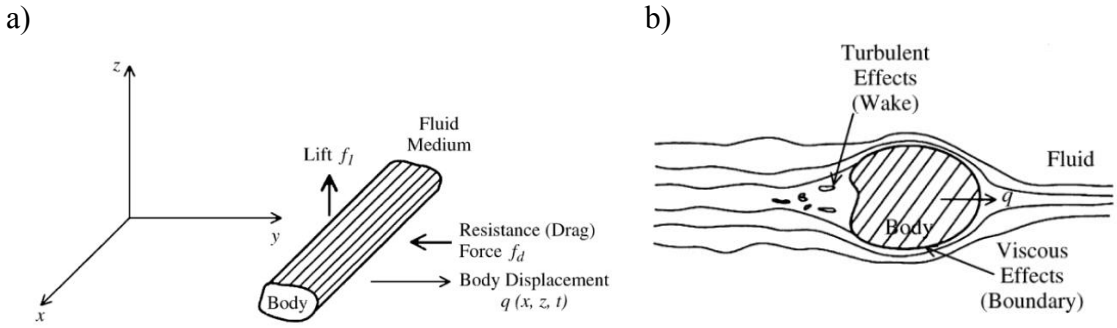

Figure 2.7: A schematic of body moving along y-direction in a fluid experiences a drag force resulting in relative movements along y, z directions (a). The turbulent and viscous effects are responsible for the drag force (b) [10].

2.4 Vibration Isolators

Vibration isolators protect a sensitive system from external disturbances by reducing the transmission of vibration from the source of vibration. The behavior of an isolator is evaluated based on its transfer function which is termed as the transmissibility. Transmissibility is expressed as the ratio of response to excitation. Depending upon the source of vibration either force or displacement transmissibility is used to evaluate the performance of an isolator. If the vibration originating from an equipment is transmitted to the foundation, then force transmissibility of isolator represents the effectiveness of the isolator whereas displacement transmissibility is used when the vibration is arising from the foundation and transmitted to the equipment.

In force isolation, an isolated system is attached to a non-movable support structure and the vibration force is applied from the source through an isolator as indicated in Fig. 2.8(a). The transmissibility is expressed using the force transmissibility ratio as [10, ch.7, pg. 8]

$$T_f = \frac{f_s}{f} = \frac{1 + j\,2\zeta r}{1 - r^2 + j\,2\zeta r} \tag{2.43}$$

In motion isolation, the movement of the movable base platform introduces vibratory motion to the isolated system. The isolator is mounted to the source and force is directly coupled to the isolated system forming a series combination of systems. The motion transmissibility ratio of this isolated system is [10, ch.7, pg. 8]

$$T_m = \frac{Y}{X} = \frac{1 + j\,2\zeta r}{1 - r^2 + j\,2\zeta r} \tag{2.44}$$

Comparing Eqns. 2.43 and 2.45, the transmissibility ratios ($T_m = T_f = T$) are identical. So the transmissibility ratio for force and motion isolation systems is of the form

$$T = \frac{k + jc\omega}{k - m\omega^2 + jc\omega} \tag{2.45}$$

where $\omega_n = \sqrt{k/m}$, $\zeta = \frac{b}{2\sqrt{km}}$, $r = \frac{\omega}{\omega_n}$

The magnitude of transmissibility ratio from Eqn. 2.45 is

$$|T| = \sqrt{\frac{1 + 4\zeta^2 r^2}{(1 - r^2)^2 + 4\zeta^2 r^2}} \tag{2.46}$$

The behavior of transmissibility (T) as a function of normalized angular frequency, r, is indicated in Fig. 2.9. The transmissibility is greater that unity when the $r < \sqrt{2}$. This region is called the region of amplification. In this region, the damping ratio, ζ, is crucial

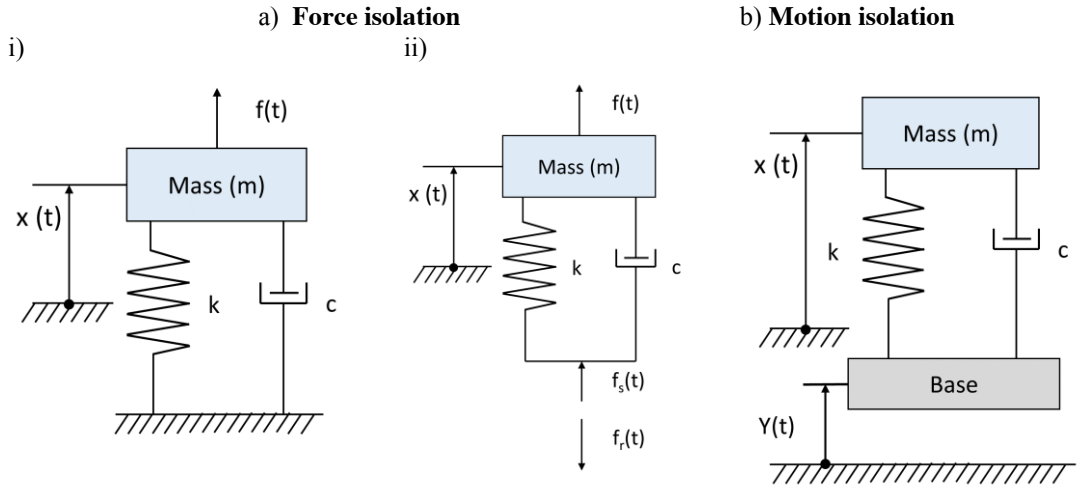

Figure 2.8: (a)(i) Equivalent mechanical representation of force isolation with a loading force f(t). (ii) The force applied on the mass is transmitted ($f_s(t)$) to the fixation resulting in a reaction force $f_r(t)$. (b) The motion isolation system with an excitation Y(t) on the base, results in a mass displacement of x(t).

in determining the response of the system. A low value of ζ drastically increases the transmissibility. Transmissibility is infinite when $\zeta = 0$. When $r > \sqrt{2}$, transmissibility is less than unity. This region is called the region of isolation. Vibration isolators adjust the equivalent system response to operate in this region to achieve a desired level of isolation. In this region, a low damping ratio enables better isolation as observed in Fig. 2.9.

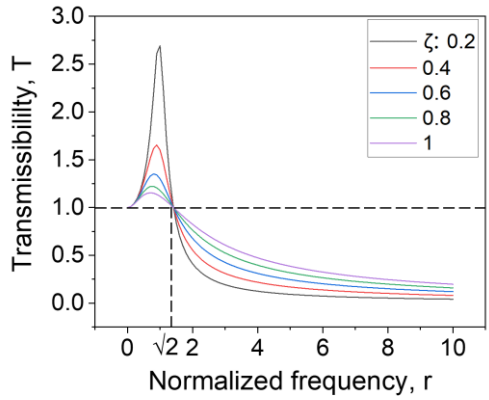

Figure 2.9: The variation of transmissibility (T) with respect to normalized angular frequency (r).

2.5 Damping Parameters

The damping parameters like damping capacity, loss factor, damping ratio and quality factor provides an insight about the damping behavior of material or systems. Modelling the damping behavior requires identification of appropriate damping parameters relevant for the model under consideration. However, the contribution of individual types of damping like material, structural and fluid damping is difficult to estimate from the overall measurement due to the resulting interacting effects of various damping types. The measurement approaches used to estimate the damping parameters are broadly classified according to time and frequency based response of the system. In this section, the common measurement methods to estimate the damping parameters are explained.

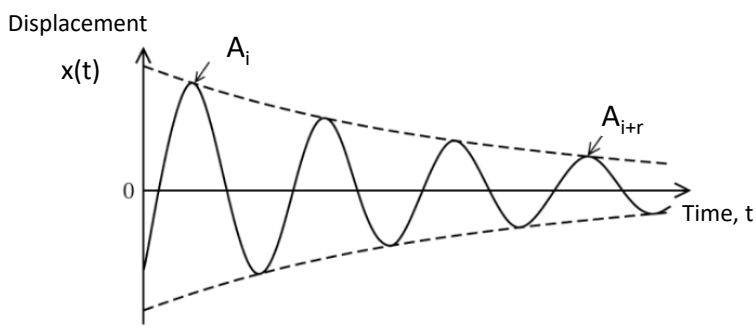

Figure 2.10: The response of the system under impact loading [10].

2.5.1 Logarithmic Decrement Method

Logarithmic decrement is a commonly used time-based response method to estimate the damping parameters of a single degree-of-freedom oscillatory system with low damping. The mass of the system is subjected to free oscillation and the resulting time-based decay of amplitude is utilized to estimate the damping parameters. According to Eqn. 2.6, the oscillation behavior of the system with spring, mass and viscous damper elements is expressed as

$$x(t) = Xe^{-\zeta\omega_n t}\sin(\omega_d t + \phi) \tag{2.47}$$

The response of the system is represented in Fig. 2.10. A_i and A_{i+r} represents the peaks of ith and $(i+r)^{th}$ oscillations respectively. The time difference between the amplitude peaks is $\frac{2\pi r}{\omega_d}$, where ω_d is the damped angular frequency. Their amplitude ratio from Eqn. 2.47 is [10]

$$\frac{A_{i+r}}{A_i} = e^{\left(-\zeta\frac{\omega_n}{\omega_d}2\pi r\right)} \tag{2.48}$$

Since $\omega_d = \omega_n\sqrt{1-\zeta^2}$, the Eqn. 2.48 becomes

$$\frac{A_{i+r}}{A_i} = e^{\left(-\frac{\zeta}{\sqrt{1-\zeta^2}}2\pi r\right)} \tag{2.49}$$

The logarithmic decrement, δ, is [10]

$$\delta = \frac{1}{r}ln\frac{A_i}{A_{i+r}} = \frac{2\pi\zeta}{\sqrt{1-\zeta^2}} \tag{2.50}$$

In the case of low damping, where $\zeta < 0.1$, $\omega_n \approx \omega_d$, logarithmic damping becomes

$$\delta = 2\pi\zeta \tag{2.51}$$

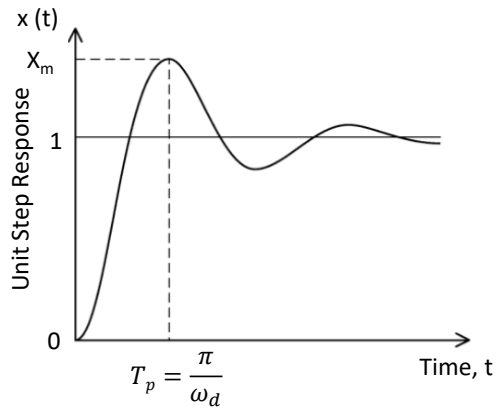

Figure 2.11: Unit step response of the system [10].

$$\zeta = \frac{\delta}{2\pi}$$

2.5.2 Step Response Method

Step response method is a time based measurement to obtain the damping parameter. A step load is applied on a single DoF spring-mass-damper system and the resulting time based response, as indicated in Fig. 2.11, reveals the damping parameters of the system.

The step response of second order system is given by

$$x(t) = 1 - \frac{1}{\sqrt{1-\zeta^2}} e(-\zeta\omega_n t)\sin(\omega_d t + \phi) \tag{2.52}$$

Where, $\phi = \tan^{-1}\left(\frac{\sqrt{1-\zeta^2}}{\zeta}\right)$. The maximum oscillation peak normalized to settling point, X_m, corresponds to

$$X_m = 1 + e(-\zeta\omega_n T_p) = 1 + e\left(-\frac{\pi\zeta}{\sqrt{1-\zeta^2}}\right) \tag{2.53}$$

The damping ratio could be estimated from the peak oscillation amplitude as [10]

$$\zeta = \frac{1}{\sqrt{1 + \frac{1}{\left[\frac{\ln(X_m - 1)}{\pi}\right]^2}}} \tag{2.54}$$

2.5.3 Hysteresis Loop Method

Hysteresis loop method is a time based damping measurement for the estimation of damping capacity, loss factor and damping ratio. The force-displacement behaviour of a damped system encloses a hysteresis loop under cyclic loading condition. The area under the force-displacement hysteresis loop is a measure of energy dissipated in each cycle of operation. In the case of hysteretic damping, the damping capacity is expressed as [10]

$$\Delta E_{vH} = \pi X^2 \mu_H \tag{2.55}$$

X is the maximum loading amplitude. The loss factor (η) is estimated from

$$\eta_H = \frac{\Delta E_{vH}}{2\pi E_{max}} = \frac{\pi X^2 \mu_H}{2\pi \frac{kX^2}{2}} = \frac{\mu_H}{k} \tag{2.56}$$

$E_{max}$is the loading energy. The damping ratio is estimated from (section 2.3.1.3)

$$\zeta_H = \frac{\mu_H}{2k} \tag{2.57}$$

2.5.4 Magnification Factor Method

Magnification factor method is a frequency response based estimation of damping behavior for a system under harmonic loading [10]. Magnification factor is the ratio of displacement under harmonic loading to static loading condition. As mentioned in Eqn. 2.12, the magnification factor is expressed as

$$\beta = \frac{1}{\sqrt{(1-r^2)^2 + (2r\zeta)^2}} \tag{2.58}$$

Here, $r = \frac{\omega}{\omega_n}$ and ω is the angular frequency of the applied harmonic load. The peak value of the magnification factor is attained when the minimum value criterion for denominator is satisfied. It is formulated as

$$\frac{d}{dr}\sqrt{(1-r^2)^2 + (2r\zeta)^2} = 0$$

$$r = \sqrt{1-2\zeta^2} \tag{2.59}$$

$$\omega_r = \sqrt{1-2\zeta^2}\omega_n$$

Here, ω_r is the angular frequency at resonance. The behaviour of magnification factor with frequency is indicated in Fig. 2.12. For low damping conditions ($\zeta < 0.1$),

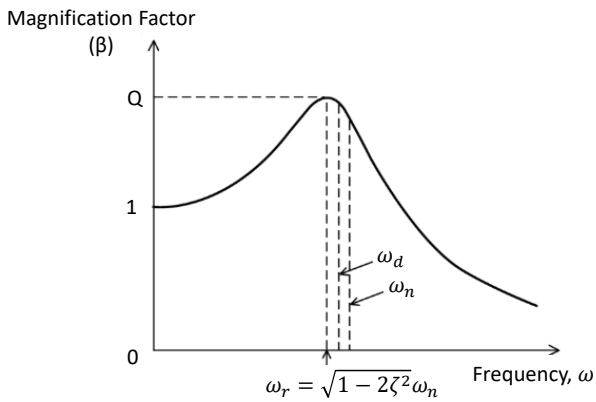

Figure 2.12:Magnification factor method of estimating damping parameter for a single DoF oscillatory system [10].

ω_r, ω_n and ω_d are almost equal. The peak value of magnification factor at resonance called the Quality factor or Q-factor is obtained by substituting resonance criterion in Eqn. 2.58 as

$$Q = \frac{1}{2\zeta\sqrt{1-\zeta^2}} \tag{2.60}$$

In case of low damping condition ($\zeta < 0.1$), Q-factor becomes

$$Q = \frac{1}{2\zeta} \tag{2.61}$$

For a multi DoF system, there would exist multiple peaks in the magnification factor corresponding to modal frequencies if the frequencies are sufficiently separated apart. The damping ratio of individual modes could also be estimated using Eqn. 2.61.

2.5.5 Bandwidth Method

Bandwidth method is a frequency response based damping measurement for a system under harmonic excitation. Similar to the magnification factor method, the behavior of magnification factor with frequency of excitation is utilized to identify the damping ratio of the system. A frequency response of a single DoF linear system with viscous damping is shown in Fig. 2.13. The bandwidth also called the half power region is defined as the frequency range where the magnification factor is above $\frac{Q}{\sqrt{2}}$. The magnification factor at half power point is

$$\frac{1}{\sqrt{(1-r^2)^2+(2r\zeta)^2}} = \frac{1}{\sqrt{2}\,2\zeta}$$
$$r^4 + 2r^2(2\zeta^2-1) + (1-8\zeta^2) = 0 \tag{2.62}$$

Simplifying Eqn. 2.62 with ${r_1}^2$ and ${r_2}^2$as the roots,

$$(r_2 - r_1)^2 = 2(1 - 2\zeta^2) - 2\sqrt{1 - 8\zeta^2} \tag{2.63}$$

For low damping ratio ($\zeta < 0.1$), $\sqrt{1 - 8\zeta^2} \cong 1 - 4\zeta^2$as per Taylor expansion. So Eqn. 2.63 is simplified as

$$r_2 - r_1 \cong 2\zeta$$
$$\Delta\omega = \omega_2 - \omega_1 = 2\zeta\omega_n \tag{2.64}$$

For small damping, $\omega_n$and ω_r are approximately equal. Therefore damping ratio is

$$\zeta = \frac{\Delta\omega}{2\omega_r} \tag{2.65}$$

2.6 Shape Memory Alloy (SMA)

SMAs exhibit the unique property of shape recovery by reversible martensite transformation mechanism. The shape recovery behavior is first observed by Arne Ölander (1938) in cadmium (Cd) - gold (Au) alloy [21]. Chang and Read (1951) performed a detailed analysis of shape recovery by the application of temperature in Au-Cd beta phase [22]. Buehler et.al observed the shape recovery behavior in Nickel (Ni)-Titanium (Ti) alloy in 1963 [23]. Soon after, NiTi based SMAs emerged as a practical material for a variety of applications. The unique properties of NiTi based SMAs are associated with their peculiar martensitic transformation mechanism. Martensitic transformation is a diffusionless transformation involving simultaneous and co-operative movement of atoms accompanied by a macroscopic material deformation. The movement of atoms is within a distance of atomic diameter with occasional shuffling of atoms [24]. The reversible nature of crystal structure in martensite transformation is termed as

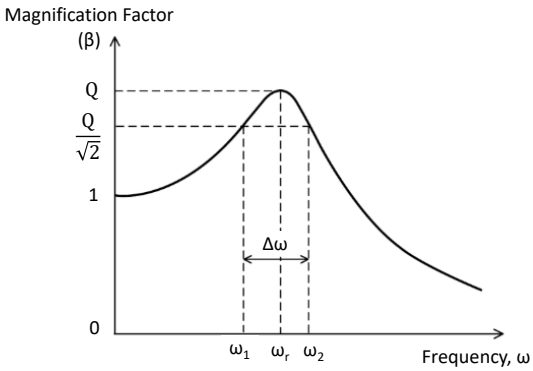

Figure 2.13: Bandwidth method estimation for a single DoF linear viscoelastic system [10].

thermoelastic martensitic transformation. As a consequence of the thermoelastic martensitic transformation, NiTi based SMAs show Shape Memory Effect (SME) where shape recovery occurs upon heating the material above Austenite finish temperature. In contrast to the conventional martensite transformation observed in steel, a smooth phase transformation is observed in NiTi based SMAs resulting in a narrow transformation temperature hysteresis of a few tens of degree Celsius [25]. In this section, the crystallographic aspects of martensite transformation and thermomechanical behavior of NiTi based SMAs are described.

2.6.1 Martensitic Transformation in NiTi Alloy

A fully annealed near equiatomic composition of NiTi alloy has a cubic, CsCl type, B2 parent phase (Austenite) above phase transformation temperature and a monoclinic B19' martensite phase below martensite finish temperatures as indicated in Fig 2.14(a). Depending upon the heat treatment conditions and alloy composition, an intermediate phase called R-phase could arise in the transformation from B2 to B19' [28]. The crystal structure of R-phase is rhombohedral formed by elongation of B2 lattice along <111> direction as indicated in Fig 2.14(b). The appearance of R-phase before reaching B19' is observed in thermo-mechanically treated NiTi alloys, Ni rich NiTi material annealed at low temperatures and addition of tertiary elements like iron (Fe) or Aluminium (Al) [29]–[32]. Consequently, a two-step transformation is observed in the differential scanning calorimetry measurement as indicated in Fig. 2.15. Since the governing mechanism involved between B2 and R-phase is thermoelastic in nature similar to that of martensitic transformation mentioned before, R-phase transformation also exhibits SME and pseudoelasticity [33]. However, the associated strain due to R phase transformation (R→B2) is only about 0.8% in contrast to 10% strain by martensite transformation (B19'→B2) [34], [35].

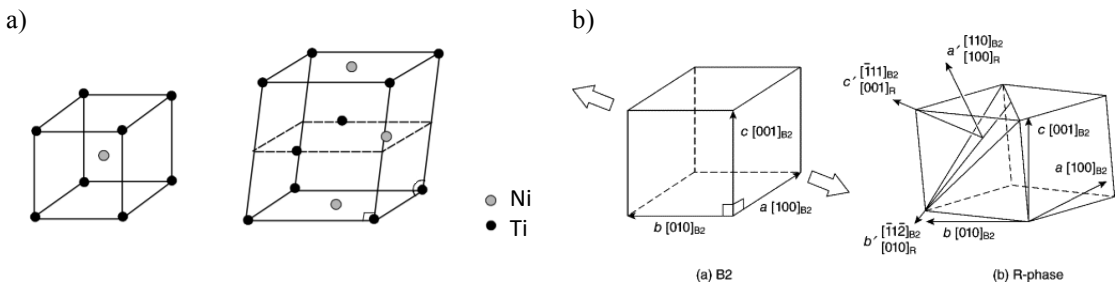

Figure 2.14: The crystal structure of Austenite (B2) and Martensite (B19') phase (a) and the formation of R phase from B2 phase (b) [26], [27].

The mechanism of martensitic transformation is well described by the phenomenological theory of martensite transformation which is based on minimization of strain energy during the transformation. The habit plane that forms the interface between parent phase

and martensitic variant should be undistorted and unrotated to minimize the interface strain energy. As a result, martensite variants experience lattice invariant shear in the form of stacking faults, dislocations or twins [37]–[39]. In SMA, the lattice invariant shear due to twinning is reversible. NiTi SMA shows <011> type II twinning [40]. The total strain (P_1), also known as the shape strain, related to the martensite transformation is expressed in matrix form as [27]

$$P_1 = RP_2B \tag{2.66}$$

where, B is the lattice deformation that give rise to martensite transformation from the parent phase, P_2 is the lattice invariant shear and R is the lattice rotation. Due to the self-accommodation mechanism, the transformation from B2 to B19' occurs without any macroscopic deformation. Therefore a co-existence of multiple martensite variants are essential to accommodate the strains of each variants [41].

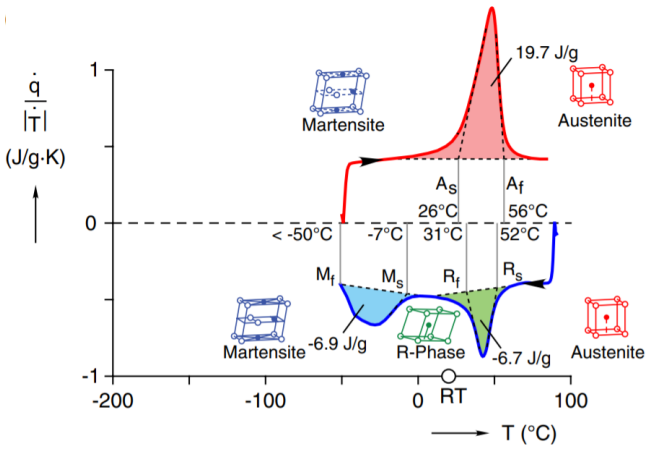

Figure 2.15: Differential scanning calorimetry (DSC) measurement of a Ni-rich NiTi alloy showing two step transformation through an intermediate R phase. A_s- Austenite start temperature, A_f- Austenite finish temperature, R_s- R phase start temperature, R_f- R phase finish temperature, M_s- Martensite start temperature, M_f- Martensite finish temperature [36].

The phase transformation stress varies with the temperature of operation. The stress required to initiate the phase transformation, called the critical stress, shows an increasing trend above martensite start temperature (M_s). The change of stress associated with temperature change satisfies the Clausius Clapeyron relation [27]

$$\frac{d\sigma}{dT} = -\frac{\Delta S}{\varepsilon_t} \tag{2.67}$$

ΔS is the entropy of transformation per unit volume and ε_t is the transformational strain. The transformation strain associated with R phase is signicantly lower than that of martensite transformation as shown in Fig. 2.16. Therefore, the critical stress of R phase increases rapidly with temperature. The critical stresses of martensite and R phase

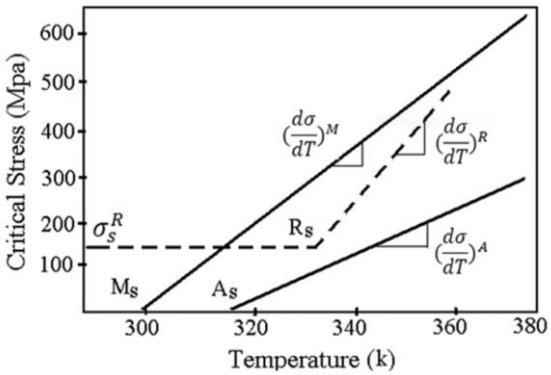

Figure 2.16: Influence of temperature on the critical stress of Austenite (A), Martensite (M) and R phases [42].

intersects at an elevated temperature above which there is a direct transformation between B2 and B19'.

2.6.2 One-way Shape Memory Effect

Shape memory effect (SME) is the phenomenon of temperature-induced shape recovery of SMA when heated above austenite finish temperature (A_f). The thermomechanical behavior of SME is illustrated in Fig. 2.17. At temperatures below A_s, martensite twin

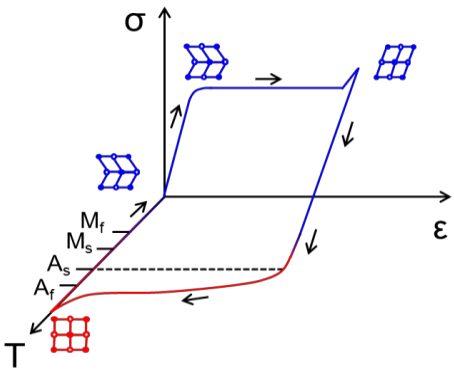

Figure 2.17: Illustration of shape memory effect under thermomechanical loading condition.

variants coexists under stress-free condition. The martensite variants at this condition is collectively known as twinned martensite or unoriented martensite. Under loading condition above critical stress, unoriented martensite begins to transform to a single martensite variant that is most favourable in accordance with the applied stress. The single martensite variant so formed is called the untwinned or oriented martensite. A large strain of about 5 to 8% is associated with the rearrangement from unoriented to oriented martensite. The completion of martensite reorientation is identified by a sudden increase

in the stress loading condition for subsequent deformation. The increase in the stress loading condition represents the initiation of slip deformation. For a reversible operation, the loading condition is restricted before slip deformation. Upon unloading, SMA retains the large plastic deformation. The shape is recovered by heating SMA above A_f transforming martensite to austenite phase. By cooling down below M_f, Austenite transforms to unoriented martensite. SME is exploited in various actuation applications in biomedical, aerospace and automobile industries [43]–[47].

2.6.3 Pseudoelasticity

Pseudoelasticity is phenomenon of stress-induced phase transformation in SMA while operating above austenite finish temperature (A_f) where large loading strain is achieved. The mechanical behavior of pseudoelastic SMA is indicated in Fig. 2.18. SMA is in austenite phase under stress-free condition. SMA behaves elastically until stress reaches

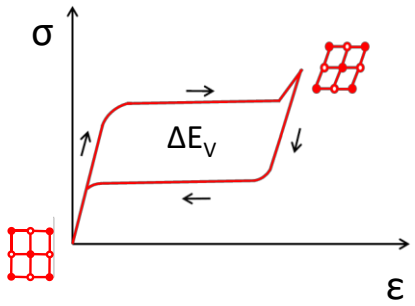

Figure 2.18: Stress-strain behaviour of a pseudoelastic SMA

a critical value. Above the critical stress, the phase transformation from austenite to martensite is initiated. The complete phase transformation occurs without much additional stress loading condition. After the complete transformation to martensite phase, there is a rise in the stress due to slip deformation mechanism. For a reversible operation, the strain levels are restricted below slip deformation. Upon unloading, the material transforms back to austenite showing a hysteretic behavior due to the energy dissipation during phase transformation. The area under the hysteresis loop indicates the damping capacity per unit volume (ΔE_v). Owing to the high load bearing and self-centering capabilities pseudoelastic SMA are used as stents, orthodontic staples in medical applications, flexible frames for eyeglasses and dampers for buildings and bridges [48]–[52].

3 Damping using Smart Materials – State of the Art

'Smart materials' refers to a group of materials that changes one or more physical properties in response to external stimuli such as stress, temperature, humidity, electric and magnetic fields, light or chemical compounds. Smart materials are of high research interest over the last three decades for damping and vibration control applications owing to its adaptive capabilities and large energy dissipation. The tunability of properties in smart materials are exploited in active vibration control applications. The term 'active vibration control' includes active attenuation, active damping and active isolation. Smart materials are widely used for passive, semi-active and active vibration control. In this section, the damping and isolation behavior of commonly used smart materials are discussed.

3.1 Piezoelectric Damping

Piezoelectric materials generate electric charges when stress is applied. These materials also demonstrate inverse piezoelectric effects forming strain under an electric field [53]. The strain generated is about 0.1% [53]. The advantages of piezoelectric materials are precise controllability of strain and high operating frequency (MHz). The common piezoelectric materials are polyvinylidene fluoride (PVDF), lead zirconate titanate (PZT) and barium titanate.

On a vibrating environment, piezoelectric materials convert the mechanical energy to electrical energy. The mechanical energy is dissipated by dissipating electrical energy through a load impedance. The basic operation of piezoelectric material is illustrated in

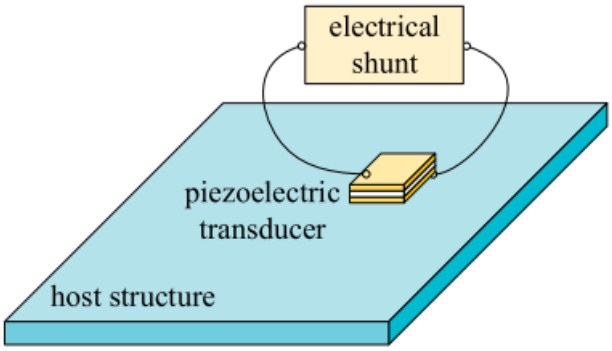

Figure 3.1: Basic operation of piezoelectric shunt damper mechanism [54]. *The vibration of the host structure is converted to electrical energy by piezoelectric transducer and dissipated through the shunt impedance.*

Fig. 3.1. The piezoelectric transducer is mounted on a vibrating host structure where the mechanical deformation of transducer generates electric charges. The corresponding electrical energy is dissipated using an external electrical shunt impedance. This method of vibration damping is called piezoelectric shunt damping. The electrical resonance and mechanical vibration mode are matched for maximum mechanical energy dissipation. A passive electrical shunt uses resistor, capacitor, inductor or diode. In active electrical shunt, external electrical energy is utilized to attain desired level of damping. A wide operating bandwidth and multimode vibration control is achievable in active shunt [54].

The topologies of passive and active electrical shunt damping are shown in Fig 3.2. The dissipation introduced by a simple resistive shunt is similar to very low viscoelastic

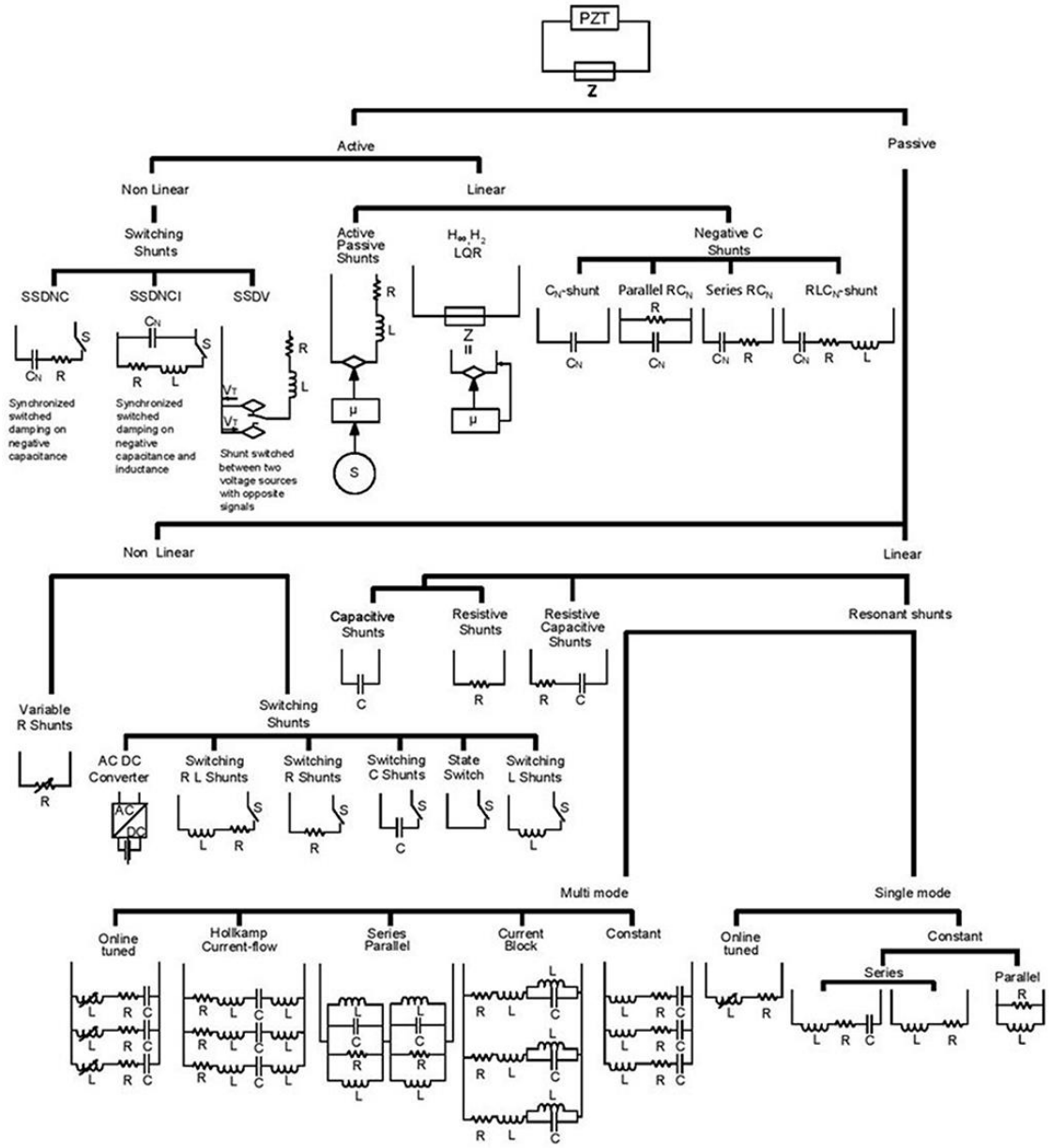

Figure 3.2 : Topologies of Piezoelectric passive and active shunt damping [55].

damping. The combination of resistor with inductor and/or capacitor forms a resonance circuit suitable for single mode and multimode vibration damping. In multimode mechanical vibrations, the electrical resonant shunts should have multiple electrical resonances by suitable combinations of inductors and capacitors. In active electrical shunt, arbitrary impedance is established through externally controlled current and voltage sources [54]. The active shunt impedance is adaptable to structural resonance frequencies enabling wide operation band. The implementation of negative shunt impedance allows for the compensation of internal capacitance of the piezoelectric transducer thereby enhancing the coupling factor, facilitating improved dissipation of mechanical energy across the passive element in electrical shunt [56].

The effectiveness of piezoelectric damping is exploited in many practical/prospective applications. Lim et al. demonstrated vibration control of the spindle of Hard Disk Drive (HDD) using piezoelectric bimorph, as shown in Fig.3.3(a), with electrical shunt of resistor and inductor in series [10,11]. Sun et al. demonstrated improved vibration damping of second, third and fourth modes of the actuator arm of HDD [59]. In dual stage actuator HDD, piezoelectric actuator is used for fine position adjustment, compensating positioning errors on a vibratory environment [60]. The suppression of helicopter rotor vibration using passive/active piezoelectric dampers improves the flight condition, aeromechanical stability and reduces noise [61]. In tapping mode Atomic Force Microscopy (AFM), the scan rate and image quality is enhanced by reducing the sensitivity of cantilever using piezoelectric shunt damping [62]. In space application, the vibration impact on deformable mirror in space telescopes is mitigated by shunting the piezoelectric actuator during launching phase as shown in Fig. 3.3(b). The reflective coating of Aluminium on single crystal silicon acts as the mirror and PZT actuators are used for mirror adjustments after deployment [63].

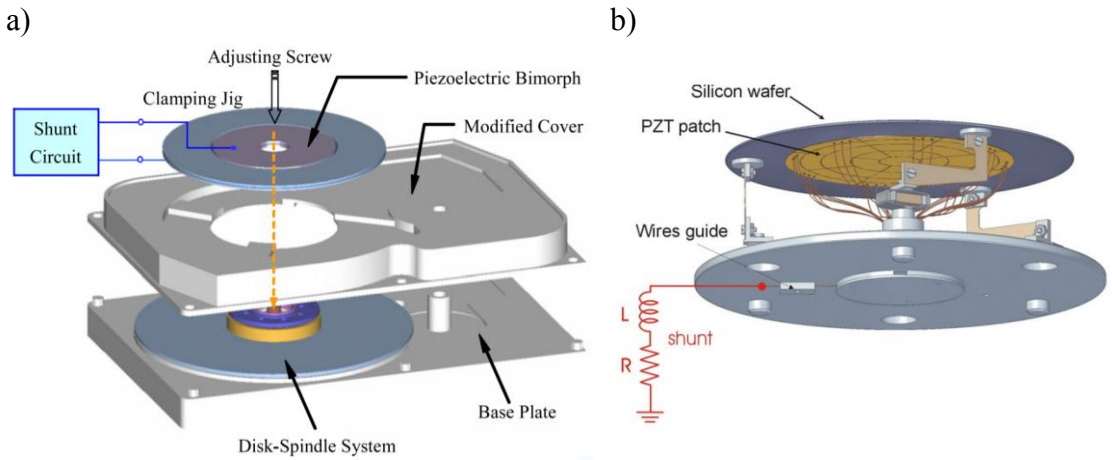

Figure 3.3: Applications of Piezoelectric damping. a) Vibration control using piezoelectric bimorph in HDD [10] b) Damping of vibrations in deformable mirror of space telescope during launching [63].

3.2 Magnetostrictive Damping

Magnetostrictive (MS) materials exhibits shape change upon application of magnetic field. This phenomenon is called magnetostriction also known as Joule mangnetostriction. The alignment of magnetic domains are responsible for the shape change resulting in an actuation as illustrated in Fig. 3.4. The high speed domain alignment enables the actuation above 20 kHz. A similar behavior is also observed in dielectric materials under external electric field. This property is called electrostriction. The strain behavior in electrostrictive materials is proportional to square of applied electric field. Therefore, the reversal of elongation direction is not followed by reversing the applied field. Electrostrictive materials do not show inverse behavior of generation of electric field by mechanical deformation. Owing to these properties, electrostrictive materials are not much deployed in practical applications.

Magnetostrictive effect is present in most of the ferromagnetic materials. The humming sound from the core of electric transformer is an effect of this behavior [64]. The popular MS materials are Terfenol-D (alloy of terbium, iron and dysprosium), and Galfenol (alloy of iron and gallium). The high operating temperature of these materials enables reliable performance even under harsh environmental conditions without undergoing permanent depolarization. The frequency of operation is constrained by the eddy current, electrical inductance and mechanical resonance [65]. Terfenol-D generates of recoverable strain of about 0.15% at a high magnetic field of 160 kA/s. It is brittle and withstands only compressive loads. On the other hand, Galfenol has a tensile strength of about 500 MPa, allowing tensile loading conditions. The recoverable strain of Galfenol is about 0.04% [66]. Besides Joule magnetostriction, MS materials demonstrates Villari effects, hysteresis and Delta-E effects favoring active, semi-active and passive vibration control. MS materials under mechanical loading aligns magnetic dipoles to the plane perpendicular to loading direction. This phenomenon is called inverse MS effect or 'Villari effect'. The change in magnetization could induce electrical energy on pick-up coil wound around the MS material. By dissipating the electrical energy via a shunt circuit, the mechanical energy is dissipated. Eddy current losses also dissipates significant amount of mechanical energy in magnetostrictive materials with high electrical conductivity [67]. Additional dissipation in MS materials is contributed by hysteresis

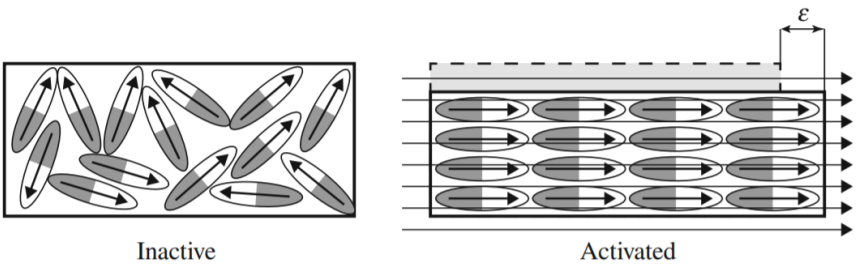

Figure 3.4: Behaviour of magnetostrictive materials. Magnetic domain alignment under external magnetic field results in elongation of the material [64].

owing to crystal defects and imperfections. The Young's modulus change of Terfenol-D and Galfenol with respect to external excitation called the delta-E effect is exploited for active and semi-active vibration control [20-21].

Magnetostrictive effect is studied for many noise control applications. The structure-borne vibrations arising from rotor and gear mechanism in helicopter introduces cabin noise with frequency components up to 6 kHz. The propagation of noise to the fuselage is reduced by active vibration control of the connecting struts using magnetostrictive actuators [70]. Passive damping of magnetostrictive materials is based on energy dissipation through eddy currents and magnetic hysteresis [71]. Passive damping making use of Villari effect by introducing shunt circuits have demonstrated high loss factors. MS materials have high stiffness are exhibits high loss factor compared to other damping materials are shown in Fig. 3.5. Semi active magnetostrictive control exploits stiffness modulation by an energy source. Smart mounts for the gear box of helicopter is an application of semi-active vibration control [65].

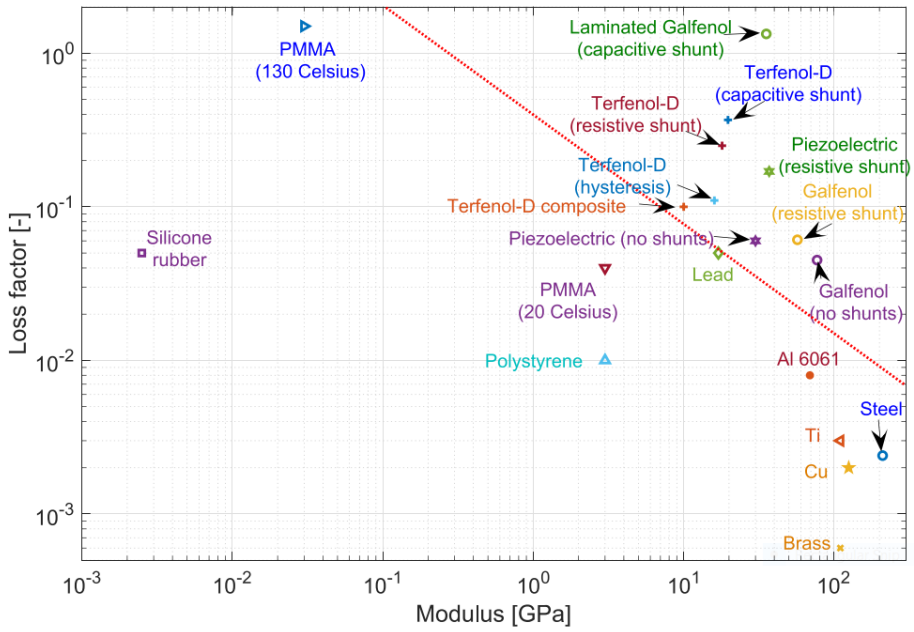

Figure 3.5: Loss factor of magnetostrictive materials and configurations [65].

3.3 Electro- and Magneto-Rheological Fluidic Damping

Rheology deals with the flow of matter in liquid, solid-like or solid form that flows undergoes plastic deformation under the application of external excitation. The rheological properties like yield stress, shear stress, dynamic modulus and compliance of

such material changes with the external excitation [72]. In electrorheological (ER) and magnetorheological (MR) fluids, rheological properties of the fluids alter under the influence of external electric and magnetic fields respectively. Bingham plastic model is commonly used to describe the fluid behavior. The modes of operation of ER/MR fluids are shear, flow and squeeze mode as indicated in Fig. 3.6. Both ER/MR fluids offers semi-active vibration control with quick response time of the order of milliseconds.

Electrorheological fluid suspension contains polarizable or semiconductive particles of 0.1 - 50 μm suspended in an insulating carrier fluid with polar materials called additives to improve the ER effect and to prevent agglomeration [24,25]. Depending upon the type of polarization ER fluids are classified as dielectric electrorheological (DER) and giant electrorheological (GER) fluids [74]. The operation mechanism of DER fluids is explained by heuristic theory. According to heuristic theory, the solid particles are polarized under electric field resulting in an induced dipole-dipole interaction between the particles. This results in agglomeration and column-like formation of particles along the field direction. The GER effect is first observed in nanoparticles of barium titanate oxylate coated with thin layer of urea dispersed in silicone oil. The yield strength in GER fluids is one to two orders of magnitude higher than in DER fluids [74]. The attractive forces contributing to high yield strength is considered to be arising from the dipole-dipole interaction of the polar molecules (urea in previous example) and dipole- charge interaction between polar molecule and nanoparticles (urea and barium titanate oxylate in previous example) [26, 27]. ER fluids are studied in chatter vibration control for machining, clutches and brakes. ER fluids require high electric field typically between 0.5 – 3 kV/mm [73].

Magnetorheological fluids consist of magnetic particles, carrier fluid and additives. Spherical carbonyl iron particles of a few μm are commonly used as magnetic particles. Low viscous hydraulic or silicone oil is used as carrier fluid that will not chemically react with the magnetic particles. Additives prevent sedimentation of magnetic particles and reduce interparticle friction [24, 25]. By the application of magnetic field, MR fluids

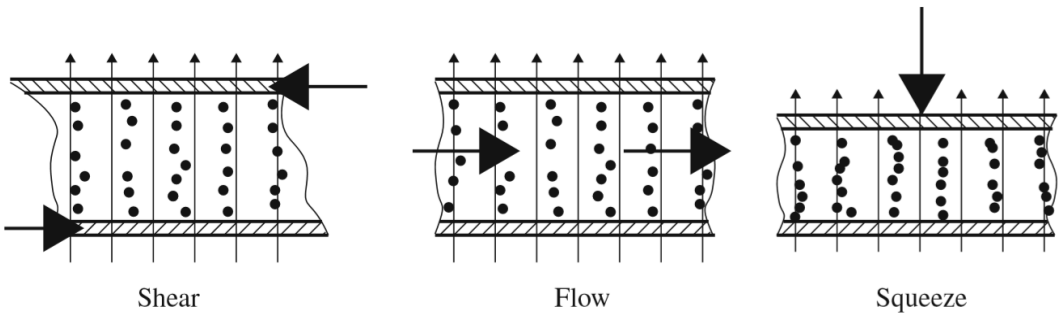

Figure 3.6: Operating modes of ER/MR fluids. The thick arrow indicates the movement direction and the thin arrow represents the field direction [64].

demonstrates a semi-solid like behavior exhibiting high yield strength. Depending on the direction of external force on MR fluid operates in three modes: flow, shear and squeeze modes. Linear and rotary damping applications make use of flow and shear mode of operations respectively [78]. Squeeze mode allows large compressive stress and effective in stabilizing vibrating platforms [64]. MR dampers have shown to be effective in a wide spectrum of applications like vehicle suspension, brakes, engine suspension, seismic protection for buildings and suspension bridges [27, 28].

3.4 Electro Active Polymer Damping

Electro Active Polymers (EAP) undergo mechanical deformation under the application of electric field. Though the operation of EAPs is similar to piezoelectric ceramics, EAPs could exhibit large strains of above 300% [81]. Depending upon the principle of operation, EAPs are classified as electronic (or dry) and ionic EAPs.

Electronic EAPs includes ferroelectric polymers, electrostrictive graft elastomers, liquid crystal elastomers and dielectric electroactive polymers (DEAPs), also referred to as dielectric elastomers (DEs)m[33, 34]. Ferroelectric polymers possess permanent electric dipole which could be reversed by an external electric field resulting in large strain. Poly (vinylidene fluoride–trifluoroethylene) (P(VDF–TrFE)) is a commonly used ferroelectric polymer. By the application of electric field P(VDF–TrFE) contracts along the field direction and expands along the direction perpendicular to field. A strain of about 7% is obtained for a stress of 45 MPa [83]. Energy dissipation is associated with the change in direction of polarization. The use of ferroelectric polymers is limited by high electric fields and fatigue life of electrodes.

Electrostrictive graft elastomer consists of a flexible polymer backbone and crystallizable side chains called grafts attached to the polymer backbone. The grafts crystallize to form cross-linked elastomer network and electro-responsive polar crystal domains. The rotation of polar domains to align with the external electric field introduces deformation in the material. The removal of electric field leads to randomization of polar domains resulting in shape recovery. Electrostrictive graft polymer could withstand a high stress of about 550 MPa with a reversible strain of 4% [84].

Liquid crystal elastomers are composite materials that have elastic properties of a polymer and alignment properties of liquid crystals. The liquid crystal side chains are bonded to cross-linked polymer backbone. The application of temperature or electrical excitation results in change of crystal orientation introducing stresses and strains on the polymer backbone. Strain of 4% is observed in electric field activated materials and a high strain of 45% is obtained in thermally activated materials [83].

Dielectric elastomer (DE) actuators consists of an incompressible and deformable dielectric material between two parallel plates of a capacitor. By the application of electric field, electrostatic forces between the capacitor plates brings the plates closer, squeezing the dielectric material. The dielectric material expands in the lateral direction. A high electric field of about 100 V/µm is required for the operation of DE actuator [85]. The shape flexibility and low weight properties of DE actuators are exploited in loudspeakers instead of moving-coil electromagnet loudspeakers. DE actuators are investigated as adaptive acoustic absorbers to reduce cabin noise in aircraft and automobiles [86]. DE actuators shows effectiveness as vibration isolators and dampers for frequencies up to a few hundreds of Hz [82].

Ionic EAP includes polymer gels, Ionic Polymer Metal Composite (IPMC), conducting polymer and carbon nanotube actuator. Polymer gels consists of polymer gel material like polyacrylic gel between a pair of electrodes. Under the application of external current, the region near to anode becomes acidic and that of cathode turns basic. The migration of ions between cathode and anode region results in large reversible deformation. Due to the requirement of large current requirement and low actuation force, polymeric gels are predominantly used in bending application [64].

Ionic Polymer Metal Composite (IPMC) consists of ion exchange polymer sandwiched between two electrodes. Typical ion exchange polymer material is Nafion. The application of electric field introduces an ion concentration gradient and attracts water towards an electrode resulting in actuation. The operation voltage is in the range of 1-10 V. Large displacements are possible only at low frequencies below 0.1 Hz [87]. Damping applications with IPMC are proposed in spacesuits to prevent muscle atrophies of astronauts [88]. Active vibration damping using IPMC is demonstrated by stabilizing a flexible beam with IPMC patches triggered 180° out of phase to the excitation of the beam [89].

Conducting polymer undergoes change in oxidation state under external electrical excitation, forcing ions into or out of the polymer chains, resulting in actuation. Conductive polymers have high tensile strength of (>100 MPa) and strain between 2 to 20%. However, the low electromechanical coupling (<1%) leads to low operating efficiencies [64]. Conductive polymers are not much explored for vibration damping applications.

Carbon nanotubes (CNTs) are of high research interest due to its unusual electrical and mechanical properties. CNTs have an exceptional high tensile strength of more than 1 GPa with a recoverable strain of about 0.1 to 1% [85]. The difficulties in mass production restricts the commercial application of CNT based EAP.

3.5 Shape Memory Alloy (SMA) Damping

Shape memory alloys undergo phase transformation between austenite and martensite phases under the effect of stress or temperature. Stress induced phase transformation is called the pseudoelastic effect and temperature induced phase transformation called one-way shape memory effects. The phase transformation results in large energy dissipation. Pseudoelastic effect is utilized for passive damping applications, whereas one-way shape memory effect enables active damping applications.

3.5.1 Pseudoelastic SMA Damping

The pseudoelastic SMAs have high specific stiffness and high damping capacity at loading strain below 10%. The energy dissipation and loss factor through the martensite phase transformation depends upon the loading amplitude, pre-strain, operating frequency and ambient temperature. In an extensive research, Piedboeuf et al. observed energy dissipation and loss factor variations with the operating frequency in a pseudoelastic NiTi wire of 100 μm. The existence of an optimal operating frequency is identified at 0.01 Hz for the NiTi wire under test, where the heat generated during loading is effectively dissipated with no net increase in the temperature of the NiTi wire. The optimal frequency depends on dimensions and shape of the material, which determines the time constant for heat dissipation. Maximum energy dissipation requires the operating frequency to be in-line with the heat transfer time. A further increase in operating frequency results in a net increase in temperature of the test specimen (called the self-heating phenomenon) resulting in a reduction of energy dissipation and loss factor. When the self-heating dominates, the temperature during unloading is higher than the loading condition [90]. Wolons et al observed a stabilizing trend in energy dissipation at frequencies close to 10 Hz [17].

The energy dissipation depends strongly on the loading amplitude. A linear increasing behaviour is observed for the energy dissipation with increase of loading amplitudes [17]. Wolons et.al observed a sharp reduction in energy dissipation with the increase in frequency. The energy dissipated by hysteresis drops by about 50% when the operating frequency is changed from 0.2 to 6 Hz. A comparative study with elastomer indicates over 20 times higher energy dissipation per unit volume for pseudoelastic SMA over elastomer [17].

The ambient temperature affects the critical stress for transformation in both loading and unloading directions. The critical stress in loading and unloading directions increases linearly with temperature introducing a shift in hysteresis area [17]. However, there are contradicting reports on the influence of ambient temperature on the energy dissipation. Dolce et al. reported that the energy dissipation is independent of the ambient temperature observing a stable energy dissipation on a NiTi wire of 1 mm from temperatures of -10

to 40 °C [91]. Wolons et al. observed a temperature dependence on energy dissipation on a NiTi wire of 0.5 mm diameter when the temperature is varied between 20 and 75 °C. A slight increasing trend in the energy dissipation is observed at temperatures between 20 and 35 °C. Energy dissipation decreases in the temperature range of 35 to 75 °C. The authors suggest the existence of ideal operating condition for a pseudoelastic SMA depending on the microstructural nature of the material under testing [17].

The energy based design approach introduced by Housner in 1956 is commonly used in structural vibration control. The optimal vibration control approach is to minimize the transfer of energy to the structure and dissipate the majority of the transferred energy through hysteretic damping of the material thereby reducing the damage energy to the structure [92]. In the last decade of twentieth century, pseudoelastic SMAs are investigated as seismic isolators. Graessar et al. proposed the usage of SMA damper as seismic isolator for buildings as a replacement for the rubber bearings, which requires high strains for hysteretic behaviour [93]. Wilde et al. investigated vibration isolation system for elevated highway bridges using SMA bars and elastomer bearings demonstrating a reduction of structure damage energy by 14% over lead rubber bearings. Owing to high stiffness of SMA based damper, the input energy on the structure arising from the base excitation is higher than the damping from lead rubber bearings. The high material dissipation of SMA based damper effectively dissipates most of the input energy substantially decreasing the structure damage energy [94].

The pseudoelastic SMA for seismic isolation by incorporating self-centering and high dissipation is extensively investigated within the framework of MANSIDE (Memory Alloys for New Seismic Isolation and Energy Dissipation Devices) project (1995-1999). Two antagonistically moving SMA wire loops are used to achieve high energy dissipation by optimally pre-straining each SMA wire loop half-way to the full phase transformation.

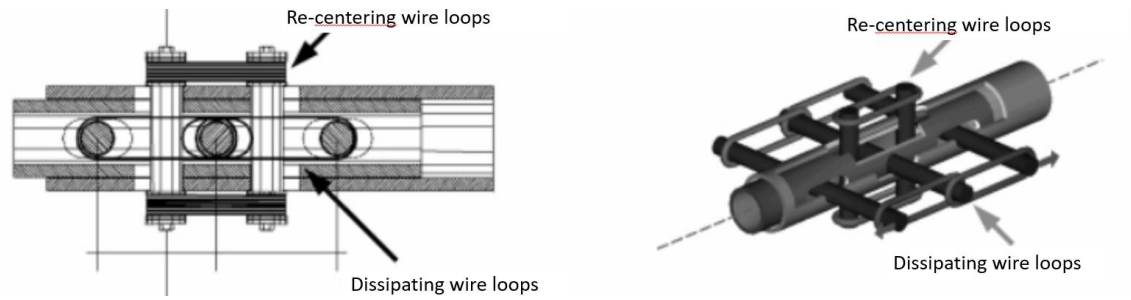

Figure 3.7: High energy dissipating SMA isolator device with re-centering property [95].

The self-centering behaviour is attained by another transversely connected pre-strained SMA wire loop, which undergoes elongation irrespective of loading direction as shown in Fig. 3.7 [95].

The investigation of pseudoelastic SMA devices as retrofit for the rehabilitation of cultural and heritage structures was extensively performed under ISTECH project (1996-1999). The SMA device along with steel tendons dissipates about 30% of the seismic input energy along in-plane direction. The out-of-plane vibration resistance is increased by more than 50% by connecting the walls to the floor level using SMA device ties than popularly used steel ties. On the basis of these findings, the rehabilitation of Bell tower of S. Giorgio in Rio (Italy) and transept tympanum of the Basilica of St. Francis of Assisi, which was severely damaged under earthquakes of 1996 and 1997 respectively, were carried out using SMA devices [97].

Besides the aforementioned damping applications for bridges and buildings, Pseudoelastic SMA could be used in military applications as bullet-proof material to enhance impact resistance ballistic velocities (> 244 m/s). The combination of SMA fibre layer with extended chain polyethylene (ECPE) have demonstrated high energy dissipation. A single layer SMA fibre with three layer ECPE have shown 23% absorption of impact energy. [50, 51].

The fabrication compatibility of SMA with MEMS process flow allows vibration damping application at a wafer level. Heterostructures involving SMA and piezoelectric materials have shown increased dissipation due to hysteretic dissipation from SMA layer and energy dissipation from piezoelectric layer through an external impedance. The heterostructures are DC magnetron sputter deposited on a silicon wafer. The damping performance of NiTiCu/ AlN heterostructure have shown an enhancement in energy

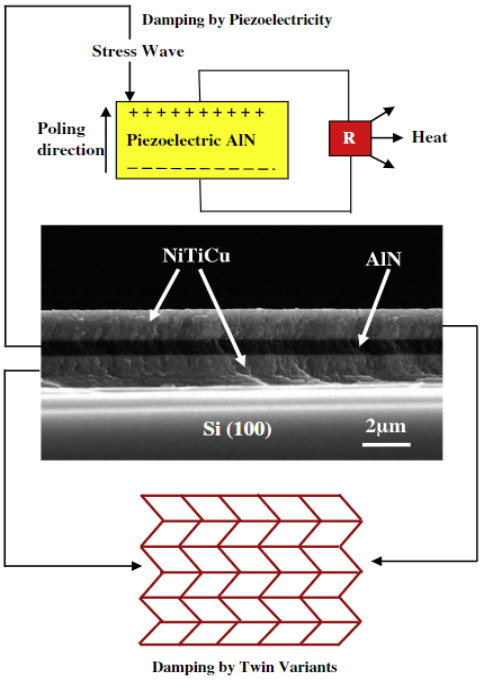

Figure 3.8: SMA - Piezoelectric heterostructure shows enhanced damping behaviour due to pseudoelastic behaviour of SMA and shunt damping of piezoelectric material [96].

dissipation than NiTiCu layer alone during nanoindentation. Sandwiching piezoelectric material between SMA layers like NiTiCu/ AlN / NiTiCu, as indicated in Fig. 3.8, enhances the energy dissipation by about three times than with NiTiCu layer alone [96]. The high energy dissipation is due to the combined energy dissipation from both SMA and piezoelectric material.

3.5.2 One-way SMA Vibration Control

The temperature-induced phase transformation and stress-induced re-orientation are responsible for high damping behavior of one-way SMA. The temperature induced phase transformation is between martensite and austenite whereas stress-induced re-orientation is between martensite variants. The actuation and stiffness change of the material arising from temperature induced phase transformation is exploited for active and semi-active vibration control applications.

One of the earliest demonstration of active vibration control was performed by Baz et al. to mitigate flexural vibration of a beam using SMA wire actuators of 400 µm diameter [100]. An on/off control approach is used to Joule heat the SMA actuator in order to counter act the flexural vibration. A zone of no heating pulse is defined close to the equilibrium position to avoid enhanced flexural vibration when the beam is settling down to the equilibrium position. Additionally, the heating power of actuators also has to be adjusted with respect to the heating and cooling time constants of the actuator [100].

In aerospace industry SMA is investigated for noise control applications. Design of Variable Geometry Chevron (VGC) using SMA facilitates the cabin noise reduction during take-off. The SMA actuators placed over the chevron of jet engine as shown in Fig. 3.9. During take-off, the SMA actuators immerse the chevrons towards the engine leading to a reduction in low frequency noise level. The morphology change introduced by SMA actuators reduced the sound level by 2-5 dB [101].

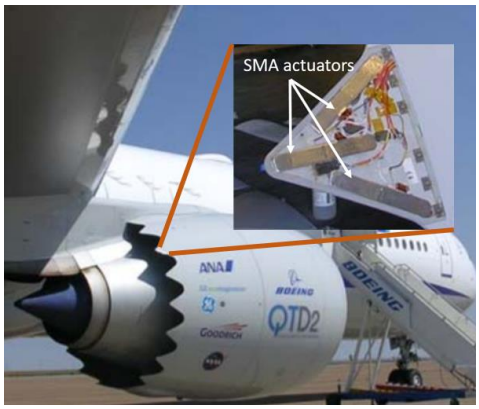

Figure 3.9: Chevron with SMA actuators for noise reduction during flight take-off [101].

SMA hybrids consisting of NiTi fibers allows stiffness modulation by the application of heat. Rogers et al. studied the stiffness modulation of NiTi-reinforced graphite-epoxy beam by exciting the beam with a shock loading at different temperatures. The behavior of graphite-epoxy beam shows a decreasing trend in the first mode frequency with temperature, whereas, NiTi-reinforced graphite-epoxy shows an increasing trend due to high stiffness of Austenite phase. It was proposed to obtain temperature independent dynamic behavior of hybrid beams making use of stiffness modulation of SMA, thereby limiting the structural acoustic radiation [102].

The SMA composite structures demonstrates a shift in the natural frequency of oscillation depending on the volume fraction of the SMA in the composite and the stress on the material. In a Kevlar-epoxy-SMA composite a frequency shift of about 75 Hz is observed by the adjustment of stiffness of SMA by heating. The frequency shift shows a linear trend with respect to the stress in the material, irrespective of how the strain is introduced in the composite [103].

The vibration control using SMA could be extended for miniature scale applications. Kazi et al. developed optical image stabilizing platform against hand movements for miniature cameras in handheld devices using SMA actuators. SMA wires of 20 µm diameter are used as actuators utilizing one-way shape memory effect. The wires are selectively activated by current pulses to stabilize the lens holder after detecting an external vibration. The lens holder consists of flexural hinges allowing counteracting movement against hand movements allowing 2-DoF stabilization as shown in Fig. 3.10. A tilt angle of about 10 mrad is achieved by this design. The operating frequency range above 6 Hz is obtained using PI feedback loop and a feedforward control [104].

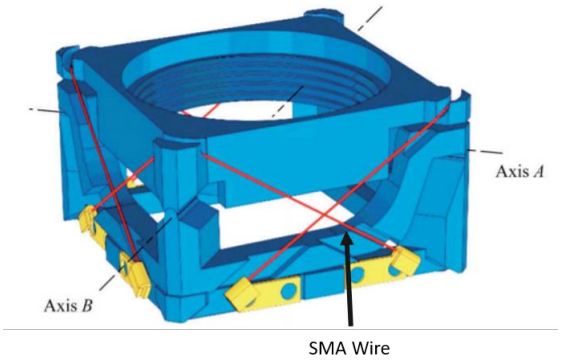

Figure 3.10: 2-DoF optical image stabilization platform for microcamera in handheld applications [104].

3.5.3 Conclusion

Among the smart materials used for vibration damping and control applications, shape memory materials offer biocompatible and noise-free operation allowing high stroke

operation. The material level investigations of SMA revealed high dissipation under passive damping operation and demonstrated mitigation of vibration for buildings under shock loading condition. Besides, the one-way material allows active damping by the application of current pulse. However, the usage of SMA devices for miniature damping/ control applications is not much investigated. Most of the existing SMA damper devices are based on SMA wires which are not suitable to incorporate in MEMS devices. Therefore, in this work, the focus is to develop miniature SMA damping devices out of cold-rolled foils using lithography or precision laser cutting.

4 Material Characterization and Device Fabrication

The material characterization of NiTi based SMA involves the thermomechanical characterization using tensile testing and differential scanning calorimetry (DSC). A temperature chamber is installed around the tensile test equipment in order to investigate the temperature dependent mechanical properties. Cold-rolled SMA foils are used for the material characterization and fabrication of devices. The thermomechanical behavior of NiTi based SMAs, device fabrication technique and the test setups used for the investigation are explained in this chapter.

4.1 Pseudoelastic SMA Foil Characterization

The phase transformation properties of $Ti_{49.1}Ni_{50.5}Fe_{0.4}$ (at. %) pseudoelastic SMA foil of 30µm thickness is adjusted by heat treatment at 450°C for 30 minutes under high vacuum condition. The phase transformation behavior is observed using DSC measurement as shown in Fig. 4.1(a). The sample consists of small SMA-foil pieces weighing about 7-10 mg and the measurement is performed using Netzsch DSC 204 Phoenix. The temperature is swept from -100 to 150 °C at a rate of 10 °C/min. The phase transformation from martensite to austenite is an endothermic process resulting in transformation peak at a temperature of 25.5 °C. While cooling down, the material has a single-step transformation from austenite to martensite at a temperature of about 22.5 °C. The

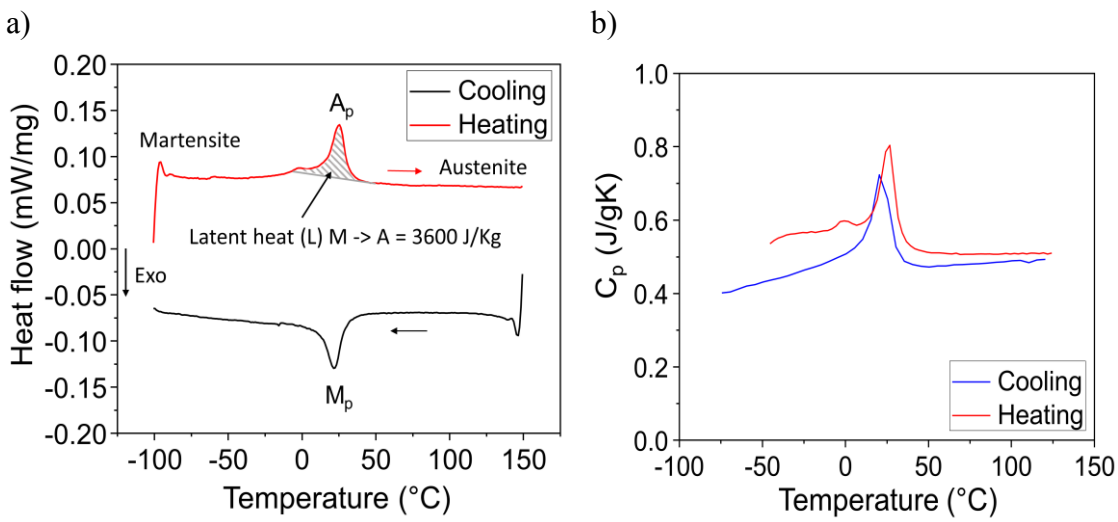

Figure 4.1: Material characterization of pseudoelastic NiTiFe foil. (a) DSC measurement indicates a single-step transformation with A_p = 25.5 °C, M_p = 22.5 °C. (b) The variation of specific heat at constant pressure (C_p) shows a constant behaviour in austenitic phase.

material exhibits a pseudoelastic behavior close to room temperature (25 °C). The latent heat associated with austenitic and martensitic transformations are 3.59 and 3.83 J/g respectively. The specific heat at constant pressure (C_p) for different temperature conditions are shown in Fig. 4.1(b). In the martensitic state, C_p slowly decreases with decrease in temperature. In austenitic phase, C_p is close to 0.5 J/gK and remains independent of temperature.

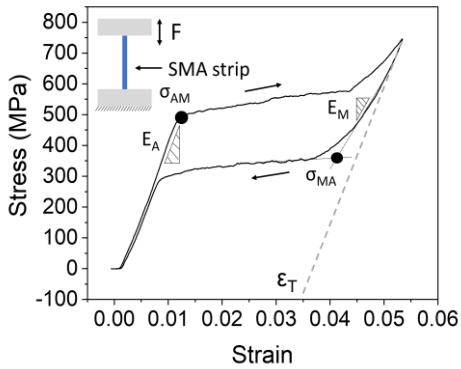

Figure 4.2: Mechanical behaviour of NiTiFe strip at room temperature under isothermal loading condition with a strain rate of $10^{-3}s^{-1}$.

A strip of NiTiFe is mechanically characterized under tensile loading condition at a strain rate of 10^{-3} s^{-1}. Under this strain rate the strip is loaded isothermally. The stress-strain behavior is indicated in Fig. 4.2. Below the critical stress of 500 MPa, the material behaves like an elastic material. The phase transformation is initiated above the critical stress. At this stress condition, the phase transformation to martensite allows large strain.

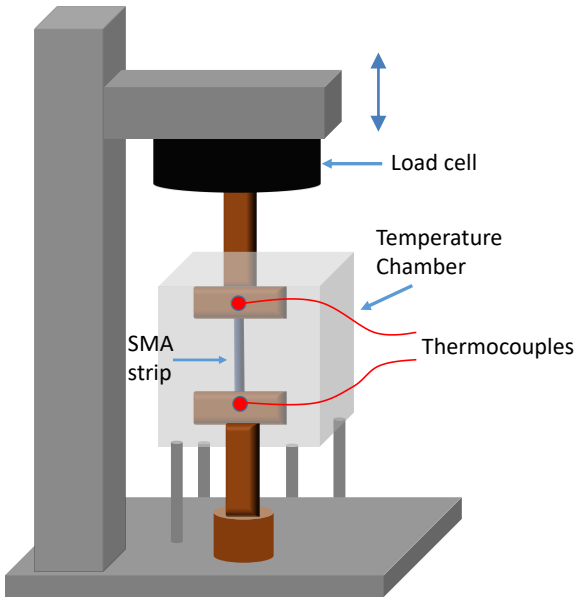

Figure 4.3: Schematic of test-setup for the temperature dependent mechanical characterization.

The complete transformation is identified by a sudden rise in the stress level for any further deformation. Upon unloading, the material recovers its original dimension with a hysteresis. The recoverable strain of NiTiFe is about 5%. The maximum pseudoelastic strain associated with stress induced martensitic transformation called the transformation strain (ε_T) is estimated by interpolating the elastic component during the reverse transformation from martensite to austenite.

The temperature based mechanical characterization is performed using the test-setup shown in Fig. 4.3. A test strip of dimension $17.6\ (l) \times 2\ (w) \times 0.03(t)\ mm^3$ is used for this measurement. A temperature chamber is installed around the SMA sample holder of the tensile testing device. The sample holders are made of polyether ether ketone (PEEK). The temperature inside the thermal chamber is restricted below 40 °C to avoid significant contribution of the holder during mechanical loading of the sample. Two thermocouples are connected to the top and bottom holders near to the SMA strips. The temperature chamber is Joule heated to the desired SMA sample temperature. The SMA sample temperature is assumed to be the average temperature of two thermocouples. The mechanical loading of the SMA strips for a strain rate of 10^{-3} s^{-1} at different ambient temperatures are shown in Fig. 4.4(a). The critical stress of SMA varies linearly with temperature [91]. The Clausius-Clapeyron coefficient for the SMA material is estimated from the stress variation with respect to temperature.

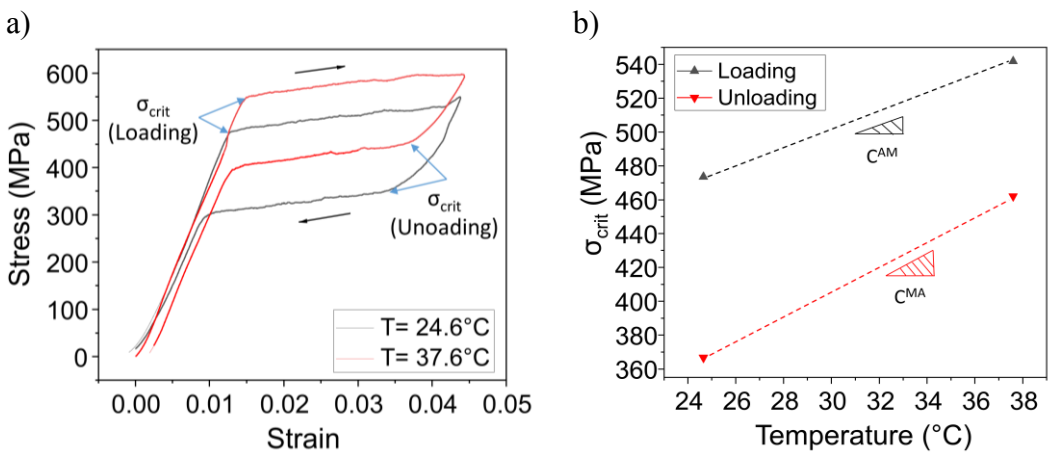

Figure 4.4: Temperature-dependent pseudoelastic SMA behaviour under mechanical loading condition shows a shift in stress plateau with temperature (a) and critical stress during loading and unloading condition at room temperature and 37.6 °C.

The thermal relaxation of the material is investigated by loading the material under adiabatic condition. The material is loaded to a strain of 5% at a strain rate of $3x10^{-2}$ s^{-1} and retained under this loaded condition for 10s. The temperature variation in the sample is observed using an infrared thermography. Fig. 4.5 indicates the time resolved temperature evolution at the center of the sample on a measurement area of 50x50 μm^2. A peak temperature of 36.5 °C is reached at maximum loading of the sample. During the

holding time, the heat is dissipated through convection with the surrounding environment and conduction to the clamps of the sample. The thermal relaxation time constant is estimated to be 1.8s. Upon unloading, a cooling behavior is observed with temperature reaching about 14 °C.

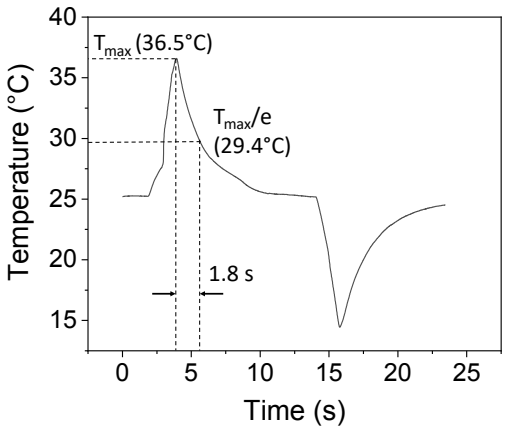

Figure 4.5: Thermal relaxation of NiTiFe, elongated at a strain rate of $3 \times 10^{-2}\ s^{-1}$ *indicates a relaxation time constant of 1.8s.*

Table 4.1 summarizes the material parameters for pseudoelastic NiTiFe. These parameters are used to develop a simulation model to understand the macro and mesoscopic behavior of the material and to validate the behavior under quasi-stationary loading condition. The model is further extended to predict the dynamic behavior of pseudoelastic devices.

Table 4.1: The summary of material parameters of NiTiFe.

Parameter	**Symbol**	**Value**
Critical stress for A – M transformation (at RT)	σ_{AM}	497 MPa
Critical stress for M – A reverse transformation (at RT)	σ_{MA}	359 MPa
Clausius–Clapeyron coefficient (A → M)	C^{AM}	12.59-13.92 MPa/K
Clausius–Clapeyron coefficient (M → A)	C^{MA}	12.45-13.76 MPa/K
Transformation strain	ε_T	0.035
Elastic modulus of austenite	E_A	51 GPa
Elastic modulus of martensite	E_M	35 GPa
Latent heat (M → A)	L	3600 J/kg
Ambient temperature	$T_{ambient}$	298 K
Heat transfer coefficient *	h	30 W/m^2/K
Thermal Relaxation time		1.8s

** The parameter is estimated according to the supplementary data provided in [105]*

4.2 One-way SMA Characterization

The cold-rolled $Ti_{50.18}Ni_{49.82}$ (at. %) foil is heat treated to tailor the phase transformation behavior under high vacuum condition for 30 minutes. The materials are heat treated at temperatures of 450 and 500 °C. The behavior of SMA under thermomechanical loading conditions are discussed in this section.

The phase transformation behavior of the SMA foil annealed at 500 °C is indicated in Fig. 4.6(a). Starting from -100 °C, the material transforms from martensite to austenite between 40 and 60 °C. While cooling down, the material transforms to martensite via an intermediate R-phase. The latent heat associated with austenite, martensite and R-phase transformations is 20.6, 6.1 and 11.9 J/g respectively. The material is in R-phase at room temperature (RT) under stress free condition. The normal operating condition of SMA is indicated in Fig. 4.6(b). During the temperature sweep from 20 to 150 °C, the material is

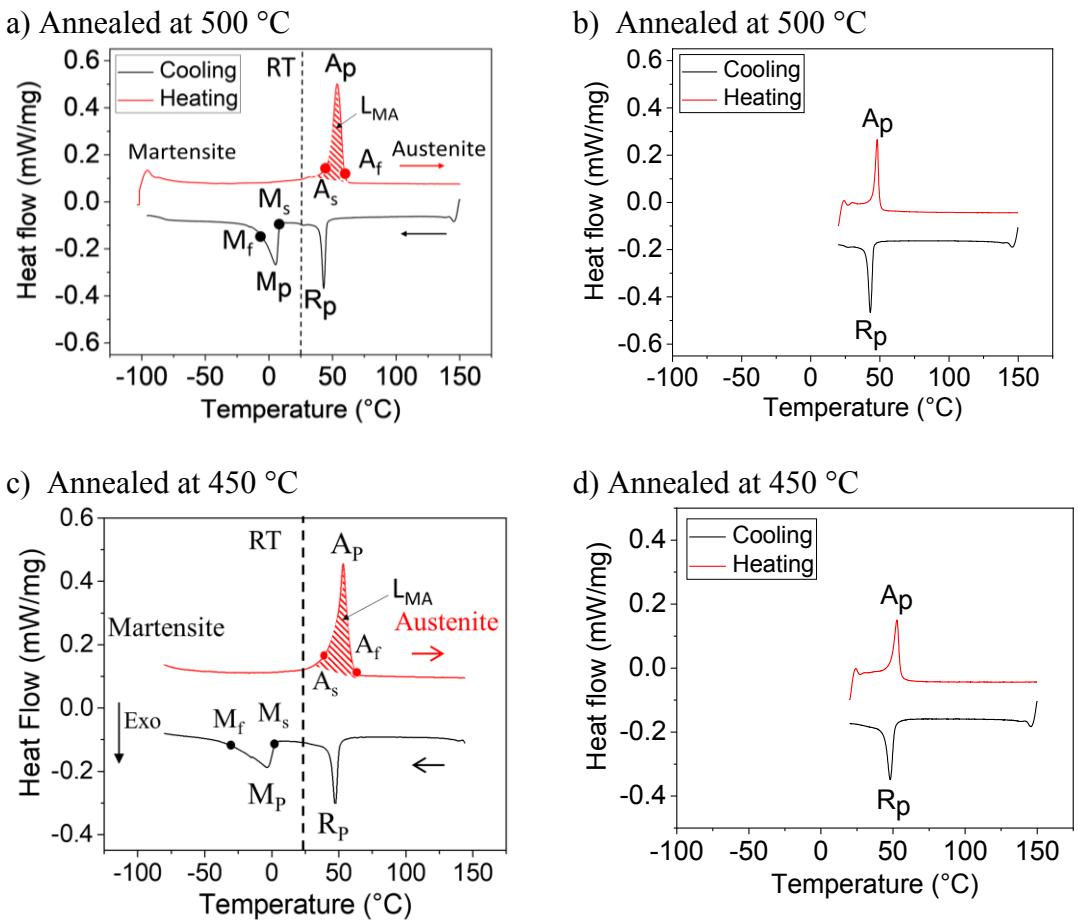

Figure 4.6: Phase transformation of NiTi foil annealed at 500 and 450 °C. (a) The temperature sweep from -100 to 150 °C shows A_s = 47.6, A_p = 53.3, A_f = 59.1, R_p = 42.8, M_s = 8.3 °C, M_p = 5.09 °C, M_f = -6.6 °C. (b) Temperature sweep from 20 to 150 °C shows a narrow austenite phase transformation region (A_p = 48.2, R_p = 42.8 °C). (c) At annealing condition of 450 °C, shallow peaks are associated with phase transformations (A_s = 47.2, A_p = 54.2, A_f = 59.1, R_p = 47.9, M_s = 2, M_p = -5.09 °C, M_f = −28.5 °C). (d) For temperature sweep from 20°C, the transformation peaks are at A_p = 47.9, R_p = 47.5 °C.

in R-phase at 20 °C and transforms to austenite between 44 and 50 °C. The latent heat involved in the austenite and R phase transformation are 6.1 and 6.2 J/g respectively.

The SMA foil annealed at 450 °C have more shallow peaks associated with the phase transformation. The austenite transformation occurs in the temperature range of 35 to 60 °C for a temperature sweep between -100 and 150 °C as indicated in Fig. 4.6(c). The martensite transformation occurs over a broad temperature range from 2 to -30 °C. Therefore, a low transformation rate is observed under 450 °C annealing condition. This behavior indicates a variation in the crystallography of SMA with the annealing condition. The latent heat associated with austenite, martensite and R-phase transformations are 18.2, 6.2 and 7.9 J/g respectively. The temperature sweep from 20 °C also shows a shallow transformation peak with associated latent heats of 5.6 (R→A) and 5.5 J/g (A→R) as indicated in Fig. 4.6(d).

The mechanical characterization of NiTi strips are performed under different temperature condition using a temperature chamber as shown in Fig. 4.7(a). The test setup is similar to Fig. 4.3, but with additional cooling fan and metal holders for the NiTi sample. The metal holder is used to minimize the effect of holder on material deformation behavior at high chamber temperatures. The usage of metal holders allows for the quick heat transfer from the temperature chamber. In the test condition, it is required to maintain the temperature of the load cell below 40 °C with a maximum temperature fluctuation below 1 °C. Maintaining chamber temperature above the phase transformation temperature of the material heats up the load cell above 40 °C. The problem is resolved by adding a cooling fan in the test setup which maintains the temperature at load cell below 40 °C even when the chamber temperature is about 90 °C.

The mechanical behavior of NiTi specimen at an annealing temperature of 500 °C is shown in Fig 4.7(b). With the increase in chamber temperature, the stress plateau shifts to higher stress levels. The strain recovery is observed for temperatures above austenitic phase transformation. However, a residual plasticity is observed under this annealing condition for chamber temperatures above Austenite finish temperature. The critical stress variation with temperature under loading condition is 5.92 MPa/K.

At 450 °C annealing condition, a complete strain recovery is observed above phase transformation temperature as indicated in Fig. 4.7(c). A sharp transformation behavior is observed under mechanical loading by flat stress plateau at chamber temperatures of 69.5 and 76.5 °C. The Clausius-Clapeyron coefficient for loading condition is 5.76 MPa/K. At temperatures above A_f the Clausius-Clapeyron coefficient for Martensite to Austenite transformation is between 9.88-10.92 MPa/K considering a measurement error of 5%.

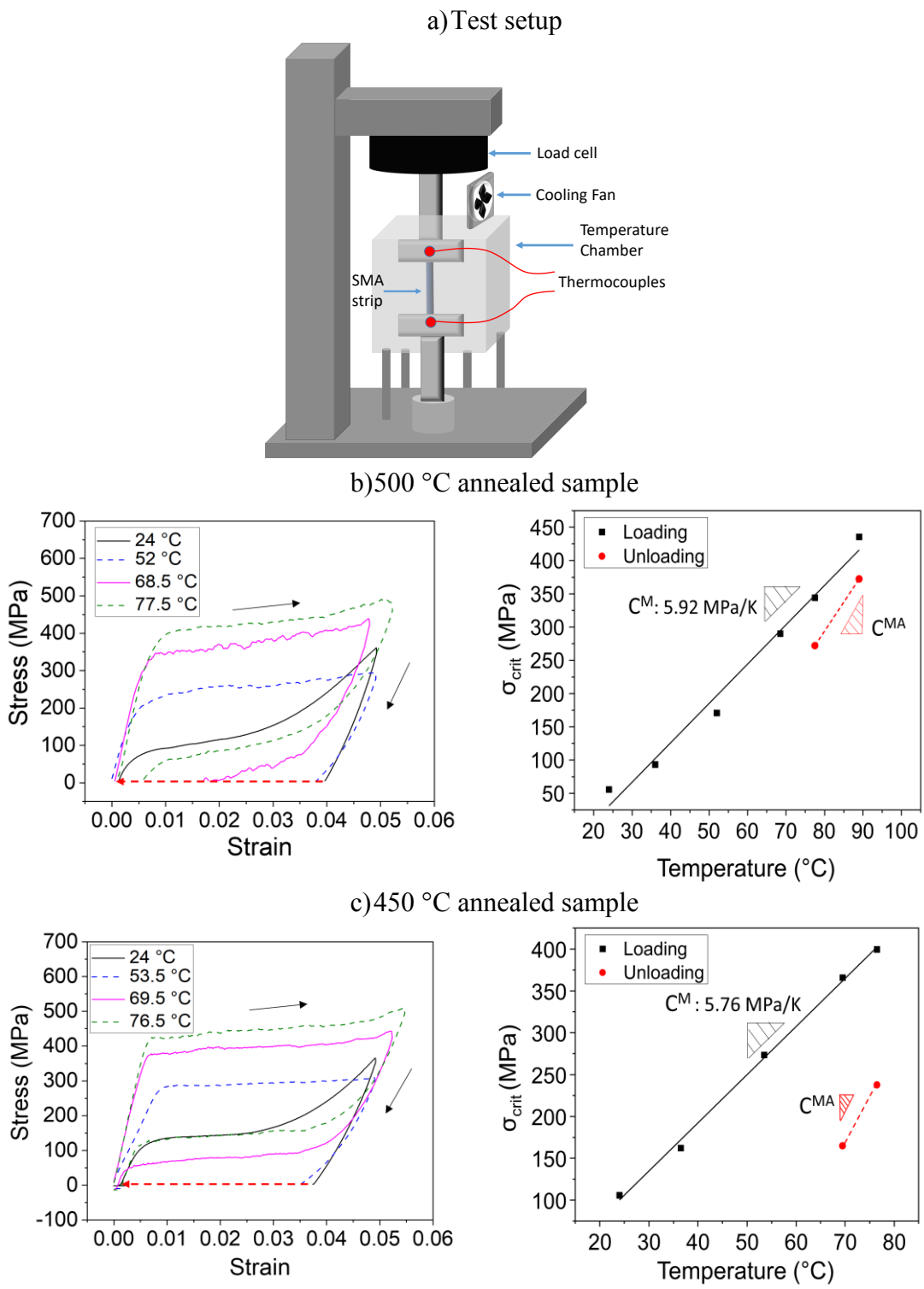

Figure 4.7: The test setup to investigate mechanical behaviour of NiTi at different temperatures is shown in (a). Thermo-mechanical behaviour of NiTi material and Clausius-Clapeyron coefficient under annealing temperatures of 500 and 450 °C at a strain rate of $10^{-3}s^{-1}$are indicated in (b) and (c).

The material annealed at 450 °C is characterized under tensile loading at different strain rates at room temperature. In Fig. 4.8(a), the NiTi test strip is cut out along the rolling direction of the foil. As the loading rate increases, the critical stress for martensitic re-orientation also increases. This behavior is due to the self-heating phenomenon associated with the high loading condition. The test specimen upon unloading retains the mechanical deformation. The strain recovery is achieved by heating the specimen above austenite finish temperature (A_f).

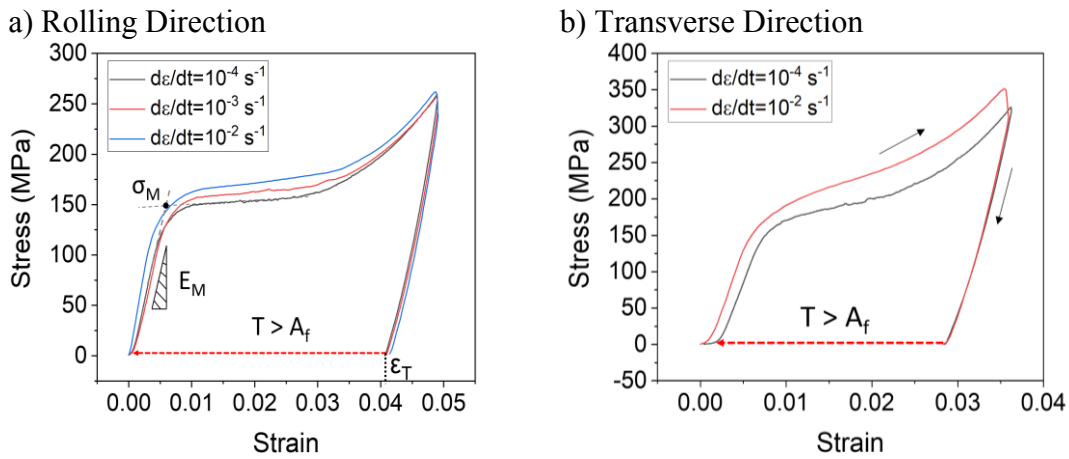

Figure 4.8: NiTi test strip along rolling direction shows a flat stress plateau during martenstite reorientation (a). The test strip along transverse direction does not have a sharp onset for martensite reorientation and reached strain hardening at low strain levels (b).

The mechanical behavior of a test strip cut along the transverse direction of the cold-rolled foil under tensile loading is indicated in Fig. 4.8(b). A higher loading stress is required along transverse direction than rolling direction for a similar deformation. During the orientation of martensite, a small increase in the stress is observed, owing to

Table 4.2: Summary of material parameters for one-way NiTi foil annealed at 450 °C

Parameter	**Symbol**	**Value**
Critical stress for Martensitic reorientation (at RT)	σ_M	150 MPa
Clausius–Clapeyron coefficient (loading)	C^M	5.76 MPa/K
Clausius–Clapeyron coefficient (M → A)	C^{MA}	9.88 - 10.92 MPa/K
Transformation strain	ε_T	0.041
Elastic modulus of Martensite	E_M	20e9 Pa
Latent heat (M → A)(-100 to 150°C)	L_{MA}	18200 J/kg
Ambient temperature	$T_{ambient}$	298 K
Heat transfer coefficient *	h	62.6 W/m^2/K
Thermal Relaxation time		1.36 s

** The parameter is estimated according to the supplementary data provided in [105].*

the formation of high density of dislocation within the type II twins. A strong increase of stress due to strain hardening is observed at low strain levels [106], [107]. Since the transverse direction of cold-rolled foil is not favoring an effective martensite detwinning, the devices are fabricated along rolling direction. The material parameters for one-way NiTi SMA foil characterized along the rolling direction is consolidated in Table 4.2. The simulation model utilizes these parameters to predict the behavior of one-way NiTi SMA strips and damper devices based on NiTi foils.

4.3 Device Fabrication

SMA devices are fabricated from cold-rolled SMA foil using lithography and laser micromachining. Fabrication by laser cutting is the quickest means to develop SMA devices. The single step fabrication approach allows for good control of the fabrication tolerances. However, the deposition of melted material during the cutting process introduces irregularities at the edges of the devices.

The fabrication using lithography is a versatile method for microfabrication. Devices with micrometer and sub-micrometer feature sizes could be fabricated by appropriate process steps using lithography. Owing to the chemical process involved in device fabrication, high quality devices without edge irregularities are obtained. However, the multi-step processing approach requires an optimization of individual process steps. Besides, the control of fabrication tolerance becomes rather challenging. The time required for device fabrication is also significantly higher compared to laser cutting approach. In this section, the SMA devices fabrication using lithography and laser cutting are explained.

4.3.1 Lithography

In the obtained condition, SMA foil of 30 µm thickness has a thick oxide layer, which has to be removed by a wet etching using buffered solution of HF and HNO_3. After oxide etching, the foil is attached to a silicon wafer using a thermal release tape as indicated in Fig. 4.9(a). Silicon wafer serves as the sample holder for the rest of the process steps.

Subsequently, a hard mask of 60nm gold is deposited as indicated in Fig. 4.9(b). The gold has a high etch selectivity with NiTi in buffered HF solution [108]. The gold could be deposited by sputtering or evaporation deposition. In evaporation deposition of gold, the adhesion of gold on SMA is not good enough to withstand the chemical processes. Therefore, a chromium layer of 7 nm is deposited before the gold deposition. However, during the following development stages, occasional mask peeling off from the foil surface, especially at locations of low feature size, is observed. By using sputter deposited of gold, the mask is more firmly adhered to the SMA surface. The retention of gold mask could be enhanced by sputter deposition of TiW on SMA before depositing gold

mask [109]. Apart from gold, sputter deposited silver is also suitable as a hard mask with high NiTi selectivity in buffered HF etching solution [108].

In the following process step, a positive photoresist is spin coated on top of gold mask as shown in Fig. 4.9(c). The photoresist is hardened by soft baking. In case of one-way SMA foil, soft baking step could introduce wrinkles in the foil due to the transformation to austenite phase. Therefore, it is preferred to avoid the soft bake step by letting it harden at room temperature over a time duration of 12 hours.

Subsequently, a photomask is aligned on top of the photoresist for contact lithography. The mask is aligned along the rolling direction of the SMA foil. The pattern transfer is achieved by UV exposure as shown in Fig. 4.9(d).

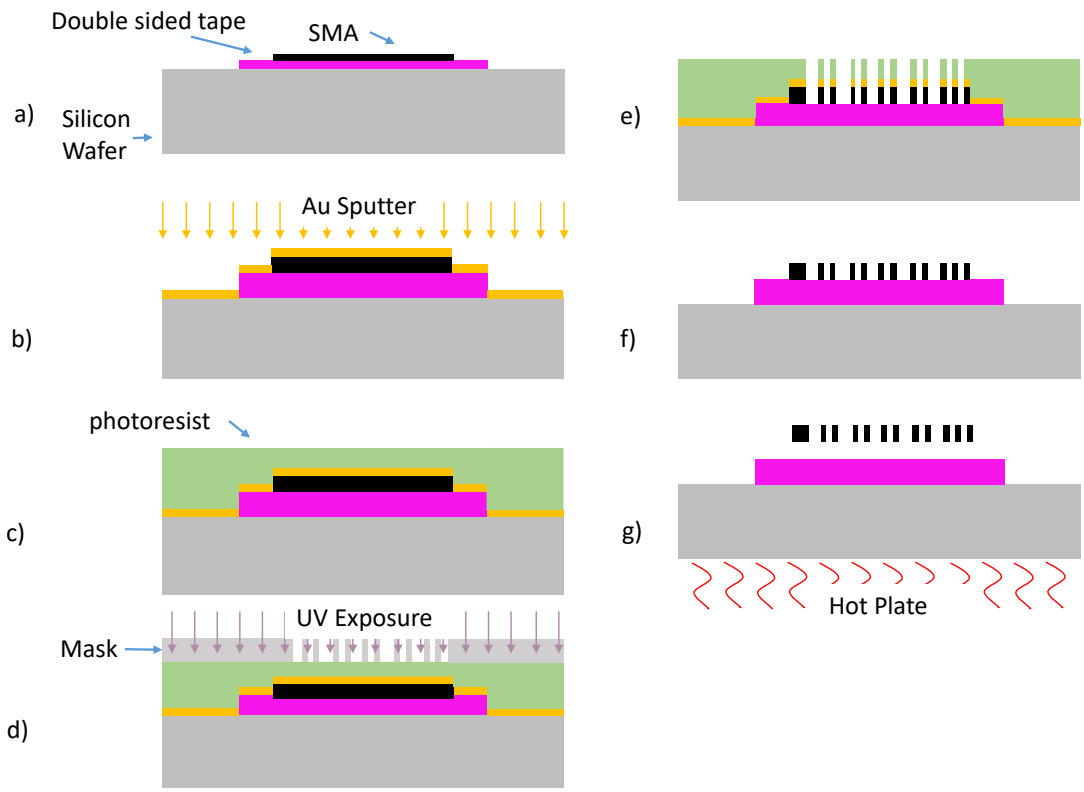

Figure 4.9: Lithography process flow of SMA device fabrication.

The pattern transfer to the SMA foil is achieved in the subsequent development and etching steps as indicated in Fig. 4.9(e). The photoresist after UV exposure is developed using developer solution. The gold mask exposed after photoresist development is etched using potassium iodide solution. If there is a chromium layer beneath as in the case of evaporation deposition, a subsequent chromium etch step exposes the SMA foil. A hard mask of silver could be etched away by using KI/ I_2 solution. In the following step, the SMA is etched using buffered solution of HF/ HNO_3/ H_2O. The wet etching of SMA foil

takes about 10 minutes to etch away the exposed foil, thereby transferring the pattern on to the foil. Subsequently, the residual photoresist and hard mask is removed from top of the SMA devices leaving behind SMA devices on silicon holder as shown in Fig. 4.9(f). The devices are removed from the holder by heating to 180 °C. At this temperature, the thermal release tape loses its adhesion and released the SMA devices from silicon substrate as indicated in Fig. 4.9(g).

4.3.2 Laser Micromachining

Fabrication by laser cutting allows direct transfer of patterns on the SMA foil. To be able to perform laser cutting, the wavelength of the laser should lie within the absorption spectrum of the material. The SMA foil attached to a silicon wafer holder using thermal release tape is micromachined using laser source of wavelength 1064 nm. The operation principle of laser is based on focusing high energy laser beam to a very small spot through suitable optics entailing tremendous rise in temperature resulting in ablation of the material. Owing to ablation, material re-deposition is observed at the edges of the laser cut devices. The high temperature developed on the material could also affect the material behavior. Spiral and folded beam devices used in this work having minimum feature sizes of 1 mm and 100 µm, respectively, are fabricated by laser cutting.

5 Pseudoelastic Damper Devices

Pseudoelastic damper devices are suitable for passive damping applications to protect objects or structures from shock loading. In this chapter, the behavior of pseudoelastic damper devices with bridge and spiral structures under quasi-stationary and dynamic loading conditions are investigated. The devices are made out of pseudoelastic NiTiFe foil described in chapter 3. The dynamic damping behavior is studied using free vibration experiment. The damping behavior of devices is compared using the specific damping capacity estimated from the oscillation behavior. In the following section, the test setups, measurement approaches and damping performance of bridge and spiral damper devices is presented.

5.1 Strip-based Four Bridge Damper Device

In a strip based bridge device, bridges of 1 mm width are cut-out from the cold-rolled foil using foil cutter. The damper device consists of four individual bridges connected to a mass of 65 g as shown in the schematic Fig. 5.1(a). PMMA based mass holder is attached to the middle of each bridges of dimension 40 x 1 x 0.03 mm^3. The bridges are pre-strained in the lateral direction using a micrometer head. The damping behavior at different pre-strain and loading amplitudes are investigated. The mass is excited to desired out-of-plane loading amplitude using an electromagnet as indicated in Fig. 5.1(b). The actual test setup is shown in Fig. 5.2(a).

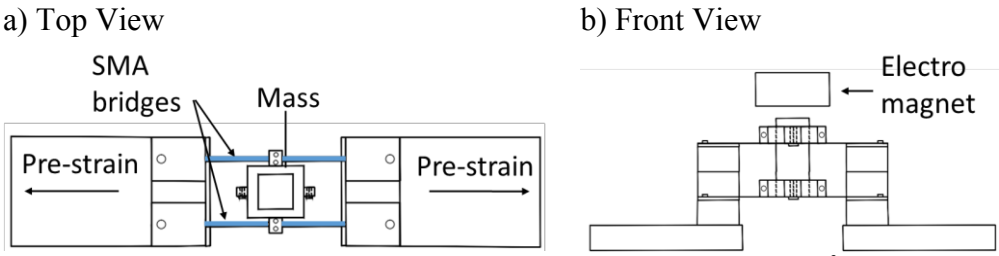

Figure 5.1: Schematic of strip based four bridge device of 40 x 1 x 0.03 mm^3 with lateral prestraining as indicated in top view (a). The front view of the setup with the electromagnet for excitation is shown in (b).

In the starting condition, electromagnet is kept in contact with the mass and activated to firmly hold the mass. The movement of the electromagnet is controlled using a micrometer head to precisely adjust the loading amplitude. Upon de-energizing the electromagnet, the mass is released to oscillate about its equilibrium. The movement of the mass is captured by a laser displacement sensor.

A sample oscillation behavior is shown in Fig. 5.2(b). The potential energy stored during the loading of the damper device is dissipated during the oscillation. Assuming a constant stiffness of the device during oscillation, the potential energy $U \propto x^2$. For a loading energy E_1, the specific damping capacity (SDC), as mentioned in Eqn. 2.20, for the first cycle of oscillation is

$$D = \frac{E_1 - E_2}{E_1} = 1 - \frac{x_2^2}{x_1^2} \tag{5.1}$$

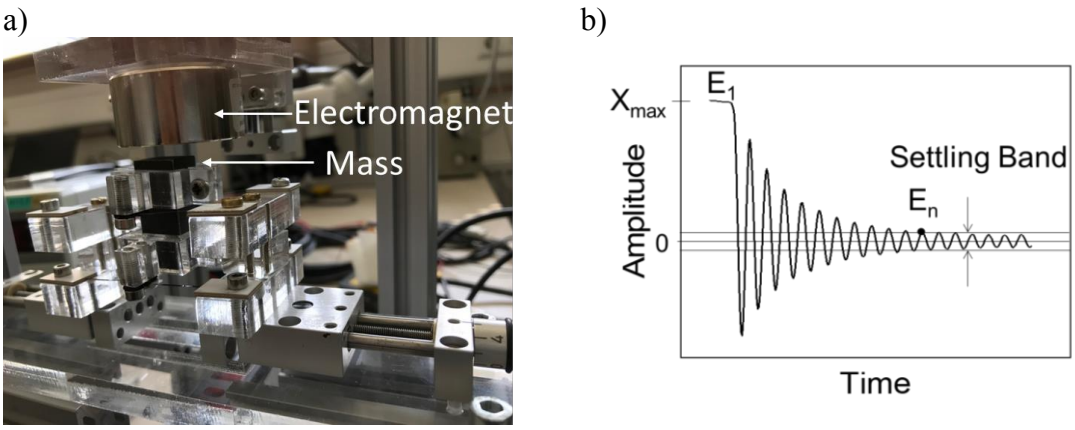

Figure 5.2: Test setup of the strip based damper device is shown in (a). The free oscillation of the mass is evaluated for a settling band of 10% as shown in (b) to estimate the average SDC per cycle.

The oscillations are analyzed until 10% settling band. The settling band is estimated from the peak to peak oscillation amplitude with respect to the equilibrium position. E_n is the energy of the last oscillation peak outside the 10% settling band. An average SDC per cycle is estimated by

$$Avg.\ SDC/cycle = \frac{1}{n}\frac{(E_1 - E_n)}{E_1} = 1 - \frac{x_n^2}{x_1^2} \tag{5.2}$$

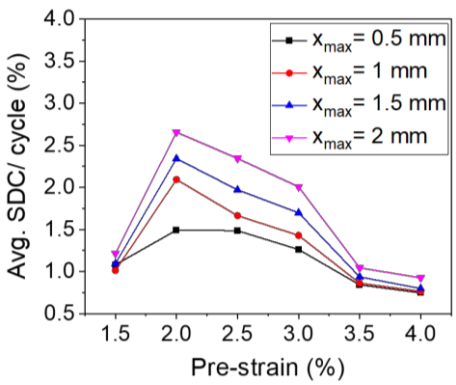

Figure 5.3: Avg. SDC/ cycle measured at room remperature shows a pre-strain dependent behaviour at different loading amplitudes. An optimal pre-strain of 2% could be observed. A high SDC is observed between 2 to 3% pre-strain.

The parameter Avg. SDC/cycle gives an estimate of the number of oscillation required to reach a pre-defined settling band. In contrast to the estimate of SDC for a single cycle, this parameter takes into account the elastic oscillations also, which is predominant at oscillations of low amplitudes in shape memory alloys.

The behavior of Avg. SDC/cycle with respect to pre-strain at various out-of-plane loading amplitudes are shown in Fig. 5.3. Optimal pre-strain of 2% is observed for loading amplitudes of 1 mm, 1.5 mm and 2 mm. These loading amplitudes corresponds to in-plane strains of 0.1, 0.3 and 0.5% respectively. The pre-strain between 2 and 2.5% is optimal for the loading amplitude of 0.5 mm. The optimal damping is observed close to the middle of the stress plateau when the combined strain due to pre-strain and loading amplitude lies within the maximum strain of 5%. Utilizing maximal pseudoelastic region is the criterion for high SDC. Therefore, the optimal pre-straining is expected to shift to lower values at high loading amplitude.

5.2 Cross Bridge Damper Device

SMA bridge devices are fabricated using optical lithography from a foil with a thickness of 30 µm. The foil is thinned down to 20 µm in the etching step to remove the oxide layer. The fabricated device has a length of 6 mm and width of 300 µm as shown in Fig. 5.4(a). Two bridge devices are antagonistically coupled to a mass of 0.3 g at the center of bridge devices. This test setup is referred as cross bridge damper device in this work. The pre-strain of the bridges is adjusted using spacers as shown in Fig. 5.4(b).

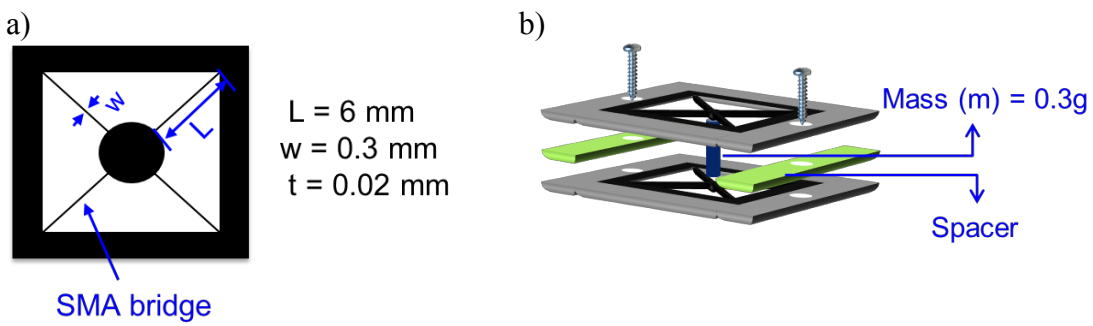

Figure 5.4: Schematic of SMA bridge device (a) and construction of cross bridge damper device (b). The pre-strain of the damper device is adjusted using spacers [110] .

5.2.1 Quasi-Static Behavior of Cross Bridge Damper Device

The quasi-stationary behaviour of the cross bridge damper device is investigated using out-of-plane loading at a displacement rate of 0.05 mm/s as shown in Fig. 5.5(a). The force-displacement behaviour in Fig. 5.5(b) indicates a force of about 3.2 N for a loading amplitude of 1.5 mm. At low loading amplitudes of up to about 0.8 mm the cross bridge

damper device behaves elastically and from 0.8 to 1.5 mm the material shows pseudoelastic behaviour.

The quasi-stationary behaviour of the cross bridge damper device is investigated using out-of-plane loading direction at a rate of 0.05 mm/s as indicated in Fig. 5.5(a). The force-displacement behaviour in Fig. 5.5(b) indicates a force of about 3.2 N for a loading amplitude of 1.5 mm. Therefore, cross bridge damper device has high stiffness suitable for damping applications involving large mass. At low loading amplitudes of up to about 0.8 mm the cross bridge damper device behaves elastically and from 0.8 to 1.5 mm the material shows pseudoelastic behaviour.

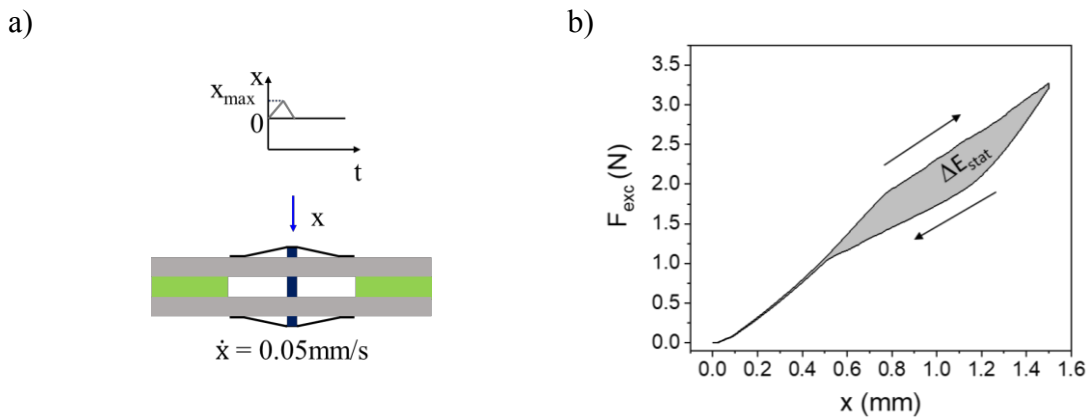

Figure 5.5: Schematic of the cross bridge damper device under quasi-stationary loading conding (a) and the corresponding force-displacement behaviour for a pre-strain of 0.17% (b).

Fig. 5.6 represents the force-displacement behaviour of the cross bridge damper device at different pre-strains and loading amplitudes. At a low pre-strain of 0.17%, the cross bridge damper device operates in elastic region at low loading amplitudes. Dissipation is observed for loading amplitudes above 0.7 mm. In the cross bridge damper device, the pre-straining using the spacers often introduces unsymmertric strains in the two antagonistic bridge devices. Therefore, an unsymmetric force-displacement behaviour is observed along positive and negative loading directions. At a pre-strain to 0.89%, the cross bridge damper device operates near to the beginning of pseudoelastic region, which is close to 1% strain as estimated from Fig. 4.4. The device operates in pseuoplastic region and dissipates energy by hysteresis for low loading amplitudes. During unloading, the strain recovery is achieved and the cross bridge damper device returns to its starting position when the load is completely removed. Upon further pre-straining in the pseudoelastic region, high hysteresis is observed even at low loading amplitudes as observed in the case of 1.98% pre-strain. However, a complete strain recovery is not obtained when the load is removed due to residual martensite. The hysteresis behaviour indicates the absence of elastic region under cyclic loading, dissipating high energy at low loading amplitudes.

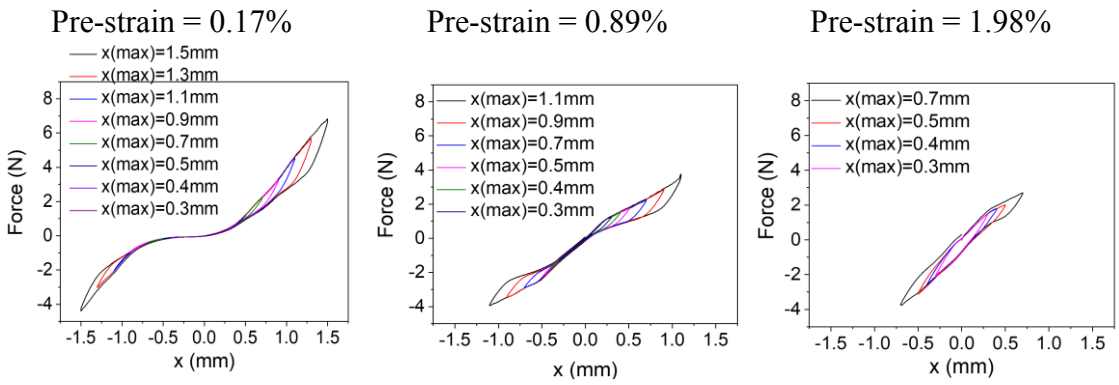

Figure 5.6: Quasi-stationary behaviour of the cross bridge damper device when pre-strained in elastic region (0.17%), near to the begininng of pseudoelastic region (0.89%) and in pseudoelastic region (1.98%).

The energy dissipation per unit volume of the cross bridge device is estimated from the enclosed hysteresis at various pre-strains and loading amplitudes from tensile testing at an a strain rate of 10^{-3} s^{-1}. Fig. 5.7 shows the energy dissipation density at various loading amplitudes (X_{max}) and pre-strains (ε_{pre}). The dissipation behaves non-linear for low pre-strains. The non-linear behavior is due to the existence of elastic and pseudoelastic regions that contributes to two types of dissipation behavior. At pre-strains above 0.89%, the dissipation behavior is almost linear. At pre-strain of 2.68%, the dissipation is linear at various loading amplitudes. A high energy dissipation is possible for small amplitudes by increasing the pre-straining. The SDC of the cross bridge damper device follows the trend of dissipation until the combined strain due to pre-straining and loading amplitudes are within complete martensite transformation. A further straining above the complete martensite transformation region still increases the energy dissipation but reduces the SDC due to the high input energy for straining above complete martensite transformation [91].

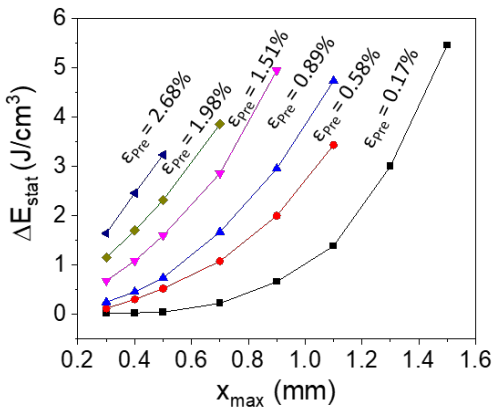

Figure 5.7: The behavior of energy dissipation with loading amplitudes at various pre-strains (ε_{pre}) under tensile loading at room temperature [110].

5.2.2 Dynamic Behavior of Cross Bridge Damper Device

The dynamic behavior of coupled SMA device is studied using a free oscillation test setup as shown in Fig. 5.8. A piston mechanism is used to excite the mass of the cross bridge damper device. The damper device is attached to a mass holder platform with the mass aligned with the piston. The piston is fixed on a piston holder that is connected to a piston platform. The micrometer head is connected to the piston platform, allowing precise movement of the piston. The movement of the mass is captured by a laser displacement sensor. After reaching desired loading amplitude of the mass, the piston mechanism is released using a released rod. When the release rod is pulled-out, the piston holder gets detached from the piston platform. The piston holder is pulled towards the base plate by the loaded springs connected between base plate and piston platform. The free oscillation behavior of the damper device is observed when the piston is released.

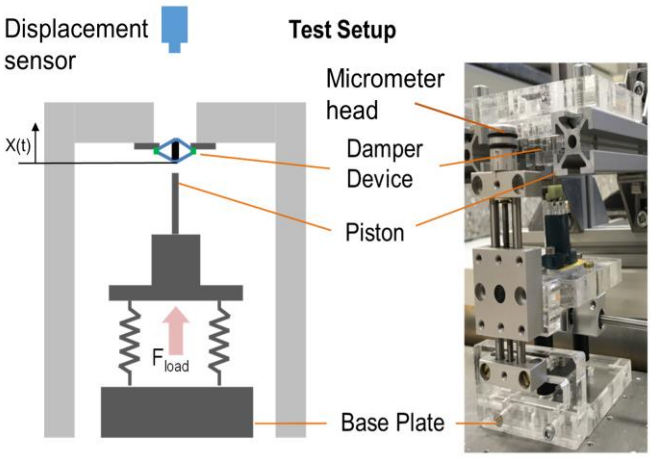

Figure 5.8: Schematic and actual test setup for the free oscillation testing of cross bridge damper device [110].

The oscillation behavior of the mass at two different pre-strain conditions for a loading amplitude of 0.3 mm is shown in Fig. 5.9(a). At pre-strain of 1.98%, the overshoot amplitude is significantly lower than 0.17% pre-strain. The increase in pre-straining results in increase in stiffness and thus increases the oscillation frequency. The oscillation settle down to the starting position at 0.17% pre-strain due to the operation in the elastic region as mentioned in section 5.2.1. The settling point deviates from the starting location in case of pre-straining at 1.98% due to the antagonistic operation in pseudoelastic region, where the unloading of one cross bridge device results in the loading of the other cross bridge device in the damper device.

The release point of the mass is indicated by 'A' and maximum overshoot amplitude is represented as 'B' in Fig. 5.9(b). The loading energy at 'A', U_A is estimated by the quasi-static tensile loading of the cross bridge device. The total energy dissipated, E_d, during the free oscillation arises from the material dissipation of the SMA (E_{dyn}) and dissipation due to air drag (E_{air}). It can be expressed as

$$E_d = E_{dyn} + E_{air} \tag{5.3}$$

The energy dissipated when the mass is moved from A to B is

$$E_d = U_A - U_B \tag{5.4}$$

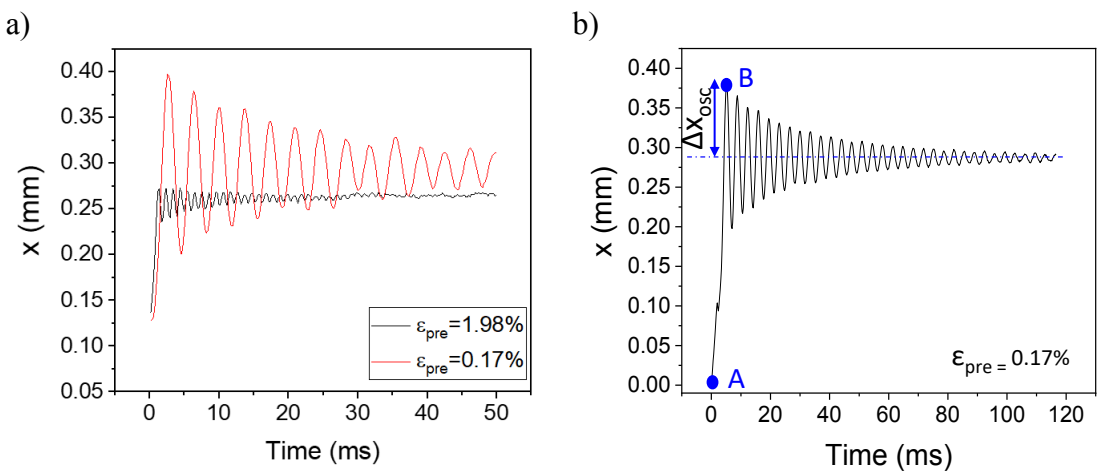

Figure 5.9: The comparison of oscillation behaviour of cross bridge damper device for a loading amplitude of 0.3 mm at pre-strains of 0.17 and 1.98% (a). The points A and B indicates the release of the mass and peak overshoot amplitude respectively (b).

The potential energy at point 'B' is

$$U_B = \frac{k \cdot \Delta x_{osc}^2}{2} \tag{5.5}$$

The stiffness of the coupled damper device is approximated as a constant stiffness and estimated from the frequency of oscillation as shown in Fig. 5.10(a). The frequency of oscillation increases about five-fold when the pre-strain is varied from 0.17 to 1.98%. The first peak oscillation amplitude, Δx_{osc}, shows a decreasing behaviour with the pre-strain as shown in Fig. 5.10(b). At no pre-strain condition, an increase in loading amplitude leads to an increase in overshoot amplitude, Δx_{osc}. An increase in pre-straining results in high opposing stiffness and enhanced material dissipation in the antagonistic operation of cross bridge damper device thereby reducing the peak oscillation amplitude.

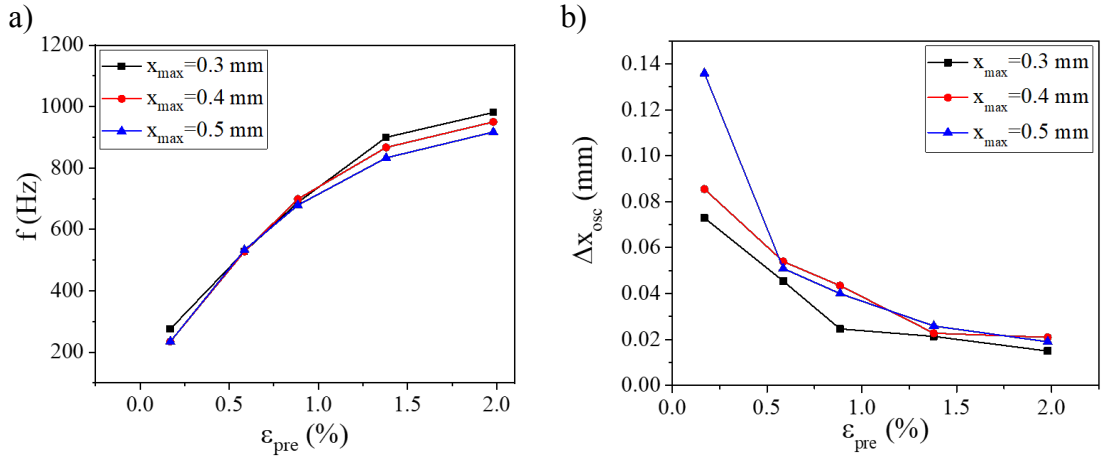

Figure 5.10: The behavior of oscillation frequency with respect to various pre-strains indicates an increase in the the stiffness of cross bridge damper device by prestraining (a). The peak overshoot amplitude decreases with increase in pre-straining due to high stiffness and enhanced material dissipation in cross bridge damper device during antagonistic operation (b).

In order to isolate the contribution of material dissipation and air drag on total energy dissipation, coupled damper device operation under elastic and pseudoelastic region is separately analysed. While operating in the elastic region, there is no material dissipation. Therefore, the energy is dissipated by air drag. At a pre-strain of 0.17% and loading amplitudes of 0.3, 0.4 and 0.5 mm, the operation of cross bridge device is in elastic region. At this condition, Eqn. 5.3 becomes

$$E_d = E_{air}$$
$$U_A - U_B = E_{air} \tag{5.6}$$

The pre-strain in pseudoelastic region at the same loading amplitude in elastic region mentioned above, dissipates loading energy by material dissipation and air drag. Even though, the loading condition is similar to the elastic region, the contribution of air drag is different from the estimated dissipation from Eqn. 5.6 due to the change in velocity after unloading. The energy dissipation by air drag is proportional to the square of velocity. A scaling factor is introduced in the estimated dissipation due to air drag as

$$n = \left(\frac{mass\ velocity\ (peak)\ during\ pseudoplastic\ loading}{mass\ velocity\ (peak)\ during\ elastic\ loading}\right)^2 \tag{5.7}$$

The consolidated energy dissipation is expressed as

$$E_d = E_{dyn} + n \cdot E_{air} \tag{5.8}$$

The contribution of material dissipation is estimated from

$$E_{dyn} = E_d - n \cdot E_{air}$$
$$E_{dyn} = U_A - U_B - n \cdot E_{air} \tag{5.9}$$

Fig. 5.11 shows the behaviour of dynamic dissipation at various pre-strains and loading amplitudes. The energy dissipation increases with both pre-strain and loading amplitude. The maximum dissipation of about 1.7 J/cm^3 at pre-strain of 1.98% and loading amplitude of 0.5 mm corresponds to a specific damping capacity of about 92%.

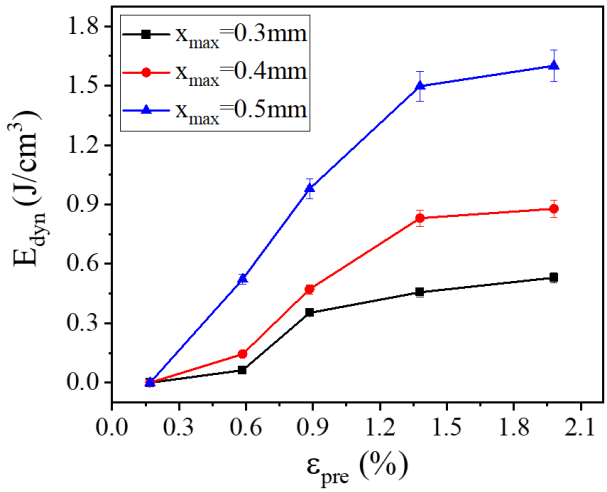

Figure 5.11: The behaviour of energy dissipation estimated from free oscillation experiment with respect to pre-straining conditions at various loading amplitudes [110].

5.2.3 Conclusion

The cross bridge damper device demonstrated high SDC up to about 92% under free oscillation testing condition. The counteracting feature of the antagonistic design and material dissipation is responsible for the high SDC in free oscillation testing. However, the pre-strain on each bridges cannot be controlled using spacers especially when pre-strained in the pseudoelastic region.

5.3 Bridge Device with Lateral Pre-strain

In order to allow for uniform pre-straining, the bridge devices are designed with parallel bridges and micromachined by laser cutting as shown in the inset of Fig. 5.12. The widths of the bridges are 265 µm. The devices are pre-strained using a micrometer stage along in-plane direction. The bridge device is quasi-statically loaded at a strain rate of 10^{-3} s^{-1}. The out-of-plane loading of 1.6 mm corresponds to 5% strain along each bridges. A high force of about 7 N is required for 5% strain as indicated in Fig. 5.12.

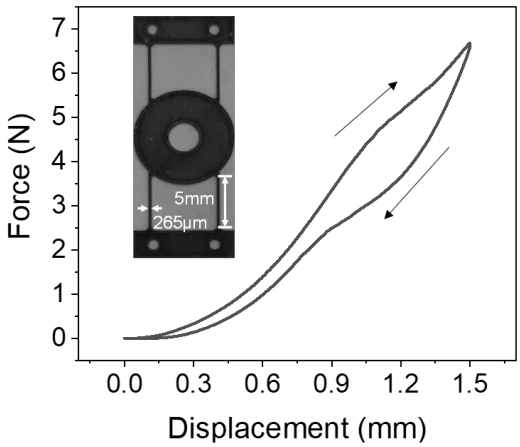

Figure 5.12: The behaviour of bridge device under quasi-stationary loading along out-of-plane direction at a strain rate of 10^{-3} s^{-1}.

5.3.1 Dynamic Testing of Bridge Damper Device

The dynamic testing of the bridge device is performed using free vibration test setup shown in Fig. 5.13(a). The bridge damper device consists of two bridge devices with a mass of 25 g at the center of the devices. An accelerometer is attached to the mass, allowing the sensing of translational Degree of Freedoms (DoFs) along x, y and z directions. The mass is excited using an electromagnet. The loading amplitude is adjusted using a linear actuator. The load cell connected to the electromagnet measures the force during the loading of the mass until it reaches the desired loading displacement amplitude. After reaching the desired loading amplitude, the mass is released and the free oscillation behavior of the mass is tracked using a laser displacement sensor.

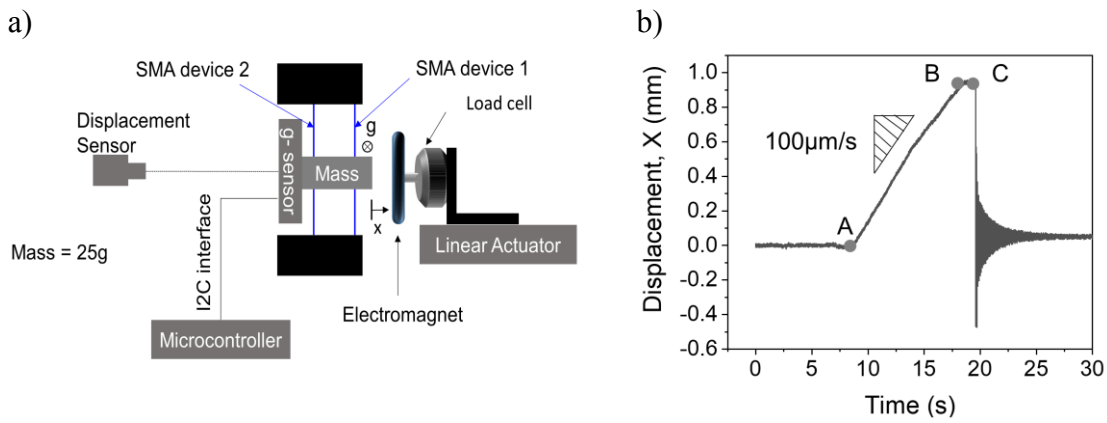

Figure 5.13: The schematic of free-oscillation test setup of the bridge damper device with lateral prestraining (a). The bridge damper device is loaded at a constant velocity of 100 µm/s using an electromagnet between 'A' and 'B'. The mass is released at 'C' and the resulting free oscillation is analysed as indicated in (b).

The test condition is illustrated by the time resolved displacement measurement using the laser displacement sensor in Fig. 5.13(b). In the starting stage, the actuator moves towards the equilibrium position of the mass and comes in contact with the mass. The electromagnet is activated at point 'A' and the mass is firmly attracted on to the electromagnet. The linear actuator is displaced at a constant velocity of 100 µm/s to ensure a constant loading rate. The desired loading amplitude is reached at 'B' and the mass is kept on hold for one minute to ensure a stable operation. The mass is released at 'C' and the resulting free oscillation behaviour is analysed to estimate the damping behaviour of the bridge damper device at different pre-strains and loading amplitudes.

The loading energy required for the bridge damper device for various pre-strains and loading amplitudes is shown in Fig. 5.14. The loading energy shows a non-linear behavior at low pre-strain condition up to about 1%. As mentioned in previous sections, the non-linear behavior is due to the operation in elastic and pseudoelastic region. At pre-strains above 1%, where the damper device is in pseudoelastic region the loading energy varies linearly with the loading displacement amplitude. A higher loading energy is required at high pre-strains than at low pre-strains to reach the same loading amplitude.

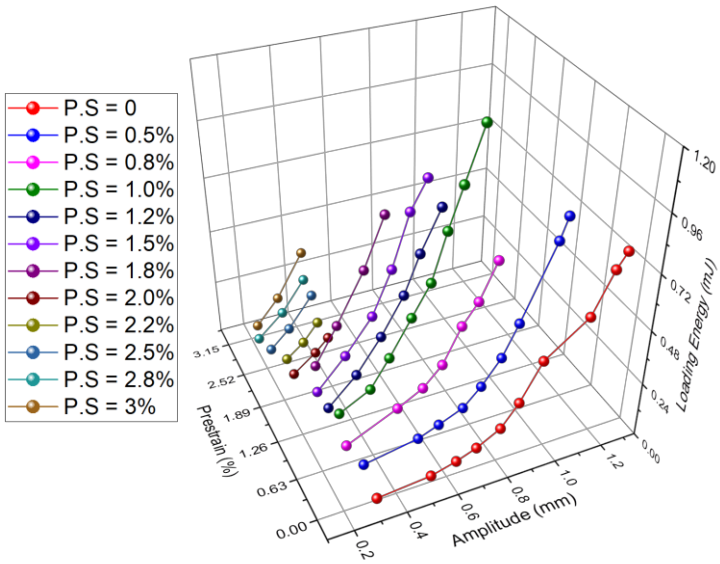

Figure 5.14: The behaviour of loading energy with respect to loading amplitudes at various pre-strains.

The specific damping capacity of the first oscillation cycle is evaluated using Eqn. 5.1 from the oscillation amplitude. The behavior of SDC at various loading amplitudes and pre-strain condition is shown in Fig. 5.15. SDC increases with both pre-strain and loading amplitude. Depending upon the loading amplitude the pre-stain can be adjusted to obtain maximum SDC by utilizing maximal pseudoelastic region. A maximum SDC of 70% is observed in this measurement.

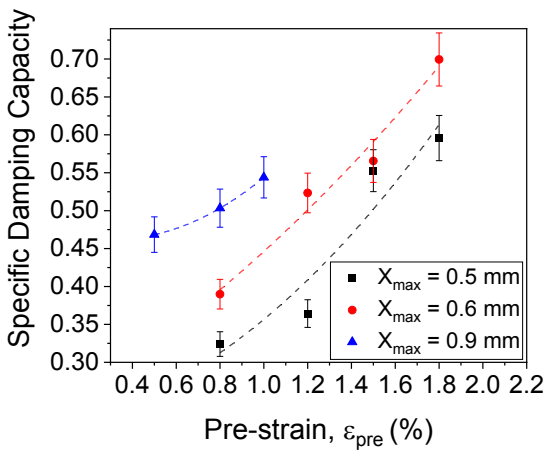

Figure 5.15: The behaviour of SDC at various pre-strains and loading amplitudes.

The 3D movement of the mass during the free oscillation is analyzed using a g-sensor connected to the mass. Fig. 5.16(a) shows the test condition, where the free oscillation of the mass is along the x direction, the device is pre-strained along y direction and the weight of the mass is along z direction. The acceleration along x, y and z directions for a pre-strain of 2.8% and a loading amplitude of 0.5 mm is shown in Fig. 5.16(b-d). The

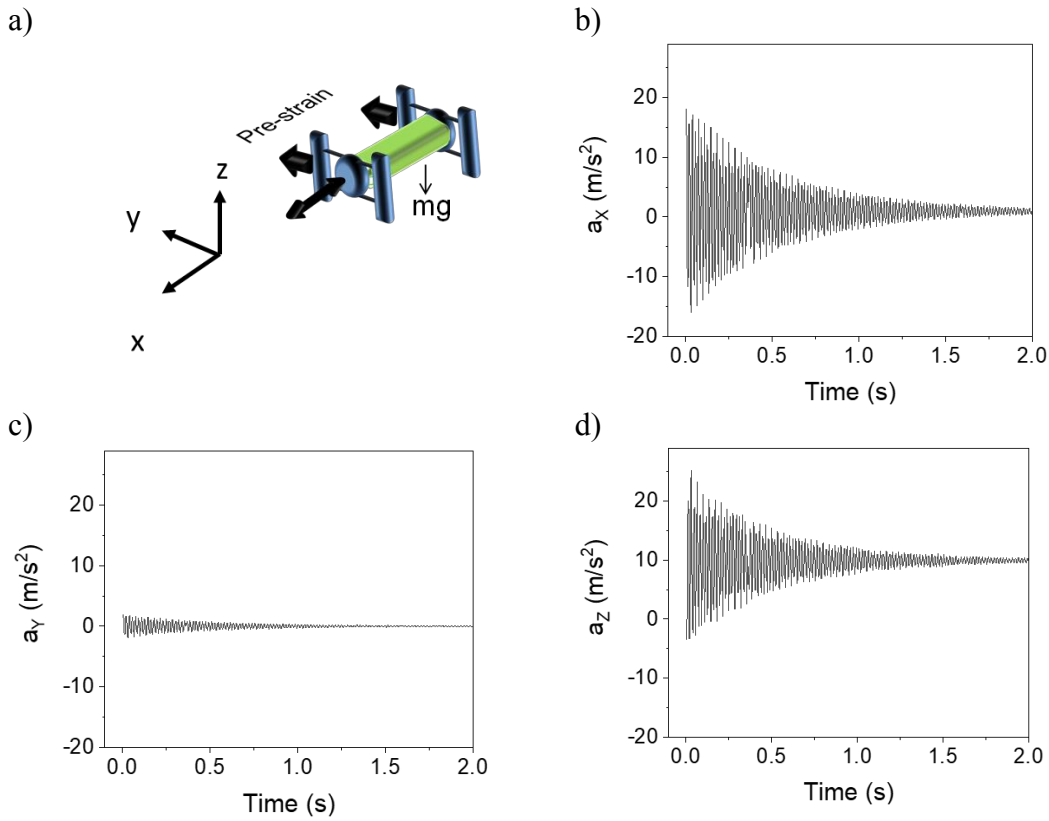

Figure 5.16: The orientation of the bridge damper device is shown in (a) with the movement of the mass excitation along x direction. The acceleration behaviour during the free oscillation of the mass along x, y and z directions for a loading amplitude of 0.5 mm and pre-strain of 2.8% (b-d).

acceleration behavior indicates that the movement is not only confined to the x direction. The mass oscillates also along z direction probably due to low stiffness resulting from bridge device sag under the effect of mass. The movement along y direction is constrained by the high stiffness along the bridges. Confining the mass movement using a linear guidance would allow single DoF movement.

5.4 Spiral Damper Device

The spiral device is micromachined by laser cutting from a foil of 30 µm thickness. The quasi-stationary behavior of the spiral device under various out-of-plane loading amplitudes is shown in Fig. 5.17. The spiral device allows large displacements at forces in the range of mN. At low loading amplitudes of up to 5 mm, a linear force-displacement behavior is observed. The loading amplitudes above 5 mm results in a non-linear behavior with a steep increase in the stiffness. In this region of operation, a small hysteresis behavior is observed indicating the dissipation due to phase transformation. Apparently, the spiral device has a predominantly elastic behavior arising from the design peculiarity of such device. The device is not uniformly loaded at high loading amplitudes. The resulting phase transformation is arising from localized regions of the spiral structure.

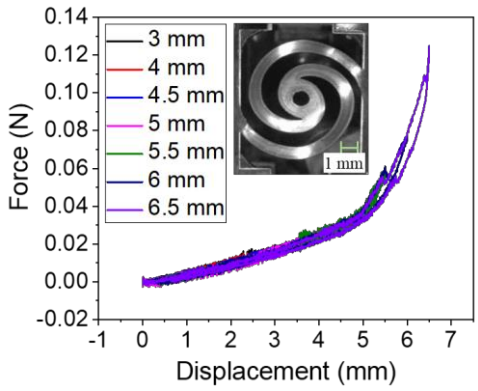

Figure 5.17: The quasi-stationary behaviour of spiral device under various out-of-plane loading amplitudes.

The free oscillation experiment is performed using two spiral devices connected with a mass of 1.3g at the center as shown in Fig. 5.18. The mass is excited using an electromagnet and the movement of the mass is captured using a laser displacement sensor. The pre-displacement is adjusted using spacers. Spacers of thicknesses 0.1, 0.3, 1 and 2 mm are used to adjust the pre-displacement. The oscillation behavior is investigated

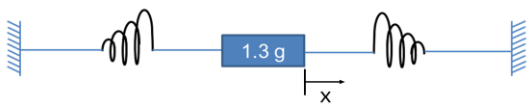

Figure 5.18: The test setup of spiral damper device with a mass of 1.3g.

to estimate the SDC of the damper device. The oscillations until a settling band of 10% is analyzed and the average SDC per cycle is calculated using Eqn. 5.2.

The behavior of peak overshoot amplitude with respect to pre-displacements at various loading amplitudes are shown in Fig. 5.19(a). The overshoot amplitude increases with the loading amplitude owing to the elastic behavior of the spiral device. By increasing the pre-displacement, the overshoot amplitude reduces due to the increase in stiffness of the

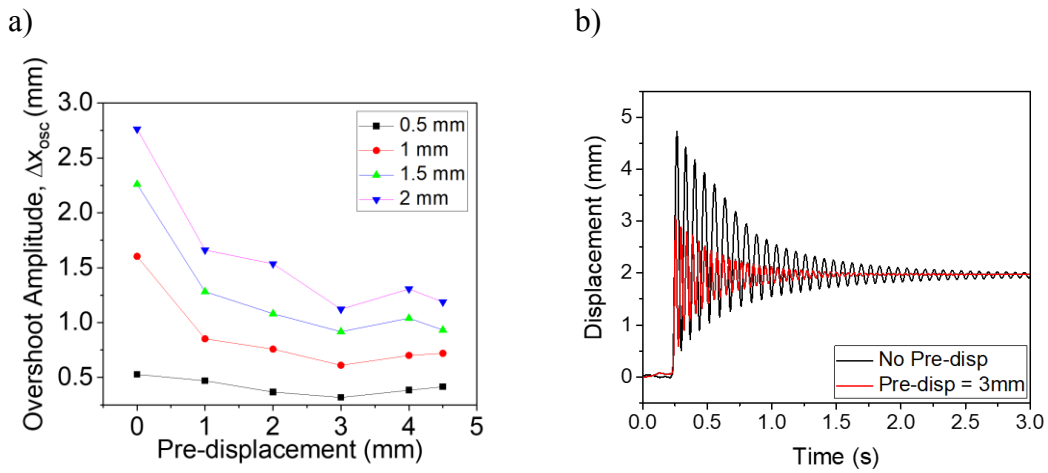

Figure 5.19: The behaviour of overshoot amplitude for various pre-displacement and loading condition is shown in (a). The oscillation behaviour in (b) indicates about one-third reduction in first oscillation amplitude by adjusting the pre-strain to 3 mm.

spiral damper device. Fig. 5.19(b) compares the time resolved oscillation behavior for a loading amplitude of 2 mm at two different pre-displacement conditions. The unsymmetric oscillation arises from the relatively higher stiffness of the bottom spring device pre-displaced by mass under the effect of gravity. About one-third reduction in the first oscillation peak is observed with a pre-displacement of 3 mm than at no pre-displacement condition.

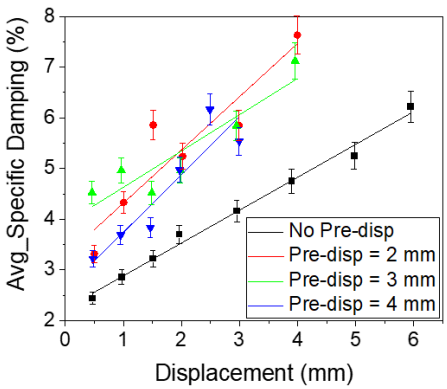

Figure 5.20: The behaviour of Avg_SDC under various loading amplitudes and pre-displacement is shown in (a). The avg_SDC is evaluated by considering a settling band of 10%.

The behavior of peak overshoot amplitude with respect to loading amplitudes at various pre-displacements are shown in Fig. 5.20. At no pre-displacement, SDC increases linearly with loading amplitude due to predominantly linear behavior of the spiral device. SDC increases with pre-displacement up to about 3 mm. Thereafter, SDC reduces due to the increase in device stiffness with pre-displacement.

6 Damping using One-way Shape Memory Alloys

One-way SMA allows for active and semi-active vibration damping through counteracting force upon heating above austenite finish temperature and stiffness/damping variation depending on the applied temperature. In this chapter, the thermo-mechanical behavior of bridge, spiral and folded beam structures are studied to understand their damping behavior. The one-way SMA damper devices are manufactured from cold-rolled $Ti_{50.18}Ni_{49.82}$ foils. The damping behavior of SMA devices are investigated by free vibration experiments at various pre-strain and loading conditions. The details about the testing procedure and estimation of damping and vibration control performance are presented here.

6.1 Bridge Device with Lateral Pre-strain

The bridge devices are micromachined by laser cutting from a NiTi one-way foil of 30 µm thickness. These devices are quasi-statically loaded at strain rates of 10^{-3} and 10^{-4} s^{-1}. The resulting out-of-plane force-displacement behavior is shown in Fig. 6.1(a). A force of about 1.7 N results in a displacement of 1.5 mm. By increasing strain rate, a higher loading force is required to initiate martensite re-orientation due to the self-heating phenomenon. Upon unloading, the deformation is almost completely retained with slight elastic recovery. The recovery of deformation is obtained by heating the device above

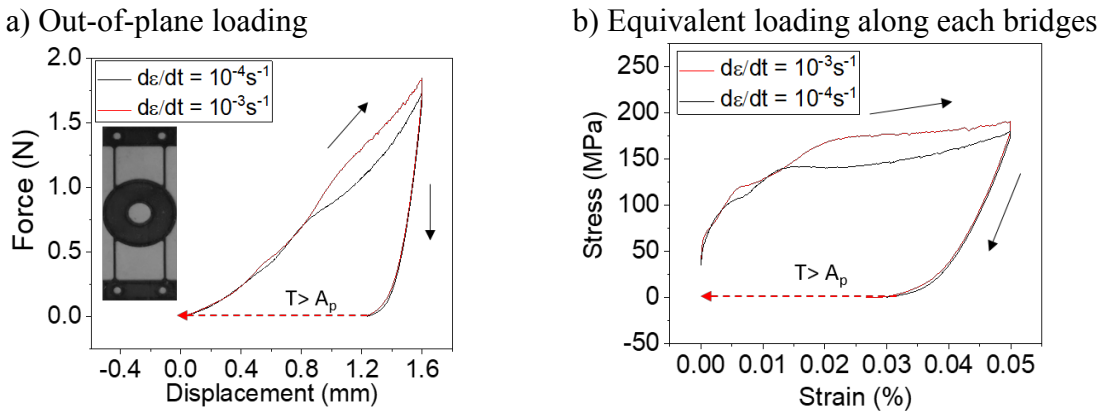

Figure 6.1: The force-displacement behavior of bridge device under quasi-stationary loading at strain rates of 10^{-3} and 10^{-4} s^{-1}(a). The equivalent stress-strain behaviour along each bridges of the bridge device is indicated in (b)

austenite finish temperature. The equivalent stress-strain behavior along each bridges of the bridge device is shown in Fig. 6.1(b). The critical stress is observed at a stress of about 150 MPa at a strain rate of 10^{-3} s^{-1}. A strain of 5% is attained along each bridges for the out-of-plane deflection by 1.5 mm.

6.1.1 Estimation of Cooling Time for Bridge Device

The one-way SMA devices require a heating pulse sufficient to heat the device above austenite finish temperature for shape recovery. The heating pulses are applied by Joule heating using a current source. The duration of heating pulse is selected based on the eigenfrequency of the system ensuring that the device is heated within one cycle of oscillation. From the experimental estimation of eigenfrequency, a current pulse duration of 50 ms is considered to study the effect of temperature rise and cooling time as shown in Fig. 6.2. The temperature rise of the bridge is tracked using an infrared camera and the temperature at the middle of the bridge is averaged on an area of 250 × 200 μm^2 as indicated by the highlight in Fig. 6.2(a) . The corresponding temperature rise shows a square dependence with current. The cooling time is investigated from the time-resolved temperature behaviour of the bridge device after removal of the current pulse. The time to cool down to 90% of the maximum attained temperature is indicated in Fig. 6.2(b). From the DSC measurement, the austenite finish temperature is estimated as 59.1 °C. This criterion is achieved by current pulse above 1.15 A. The cooling time of the device does not show significant variation with current pulses and lies between 1.2 and 1.36 s.

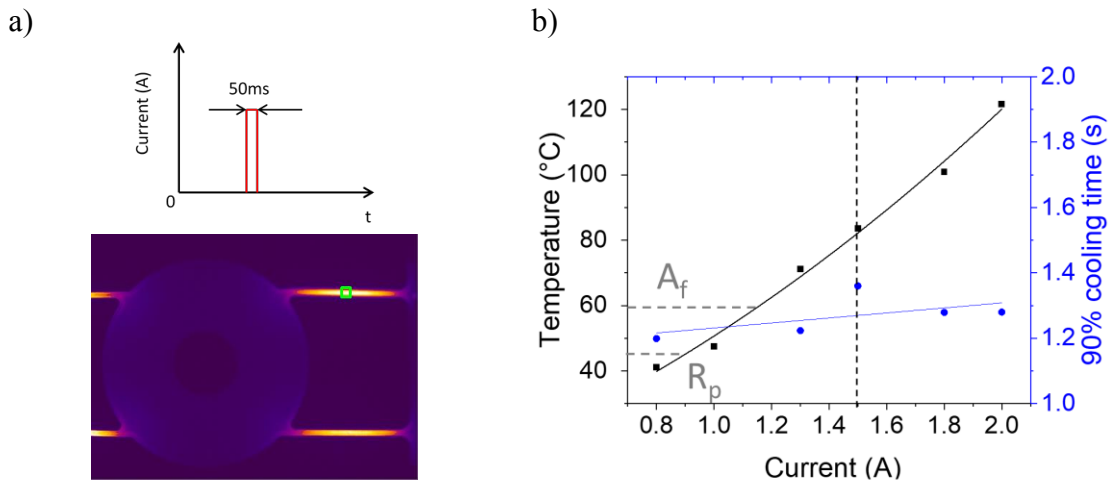

Figure 6.2: The Infrared thermography at the middle of the bridge averaged on an area of 250 × 200 μm^2 for a current pulse of 50 ms (a) and the corresponding temperature rise vs current pulse amplitude and cooling time for various currents is indicated in (b).

The cooling time is a crucial parameter which determines the effectiveness of multiple current pulses in damping and vibration control application. After applying a current pulse, the device has to be cooled down below Martensite finish temperature before

applying the next pulse to achieve high energy dissipation. As mentioned in section 4.2, the NiTi material shows an intermediate R-phase and remains in this phase at room temperature. Below 40 °C, the material is transformed to R-phase. Using this information, the cooling time of the bridge device is evaluated for the cooling down to 30 and 40 °C as indicated in Fig. 6.3. After heating the bridge device above 70 °C, the cooling time of the bridge device is more than 1.1 s to reach 30 °C. The cooling time increases with the increasing amplitude of the current pulse due to high temperature rise. The optimal performance is achieved by cooling the bridge device to 40 °C. The fastest time to cool from about 73 °C to 40 °C is 0.58 s. Further improvement in the cooling time is required to enhance the performance of the bridge device for vibration damping as well as control applications.

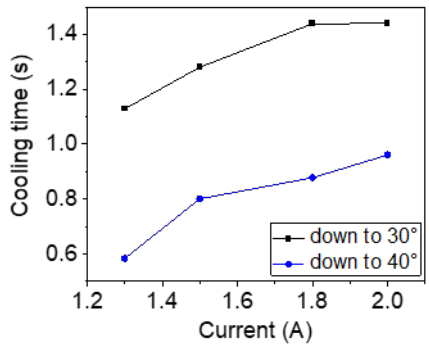

Figure 6.3: Cooling time vs current pulse amplitude for cooling down of the bridge device to 30 and 40 °C indicates a cooling time of above 1.1s to cool down to 30 °C after the application of current pulse.

6.1.2 Free Oscillation Test Setup

The dynamic damping behavior of the bridge device is investigated using a free oscillation test setup as indicated in Fig. 6.4 (a, b). The bridge damper device consists of a mass of 18g connected between two bridge devices and the mass is excited using an electromagnet. The bridge devices are pre-strained along the bridges as indicated in Fig. 6.4 (a). The position of electromagnet is adjusted using a micrometer head. When the electromagnet is deactivated, the mass oscillates and the corresponding movement is captured using a laser displacement sensor. During the oscillation of the mass, current pulses are applied at terminals V1 and V2 to enhance the damping performance arising from phase transformation. In the following section, the operation of the bridge damper device at various operating conditions is illustrated.

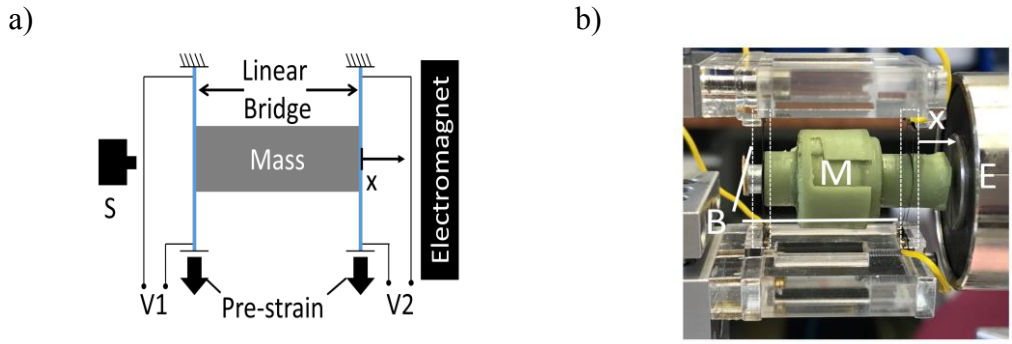

Figure 6.4: Schematic of the free oscillation test setup (a) and the actual test setup comsisting of two bridge devices with a mass at the center (b). M – Mass, B – Bridge devices, E – Electromagnet, x – Oscillation.

6.1.2.1 Vertical Configuration

In the vertical configuration, the mass is kept vertical, thereby loading the bridge damper device in out of-plane direction by gravity as indicated in Fig. 6.5 (a). After the release of the mass from the electromagnet, a current pulse is applied simultaneously on both bridge devices when the mass travels 0.3 mm. The current pulse of 1.5 A is applied for 50 ms to introduce austenite phase transformation. Fig. 6.5(b) represents the time-resolved mass oscillation for a loading amplitude of 1 mm at no pre-strain condition. The eigenfrequency of the system is 41 Hz without the application of heating pulse. The application of heating pulses worsens the oscillation behavior. A magnified oscillation behavior and shift in the equilibrium position is observed with the application of heating pulse. Both these phenomena arise due to the pre-straining of the bridge devices by the mass under the action of gravity. The application of short current pulse transforms the bridge devices to austenite, introducing a strong out-of-plane actuating force resulting in an enhanced oscillation of the mass. Besides, the equilibrium position is also shifted by the application of current pulse due to the shape recovery of bridge device that is pre-strained by the mass.

The stress-strain behavior of the bridge device during the free oscillation without any heating pulse is illustrated in Fig. 6.5 (c). 'I_0' represents the initial external pre-straining state in the device. Additional straining is introduced by the mass and the corresponding state is shown as 'S_0'. Now the damper device is externally loaded to desired amplitude and the respective state is denoted as 'S_1'. After the mass release from electromagnet, a new equilibrium state 'S_0'' is attained. The peaks of oscillations are represented by states S_2 and S_3.

The stress-strain-temperature behavior of the bridge device when a heating pulse is applied is illustrated in Fig. 6.5(d). The loading behavior until state 'S_1' is same as mentioned above. Upon unloading, a heating pulse is applied at state 'S_2' resulting in phase transformation to austenite. Correspondingly, the bridge device shows a

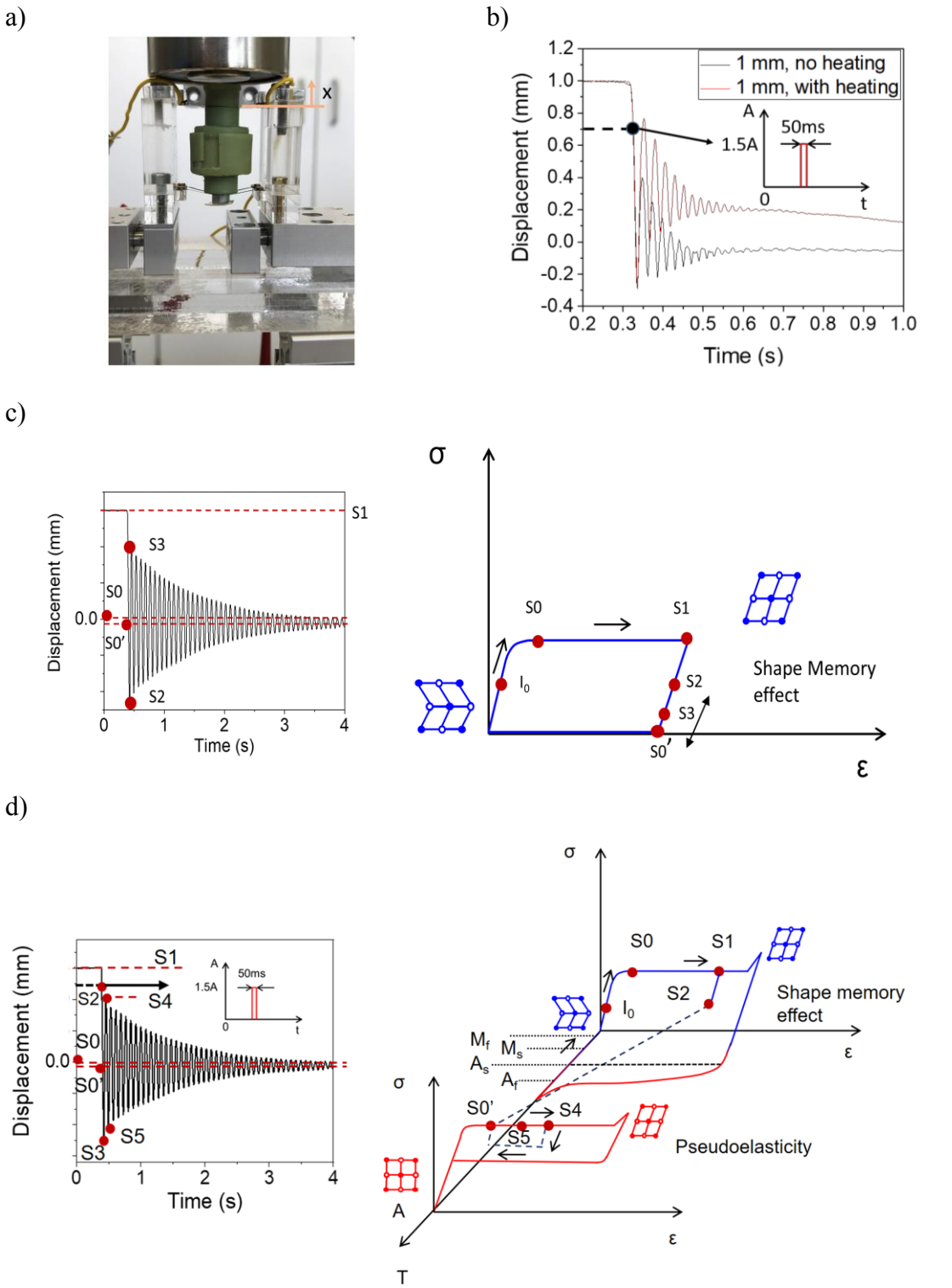

Figure 6.5: Photo of vertical configuration of the bridge damper device is shown in (a) and the time resolved mass oscillation with/ without the application of heating pulse indicates enhanced oscillation with the application of heating pulse (b). The illustration of stress-strain states corresponding to the free oscillation without the application of current pulses (c). The representation of stress-strain-temperature states during free oscillation with the application of current pulse (d).

pseudoelastic behavior with the new equilibrium state 'S_0''. Assuming one cycle of oscillation for heating above austenite finish temperature, the peaks of oscillations S_4 and S_5 are represented by states in pseudoelastic behavior.

The specific damping capacity (SDC) of the bridge damper device is estimated from the oscillation behavior considering first cycle of oscillation. The damping arises from martensite reorientation in the first oscillation cycle. From second cycle of oscillation onwards, the amplitude reduction is arising from air drag. Fig. 6.6(a) represents the SDC behavior of the bridge damper device without application of heating pulse. SDC increases with the increase in loading amplitude from 1 mm to 1.5 mm and lies between 83 and 92% for all pre-straining conditions. The high SDC is attributed to the softening effect arising from the residual strains after unloading. The highest SDC of 92 % is observed for a pre-strain of 3% at a loading amplitude of 1.5 mm. The corresponding oscillation behavior is indicated in Fig. 6.6(b). An amplitude reduction of 73% is observed in the first oscillation cycle without application of current pulse. By the application of current pulse, the damping performance worsens due to out-of-plane actuation of the SMA.

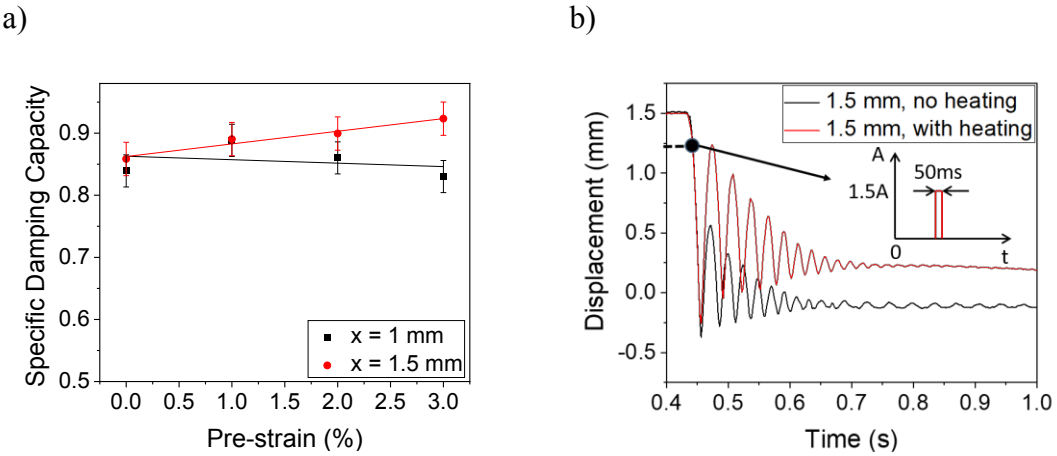

Figure 6.6: SDC measurement of bridge damper device with respect to pre-straining at various loading amplitudes without the application of current pulses (a). The time resolved mass oscillation corresponding to maximum SDC of 92% for pre-strain of 3% and loading amplitude of 1.5 mm is shown in (b).

6.1.2.2 Horizontal Configuration

In the horizontal configuration of the bridge damper device, the mass is kept in horizontal position as indicated in Fig. 6.7(a). The bridge devices are not pre-strained along the out-of-plane direction. The oscillation behavior of the mass with and without the application of heating pulse for a loading amplitude of 0.5 mm under no pre-strain condition is shows in Fig. 6.7(b). The applied current pulse has an amplitude of 1.5 A and a pulse duration of 50 ms as in the case of vertical configuration. The equilibrium position of the oscillation does not shift with the application of current pulse, due to the absence of out-of-plane pre-straining of the bridge devices.

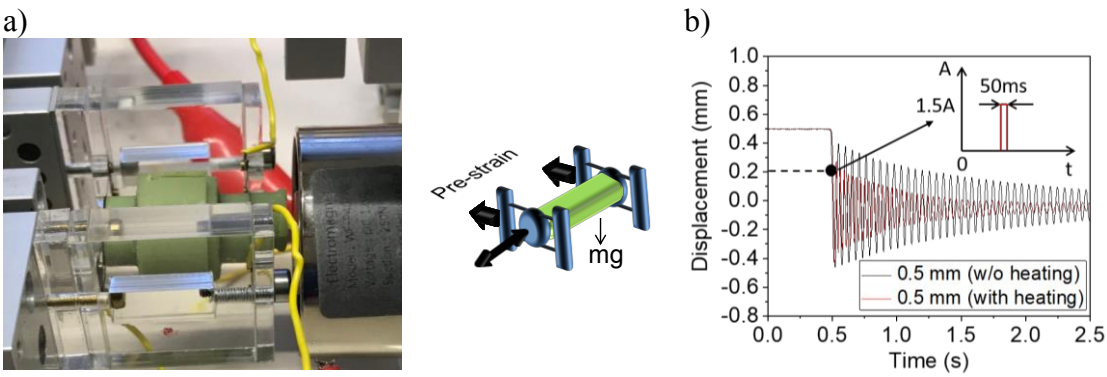

Figure 6.7: The picture of the horizontal configuration of bridge damper device is shown in (a). The mass oscillation under no pre-strain condition for a loading amplitude of 0.5 mm is shown in (b).

The SDC of the bridge damper device in the horizontal configuration is estimated for the first oscillation cycle from the amplitude of oscillation. Fig. 6.8 indicates the behavior of SDC at various pre-straining (PS) conditions. The application of heating pulse results in an improvement in the SDC at all pre-straining conditions. The SDC lies between 0.2 and 0.6 without the application of heating pulse.

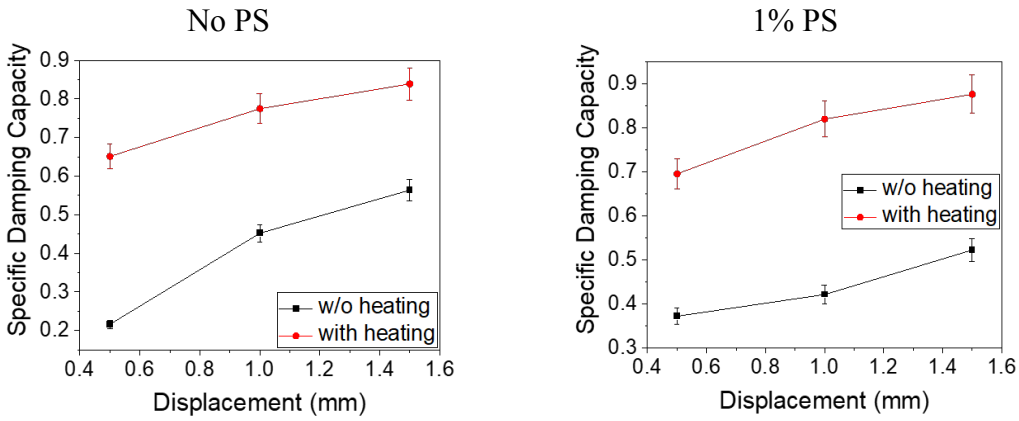

Figure 6.8: The comparison of SDC behavior at various pre-strain conditions with and without the application of heating pulse.

The frequency behavior of the bridge damper device under various loading conditions is illustrated in Fig. 6.9. When no current pulse is applied, the oscillation frequency increases with pre-strain at loading amplitudes below 1 mm due to increase in stiffness of the bridge damper device as shown in Fig. 6.9(a). At loading amplitudes above 1 mm, the softening effect due to the self-accommodated martensite variants dominates and the frequency of oscillation reduces when no current pulse is applied. When the current pulse is applied, the oscillation behaviour depends only on device pre-strain as shown in Fig. 6.9(b). The loading amplitude does not affect the oscillation frequency due to the absence of softening effect in the austenite phase by the application of current pulse.

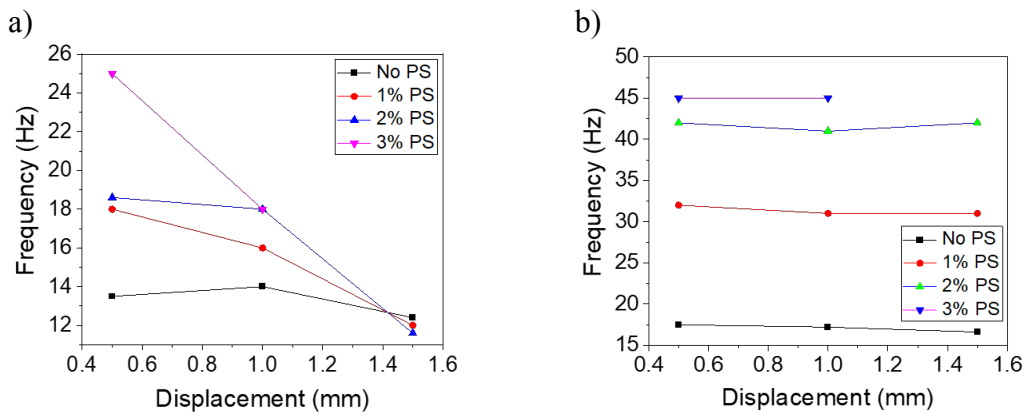

Figure 6.9: Frequency vs loading amplitude of the bridge damper device at various pre-straining condition without the heating pulse indicates a softening behaviour with high loading amplitudes (a). An increase in operating frequency is observed by the application of current pulse(b).

The behavior of SDC with respect to pre-strain at various loading amplitudes are indicated in Fig. 6.10(a). The SDC increases with increase in loading amplitude with the application of current pulse. A maximum DSC of 90% is observed for a pre-strain of 2% and loading amplitude of 1.5 mm. The range of SDC lies within the range of 55 to 90%. The oscillation behaviour corresponding to the maximum SDC is shown in Fig. 6.10 (b). An amplitude reduction of about 73% is observed with the application of current pulse. Owing to the high stiffness in austenite phase, the frequency of oscillation increases from 12 Hz (without current pulse) to 42 Hz with the application of current pulse.

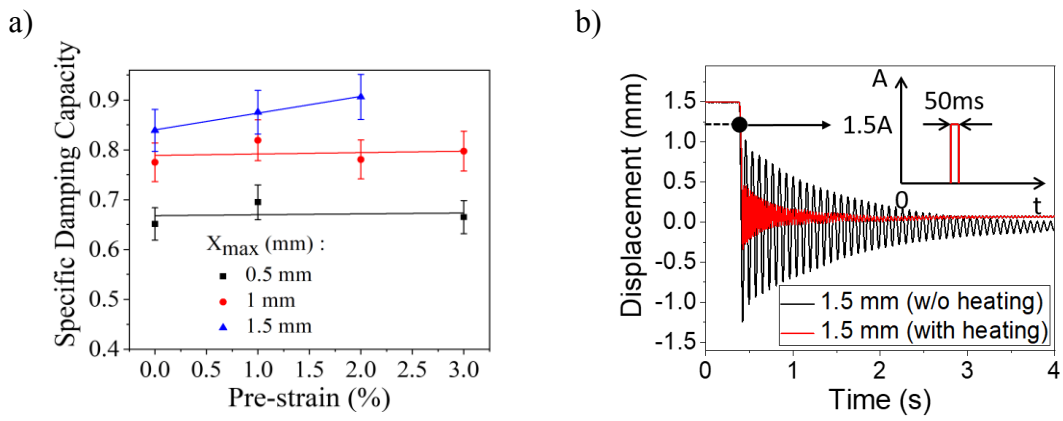

Figure 6.10: The behaviour of SDC with pre-strain with the application of current pulse (a) and the oscillation behavior corresponding to the maximum damping capacity of 90% at pre-strain of 2% and loading amplitude of 1.5 mm (b).

6.1.2.3 Hanging Configuration

In hanging configuration, the mass is kept hanging on the two bridge devices as indicated in Fig. 6.11(a). Each bridge devices are asymmetrically pre-strained by the hanging mass. The test conditions in the hanging configuration is same as other configurations for the bridge damper device. The current pulse of 1.5 A is applied for 50 ms when the mass moves 0.3 mm after the release from the electromagnet. The oscillation behavior of the mass for a loading amplitude of 0.5 mm under no pre-strain condition is indicated in Fig. 6.11(b). The application of current pulse reduces the oscillation amplitude and improves the settling time.

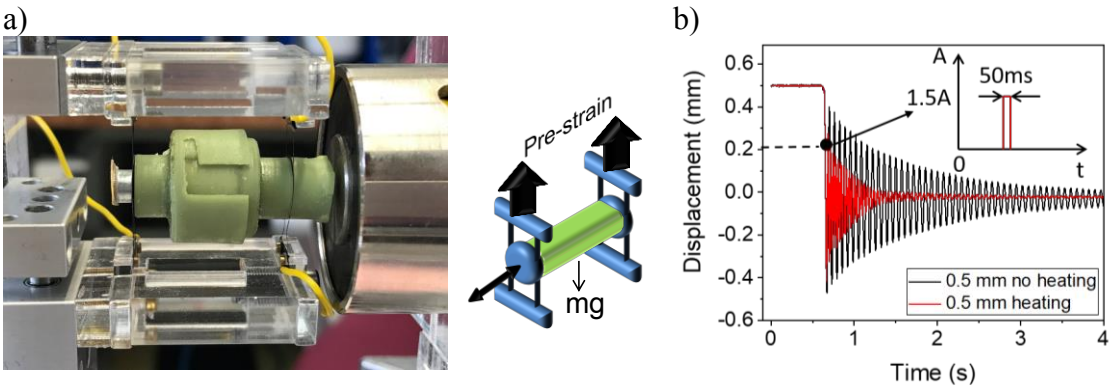

Figure 6.11: The photo of bridge damper device in hanging configuration (a). The time resolved mass oscillation under no pre-strain condition and loading amplitude of 0.5 mm indicates high amplitude reduction and quick settling with the application of current pulse (b).

The SDC for the first cycle is estimated from the mass oscillation amplitude. The first oscillation cycle shows the maximum reduction in oscillation amplitude owing to the austenite transformation by the current pulse. Fig. 6.12(a, b) represents the effect of current pulse on the SDC behavior at 1% and 2% pre-straining conditions. SDC shows an increasing trend with the loading amplitude due to large strain recovery upon austenitic phase transformation. In the absence of current pulse, SDC lies below 60%.

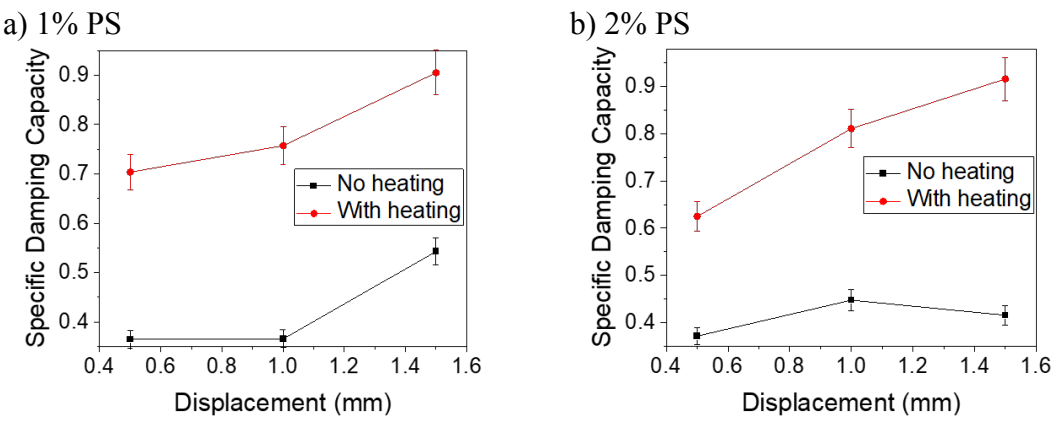

Figure 6.12: SDC vs loading amplitude of bridge device under hanging configuration at pre-strains of 1% (a) and 2% (b).

The behavior of frequency for the bridge damper device at various loading amplitudes and pre-strain conditions are shown in Fig. 6.13(a). A reduction of oscillation frequency is observed for high loading amplitudes due to the softening behavior of the bridge damper device. The frequency of oscillation doubles by the application of current pulse as shown in Fig. 6.13 (b). The absence of softening effect in austenite phase results in a constant behavior with the loading amplitude. The frequency of oscillation depends only on pre-straining under the application of current pulse.

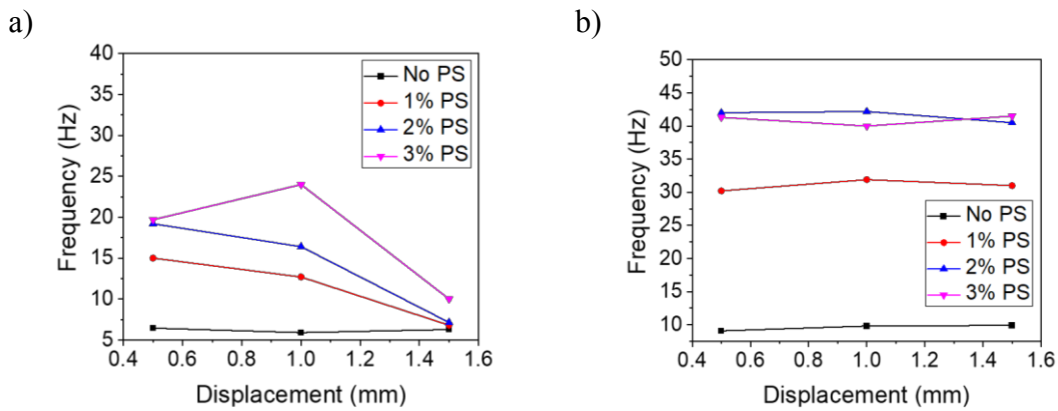

Figure 6.13: The frequency vs loading amplitude of bridge damper device without and with the application of current pulse is shown in (a) and (b) respectively.

The behavior of SDC with respect to pre-strain at various loading amplitudes is shown in Fig. 6.14(a). SDC depends strongly on the pre-straining condition. SDC increases rapidly until 1% pre-strain. The asymmetric pre-straining on the bridge device in the hanging configuration is responsible for this behavior at low pre-strain condition. An optimal pre-straining condition exists between 1% and 2% pre-strain. At this pre-straining condition, all bridges of the bridge devices contribute to the dissipation. A further increase of pre-strain results in reduction of SDC due to loading above the region of oriented martensite.

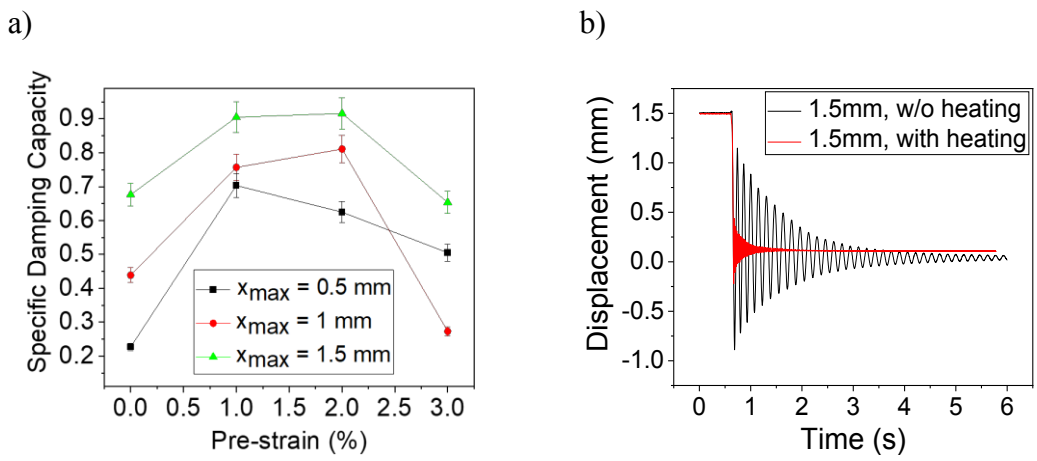

Figure 6.14: (a) SDC vs Pre-strain at various loading amplitudes shows an optimal pre-straining between 1 and 2% . The mass oscillation corresponding to the maximum SDC at 2% pre-strain and loading amplitude of 1.5 mm is shown in (b).

The maximum SDC of 91.6% is observed for a pre-strain of 2% and loading amplitude of 1.5 mm. The corresponding oscillation behaviour and effect of current pulse is shown in Fig. 6.14(b). The first peak oscillation amplitude reduces about one-third and settling time reduces by one-sixth by the application of current pulse.

6.1.2.4 Conclusion

The bridge devices demonstrate high SDC under free oscillation testing condition. The high SDC is associated with the residual deformation of the one-way bridge device under unloading condition and the phase transformation arising from the heating pulse. Among the vertical, horizontal and hanging configuration, enhancement in SDC by the application of current pulse is observed in horizontal and hanging configuration, where the bridge devices are not pre-strained along the out-of-plane direction by the proof mass under the effect of gravity. Maximum SDC of 90 and 92% is observed for horizontal and hanging configuration respectively. The application of current pulse does not improve the SDC in the vertical configuration. A maximum SDC of 92 % is observed in vertical configuration without the application of heating pulse. The unsymmetric loading of the bridges in hanging configuration results in high pre-strain dependence of the SDC behavior. The unsymmetric pre-straining of the bridges does not exist in the horizontal configuration and therefore it is preferred over hanging configuration.

6.2 Spiral Device

The spiral device is micromachined by laser cutting from NiTi one-way SMA foil of 30 µm. The device is tested under quasi-stationary condition along out-of-plane direction at a strain rate of 0.5 mm/s. The resulting force-displacement behavior is indicated in Fig. 6.15(a). The spiral device attains a large stroke of about 5 mm with a force of a few tens of millinewtons. By the application of continuous current, the device stiffness increases rapidly until the temperature of the entire spiral device is above austenite transformation temperature which is observed for a continuous current of 0.6 A as shown in Fig. 6.15(b) . At this temperature the entire spiral device has a temperature above 55 °C. Apparently, the spiral device has a predominant elastic behaviour enclosing a small hysteresis. The device undergoes almost complete strain recovery upon unloading even under no current condition. The hysteresis decreases at high continuous currents.

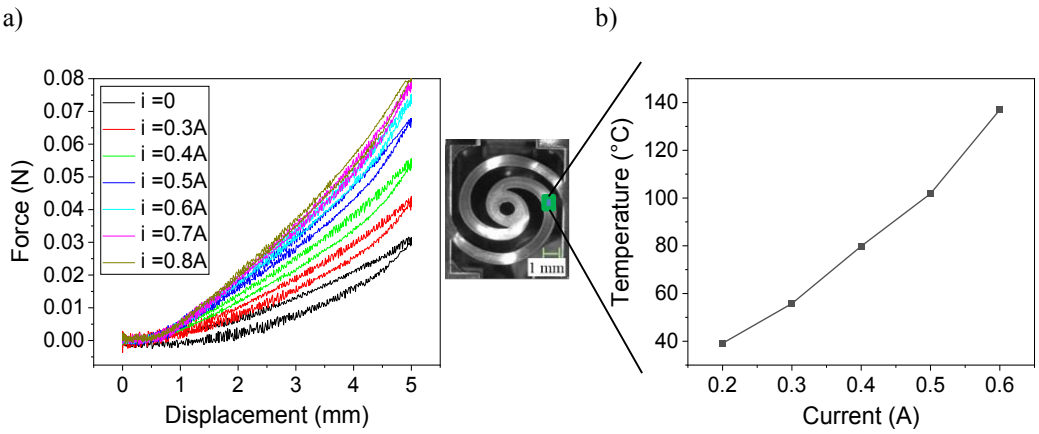

Figure 6.15: The force-displacement behavior of spiral device at a loading rate of 0.5 mm/s under various continuous heating currents (a) and the temperature on the spiral device at various continuous heating current is plotted in (b).

6.2.1 Free Oscillation Testing of Spiral Damper Device

The spiral damper device consists of two spiral devices antagonistically attached to a mass of 1.3 g at the center. The mass movement is along the horizontal direction, thereby avoiding the pre-displacement of the spiral devices arising from the mass under the action of gravity. The pre-displacement of the spiral devices is adjusted using spacers. The free oscillation test-setup of the spiral damper device is shown in Fig. 6.16. An electromagnet is used to excite the mass and the position of the electromagnet is adjusted using a micrometer head. Upon de-energizing the electromagnet, the mass oscillates and the mass movement is captured using a laser displacement sensor. The current pulses are applied at terminals V1 and V2 to enhance the damping performance.

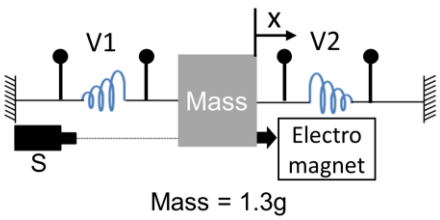

Figure 6.16: Schematic of the freee oscillation test setup of spiral damper device. S- laser displacement sensor, V1, V2- terminals for current pulse, X- mass displacement

The behavior of SDC with respect to pre-displacements at various loading amplitudes under the application of current pulse is shown in Fig. 6.17. A current pulse of 1.5 A is applied for a time duration of 50 ms when the mass moves 0.3 mm after the release from the electromagnet. SDC has a linear behavior with respect to the pre-displacement for a fixed loading amplitude due to the predominantly elastic behavior of the spiral devices. By the increase of pre-displacement, the SDC reduces due to an increase in the device stiffness. An increase in loading amplitude increases the SDC owing to the increase of

spiral device stiffness with the application of current pulse. A maximum SDC of 82% is observed under no pre-strain condition for a maximum loading amplitude of 2 mm. Even though spiral device shows no significant hysteretic behavior, a high SDC is observed in the spiral damper device. This is due to the antagonistic configuration of the two spiral device where one device undergoes loading when other is unloading thereby reducing the oscillation amplitude.

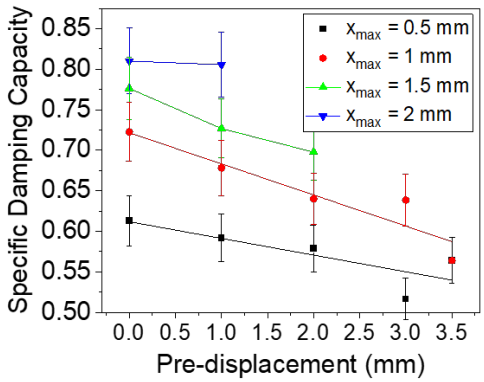

Figure 6.17: SDC vs pre-displacement of the spiral device at various loading amplitudes under the application of heating pulse.

The free-oscillation behavior of the mass is fitted with exponential function to estimate the behavior of damping ratio by using the general fitting function of

$$A_0 + Ae^{-\zeta\omega_n t}(cos(\omega_d t + \Phi)) \qquad \omega_n = \frac{\omega_d}{\sqrt{1-\zeta^2}} \tag{6.1}$$

a) No current pulse

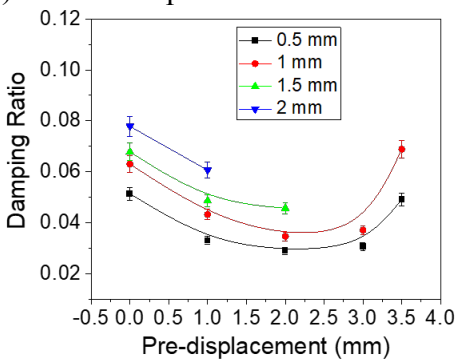

b) With current pulse

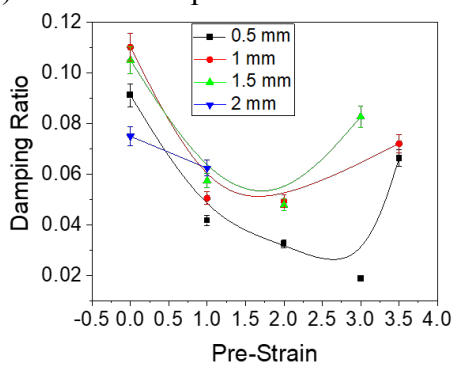

Figure 6.18: Damping ratio vs pre-displacement at various loading amplitudes without (a) and with the application of current pulse (b).

Fig. 6.18 indicates the effect of current pulse on damping ratio, ζ, estimated using Eqn. 6.1. Without application of current pulse, the damping ratio increases with increase in loading amplitues as shown in Fig. 6.18(a). By increasing pre-displacement, the damping ratio decreases due to the increase in stiffness of the spiral damper device. At pre-displacement above 3 mm an increasing behaviour in damping ratio is observed indicating additional dissipation mechanism. Even though, the behaviour of spiral device is predominantly elastic, at high pre-displacements, there is a possibility of localized re-orientation of martensite phases at regions of high stress. The softening effect associated with the martensite re-orientation is considered to be reponsible for the increase of damping ratio at high pre-displacements.

The effect of heating pulse on the damping ratio is shown in Fig. 6.18(b). The damping ratio is increased by the application of current pulse for loading amplitudes up to 1.5 mm. For a loading amplitude of 2 mm, no significant improvement in the damping ratio is observed by the application of current pulse. Since a high SDC behavior is observed for the loading amplitude of 2 mm under no pre-displacement condition as shown in Fig. 6.17, the oscillation amplitude reduction occurs gradually after first cycle. The enhancement in low amplitude oscillation is due to the increase in stiffness of the spiral damper device by the application of current pulse. The increase in damping ratio at high pre-displacement arises from the restoring force due to phase transformation.

In summary, the spiral devices are predominantly elastic devices, sensitive to excitation forces of a few millinewtons. The reorientation of martensite occurs only at localized regions of high stress concentration resulting in low energy dissipation through hysteresis. The stiffness change associated with the heating pulse is exploited to achieve high SDC. The spiral device is suitable for vibration damping of proof mass of a few grams with 1 mm wide spiral structures. Besides, the fabrication complexity is reduced due to high feature sizes.

6.3 Vibration Control using SMA Strips

The actuation property of SMA devices owing to one-way shape memory effect offers the possibility to use them for vibration control applications. Fig. 6.19(a) shows the vibration control test-setup with a mass of 3.5 g moving on a linear guidance. Two SMA strips, each of 1 mm width, are attached to the mass at an angle, θ, of 75° at unstrained condition. The test-setup is given a harmonic excitation using a linear actuator. The instantaneous position of the mass is tracked using a laser displacement sensor (S). The tracking signals from the laser displacement sensor are compared with the initial reference position of the mass using a microcontroller. An on/off control is implemented in microcontroller to enable the counteracting current pulses on terminals V1 or V2 to actuate the respective SMA strip. When the mass moves along positive direction, then

current pulse is applied along terminal V1 to bring it back to the reference position. Similarly, the current pulse along V2 counteracts the mass movement along negative direction. The corresponding closed loop control is represented in Fig. 6.19 (b). The frequency of external excitation (Exc) is below 1 Hz which is far below the resonance region of the system as represented in Fig. 6.19 (c).

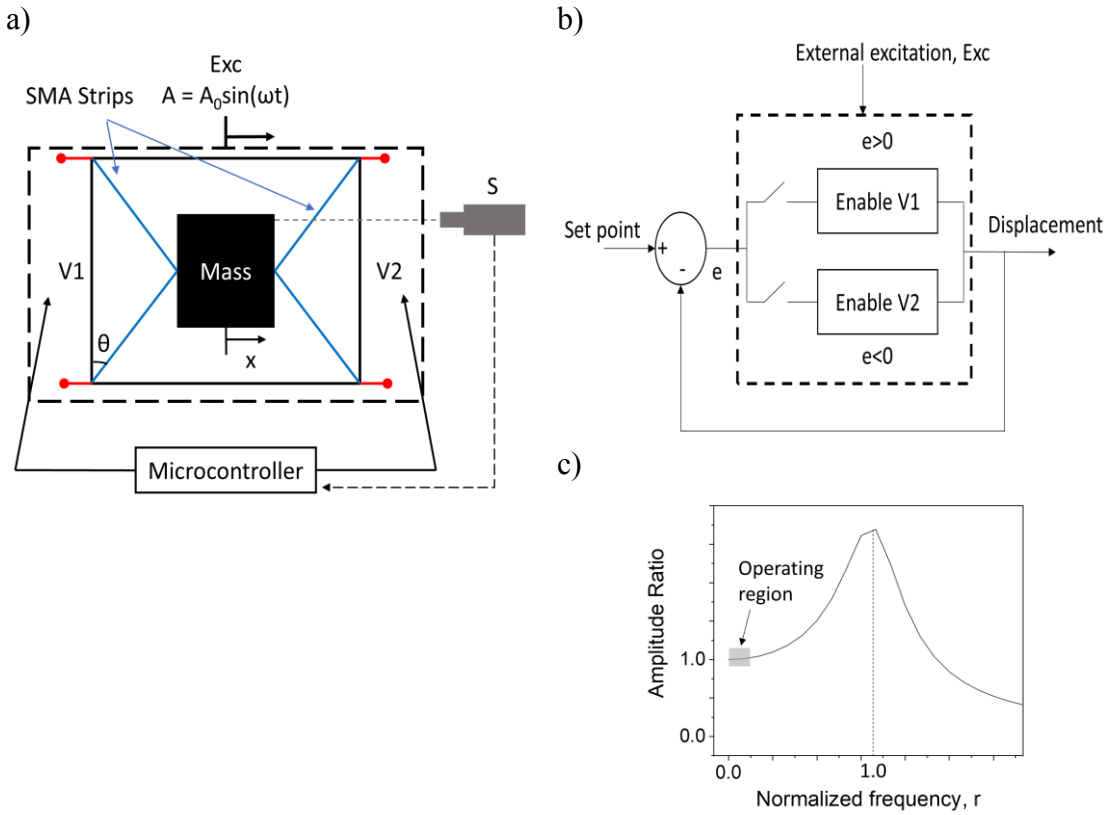

Figure 6.19: Schematic of vibration control test-setup using SMA strips (a). The excitation is introduced by a linear actuator. Exc - harmonic excitation from linear actuator, A – excitation amplitude, S - laser displacement sensor, V1,V2 - terminals for current pulse, x - mass displacement, θ – angle of the strips under no prestrain condition. The equivalent closed loop control is represented in (b). Based on the instantaneous position of the mass, either V1 or V2 are triggered to enable the corresponding SMA strips. The frequency of external excitation is far below the resonance region, below 1 Hz (c).

The mass movement under harmonic excitation of 0.067 Hz and 0.4 Hz is shown in Fig. 6.20. The peak to peak excitation amplitude is 400 µm. At low excitation frequency of 0.067 Hz, the application of current pulse stabilizes the mass within a peak to peak amplitude of 240 µm. The vibration control is less effective for an excitation frequency of 0.4 Hz and no significant amplitude reduction is observed. The high cooling time (about 1.3 s) of SMA strips hinders the effective mass stabilization using on/off control. The response time of the SMA strip increases if the counteracting strip is not cooled below the martensite finish temperature.

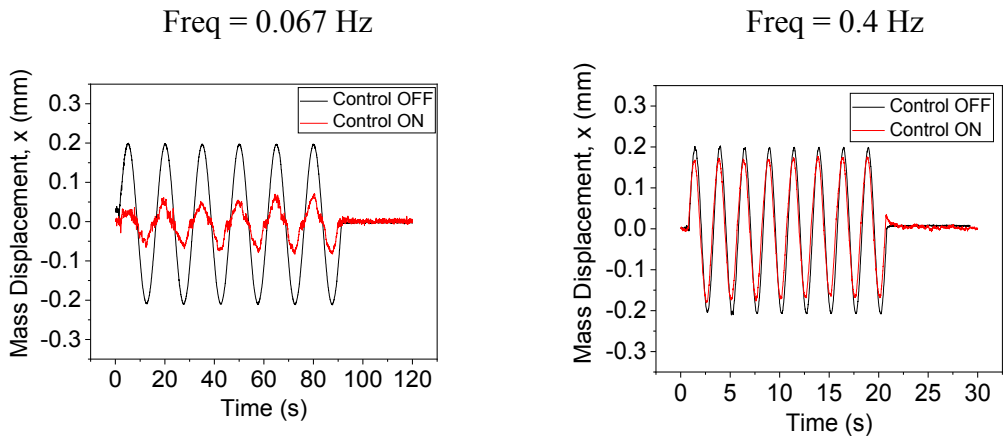

Figure 6.20: The mass movement under excitation frequencies of 0.067 Hz and 0.4 Hz.

The amplitude reduction in the movement of mass achieved using on/off control under various harmonic excitation is indicated in Fig. 6.21. A high amplitude reduction of about 60% is observed at an excitation frequency of 0.067 Hz. By increasing the excitation frequency, the high cooling time of the SMA strips results in less effective vibration control operation. For the frequencies of 0.8 and 1 Hz, the amplitude reduction is below 5%.

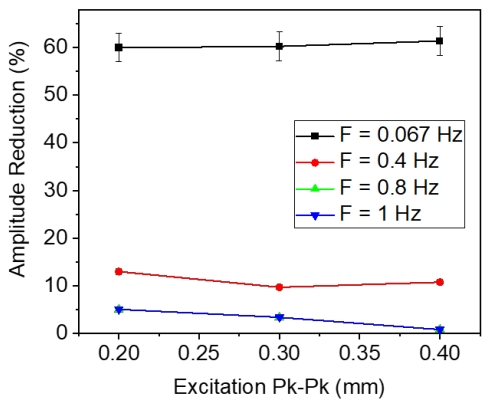

Figure 6.21: Amplitude reduction vs excitation amplitude behaviour for SMA strips under various excitation frequencies.

6.4 Vibration Control using Folded Beam

A folded beam device is fabricated by laser cutting from a NiTi one-way foil of 100 µm thickness. The quasi-stationary behavior of the folded beam device under two different loading conditions is shown in Fig. 6.22. The folded beam device accommodates large in-plane displacement of 2 mm at a loading force of about 0.45 N. The strain recovery is obtained by heating above austenite finish temperature. At high loading rates, the self-heating phenomenon results in an upward shift of the quasi-stationary behavior.

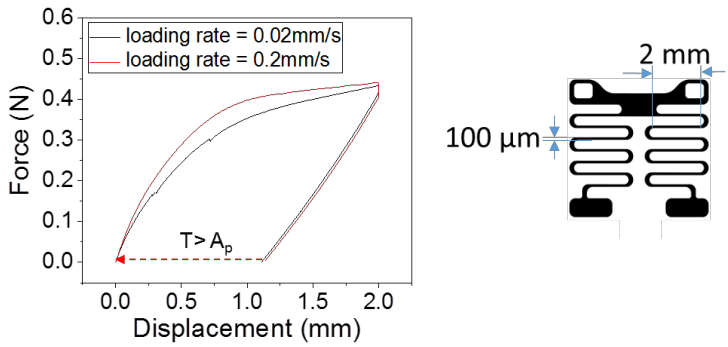

Figure 6.22: The quasi-stationary behavior of the folded beam device along in-plane direction.

6.4.1 Test-Setup for Folded Beam Device

The vibration control test setup using folded beam devices is indicated in Fig. 6.23. A mass of 3.5 g moving on a linear guidance is connected to two folded beam devices. The folded beams are pre-displaced in order to obtain an actuation stroke of 1 mm. Harmonic excitation is introduced using a linear actuator. Based on the position of the mass, the counteracting folded beams are activated to stabilize the mass against harmonic excitation. The on/off control is implemented using a microcontroller as explained in section 6.3.

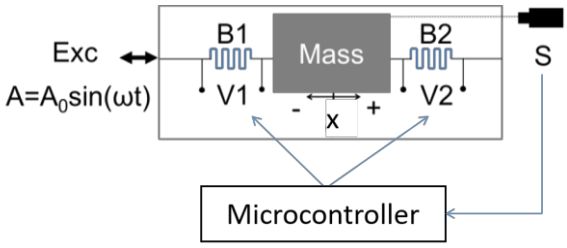

Figure 6.23: Vibration control test-setup using folded beam devices.

The vibration control operation is illustrated in Fig. 6.24. The mass position during harmonic excitation is compared with respect to its reference position. The starting position before applying the harmonic excitation is taken as the reference position. When the mass moves along positive x direction, current pulse is applied through the terminal V1 to activate the folded beam B1. The actuation of B1 brings the mass back to the reference position. B1 is active until the mass crosses the reference position and starts to move along negative x direction. I9mmediately, current pulse applied on B1 is disabled and current pulse is applied through the terminal V2 to activate B2. Therefore, when the mass is close to the reference position, multiple switching operations occurs at terminals V1 and V2. The closed loop control of this system is same as mentioned in Fig. 6.19 (b). The frequency of external excitation (Exc) is less than 1 Hz, far below the eigenfrequency of the system.

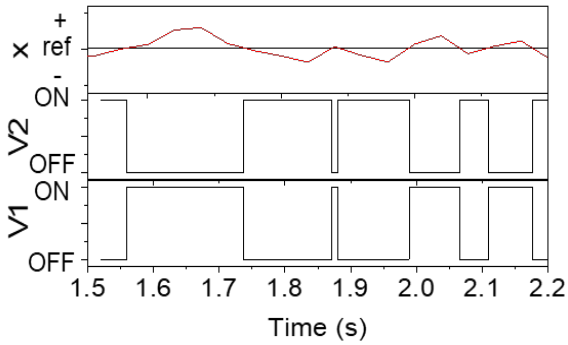

Figure 6.24: Illustration of vibration control operation.

The movement of the mass for a peak excitation amplitude of 0.5 mm and frequency of 0.067 Hz is shown in Fig. 6.25(a). By the active on/off based control, the mass is stabilized within a peak to peak oscillation amplitude of 170 µm. The behavior of oscillation amplitude reduction at various excitation amplitude and frequencies are shown in Fig. 6.25(b). For an excitation frequency of 0.067 Hz, high amplitude reduction above 75% is observed. The peak amplitude reduction of 83% is observed for excitation amplitudes of 0.8 and 1 mm. At excitation frequency of 0.4 Hz, no significant oscillation amplitude reduction is observed at high excitation amplitudes owing to the high cooling time of the SMA based folded beam actuator. Therefore, while operating at low excitation frequency, e.g. 0.067 Hz, better mass stabilization is obtained. High stroke length of the folded beam actuator aided in attaining high amplitude reduction.

a) b)

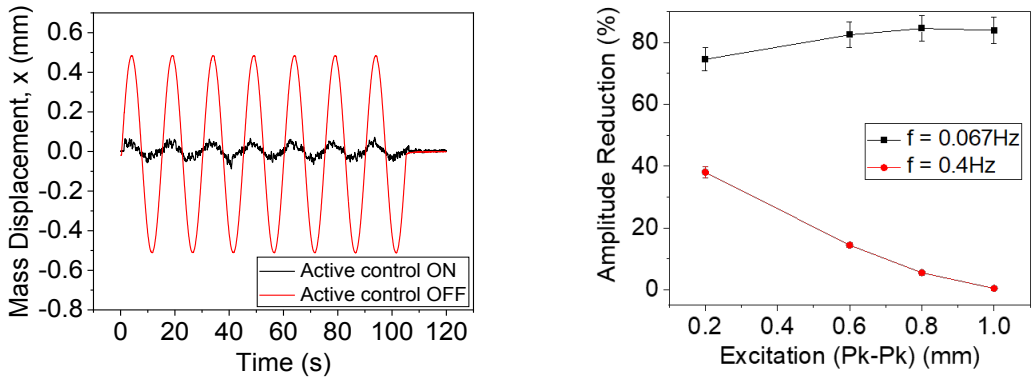

Figure 6.25: Mass displacement under harmonic excitation of 0.067 Hz with/without active vibration control is shown in (a) and the amplitude reduction vs peak to peak excitation at various frequencies is shown in (b).

The vibration control application of SMA based actuators are limited by the high cooling time of the devices. In order to extend the operating frequency, an optimal switching behavior is essential to avoid unnecessary heating of the SMA devices. A PID control is

implemented to study the performance improvement. The folded beam based vibration control system is given a staircase reference signal for the mass movement. The reference signal changes every 0.5s. The mass movement using on/off and PID based control algorithms is shown in Fig. 6.26. PID based control algorithm enables the mass to trace the reference signal better than the on/off control.

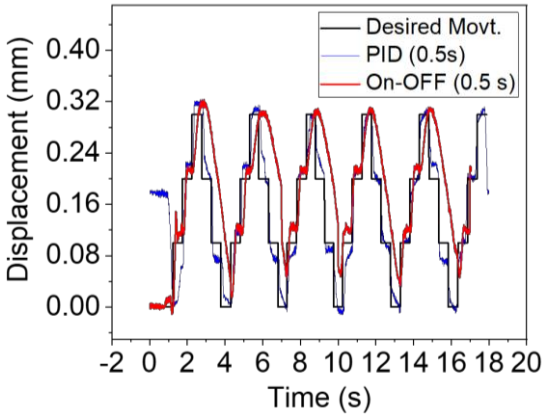

Figure 6.26: Comparison of PID and on/off based vibration control to follow a staircase signal as mass reference. The staircase signal changes in every 0.5s.

6.5 Scaling Effect on Cooling Time

The damping and vibration control performance of the SMA devices can be enhanced by improving the cooling time of the SMA device. In vibration damping application, if the combined heating and cooling time lies within the duration of each cycle, then current pulse can be applied in each oscillation cycle of shock loading. An improved settling behavior could be obtained by the application of current pulse in each oscillation cycle. In this section, the effect of device scaling on the cooling time is investigated. The bridge devices with variation in parameters like widths, lengths and thicknesses are fabricated out of steel foil to study the scaling effect on cooling time. Steel foil is used as a cost-effective alternative to SMA foil to investigate the scaling effect. By this approach, knowing the cooling time of SMA device corresponding to one of the investigated parameters enables the estimation of cooling time for all other parameters.

6.5.1 Scaling Effect in Bridge Devices

The bridge devices are manufactured out of steel by laser cutting using the same design as SMA bridge devices (discussed in section 6.1). The devices are heated with current pulse of various pulse duration to study the behavior of cooling time. The temperature at the end of the heating pulse is taken as the starting temperature to investigate the cooling time. The cooling time for thicknesses (t) of 10, 20 and 30 µm and widths of 300 and

200 µm are investigated as shown in Fig. 6.27. The temperature is estimated from the average temperature in an area of 75×75 μm^2 at the middle of the bridge. The cooling time is estimated from the time required to reach 30 °C after turning off the current pulse. The cooling time reduces with the reduction in area of cross-section of the bridge devices indicating improved thermal dissipation by convection. Considering a temperature of 80 °C, the cooling time for the bridge devices are 0.64s for t = 30 µm, w = 300µm and 0.39s for t = 10 µm and w = 300 µm. As estimated in section 6.1, the cooling time from 80 °C for SMA bridge device with t = 30 µm and w = 300 µm is 1.3s. The cooling time of SMA bridge device with t = 10 µm and w = 300 µm is about 0.79s. By further reducing the widths of the bridge devices, the cooling time could be improved. The fabrication of devices with widths less than 100 µm using laser cutting introduces large deposits of the material melts on the bridges and significant burning of the bridges. Further improvement in cooling time requires devices with widths below 100 µm. Short pulsed excimer laser based micromachining or optical lithography are suitable for fabrication of devices below 100 µm.

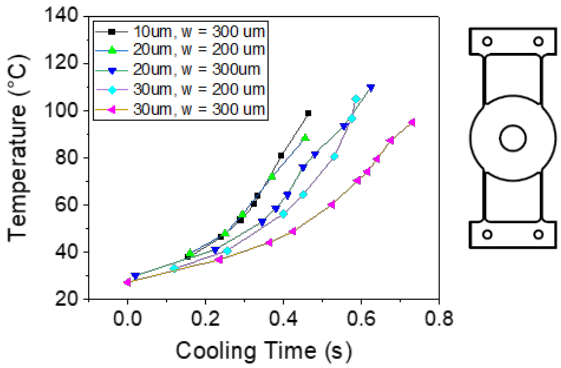

Figure 6.27: Behavior of cooling time for various starting temperatures of the bridge device made out of steel foil with the scaling of width and thickness for bridge devices.

6.5.2 Scaling Effect in Bridge Devices with Short Bridges

The cooling time of the bridge devices can be further improved by increasing the heat loss by conduction. The length of the bridge device mentioned above is scaled to one-half and the corresponding cooling behavior is indicated in Fig. 6.28. In comparison to the behavior in Fig. 6.27, the cooling time reduces almost by a factor of one-half using short bridges. The fastest cooling time of 0.18s is observed for t = 10 µm and w = 200 µm. The cooling time of SMA bridge device with comparable dimension is estimated as 0.36s.

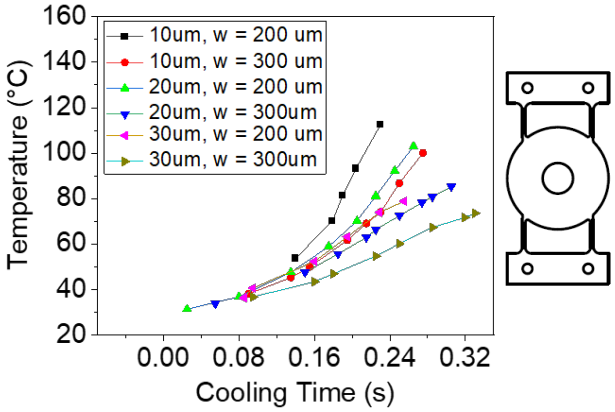

Figure 6.28: Behavior of cooling time for various starting temperatures with the scaling of width and thickness for bridge device with the bridge lengths reduced by one-half.

6.5.3 Scaling Effect in Bridge Devices with Short Bridges and Mass Holder

The bridge devices considered so far have a large mass holder platform of 10 mm diameter at the middle of the devices. The effect of mass holder in scale down is investigated by designing a mass holder of 3 mm diameter. The length of the bridges are

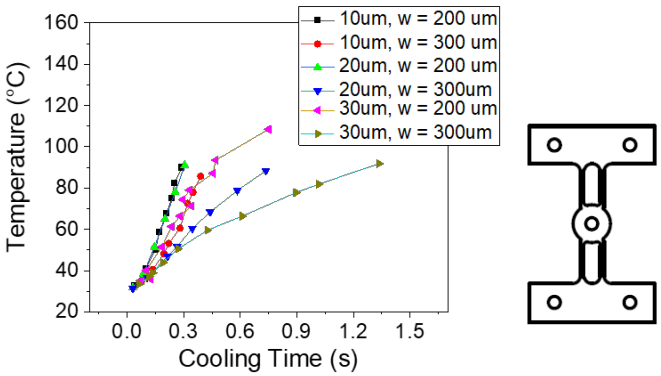

Figure 6.29: Behavior of cooling time with the scaling of width and thickness for bridge device for the bridge lengths reduced by one-half and the mass holder platform reduced to 3 mm diameter.

same as that mentioned in section 6.5.2. The cooling behavior of the bridge device with short bridges and small mass holder is shown in Fig. 6.29. A slow cooling is observed for devices with high cross-sectional areas. For devices with low cross-sectional areas, the cooling time slightly increases when compared with Fig. 6.28. The fastest cooling time of 0.24s is observed for the device with t = 10 µm and w = 200 µm. The cooling time for an SMA device under this dimension could be estimated as 0.48s representing 33% increase in cooling time by reducing the area of mass holder. This indicates that the mass holder acts as a heat sink and could contribute to faster cooling time.

7 Conclusions and Outlook

The focus of this work is to study the damping behaviour of foil based pseudoelastic and one-way Shape Memory Alloy (SMA) devices under quasi-stationary and dynamic loading conditions. Starting from a cold-rolled NiTi based SMA foil, the material characteristics, device characteristics and damping behaviour are investigated. The dynamic behaviour of SMA damper devices are investigated using free oscillation experiment. The findings related to the material and device behaviour are described in the following section and the future scope of this work is outlined.

7.1 Conclusions

Pseudoelastic material behaviour: The damping behaviour of the material is evaluated from the energy dissipation by hysteresis during loading and unloading operation. The energy dissipation depends upon loading amplitude, pre-strain and loading rate. The energy dissipation has a non-linear relation with the loading amplitude when pre-strained below 1%. For a pre-strain above 1%, the energy dissipation varies linearly with the loading amplitude. The pre-straining condition has to be optimized for each loading amplitude to allow for maximum energy dissipation.

Pseudoelastic (Passive) damper devices: The pseudoelastic dampers using bridge and spiral devices are investigated in this work. The strain recovery upon unloading allows for self-centering capability for the damper device along with high energy dissipation. The bridge based damper devices exploits phase transformation of the material to obtain high energy dissipation. The dynamic damping behaviour is investigated using free oscillation method. The specific damping capacity (SDC) of up to 72% is obtained using the bridge devices with lateral pre-strain. A further enhancement in SDC is observed using cross bridge damper device, where two bridge devices are antagonistically operating under the loading condition. The antagonistic operation enables enhanced phase transformation in both loading and unloading directions. SDC up to 92% is obtained using the cross bridge damper device. On the contrary, the spiral damper device operates predominantly in the elastic region resulting in relatively low energy dissipation.

One-way material behaviour: The material stiffness of the one-way material is drastically reduced after one loading cycle owing to the large residual strain. The large material deformation allows for high energy dissipation and the shape recovery is obtained using a heating pulse. Quick heating of the material is possible by a short current pulse of a few milliseconds. Apparently, the effective application of multiple current pulses is restricted by the cooling time of the material.

Active damper devices: The dynamic damping performance of active damper devices with bridge and spiral structures are investigated from the free oscillation behaviour. The vertical mass configuration of bridge damper device introduces an enhancement in the oscillations by the application of heating pulse. The strong out-of-plane movement of the bridge actuator upon heating pulse results in enhanced oscillation of the mass. The SDC of up to 92% is observed without the application of heating pulse whereas SDC below 73% is observed with the application of heating pulse. The vertical configuration of bridge device is not suitable for active damping application. Eliminating the effect of gravity by horizontal and hanging mass configuration in bridge damper device results in improvement of SDC with the application of heating pulse. In horizontal configuration, the SDC increases with increase in loading amplitude. A maximum SDC of 90% is obtained under the prestrain condition of 2% and loading amplitude of 1.5 mm. The test setup of the horizontal configuration is rotated by 90° to obtain the hanging configuration of the bridge device. In hanging configuration, the movement of mass is perpendicular to the direction of gravity as in the case of horizontal configuration but the mass is suspended from the bridges. The unsymmetric loading of the bridges results in a drastic pre-strain dependent behaviour during free oscillation testing condition. An optimal pre-straining between 1 and 2% is observed for hanging configuration. The optimal pre-strain is expected to vary according to the oscillating mass owing to the change in initial pre-straining condition of the bridges. A maximum SDC of about 92% is observed for a pre-strain of 2% and loading amplitude of 1.5 mm. Among the three configurations of the bridge damper device, the horizontal configuration would be the most suited for active damping application due to symmetric loading of the bridges under the mass. Besides, a drastic pre-strain dependence is also not observed on the SDC behaviour. Table 7.1 consolidates the max SDC of both pseudoelastic and one-way bridge damper devices.

Table 7.1: Comparison of max SDC of bridge damper devices

Pseudoelastic damper devices	
Devices	**Max SDC (%)**
Bridge device with lateral pre-strain	72
Cross bridge device	92
One-way SMA damper devices (with heating pulse)	
Bridge damper horizontal config.	90
Bridge damper hanging config.	92

The spiral damper device under antagonistic operation demonstrated SDC up to 82% with the application of heating pusle. The SDC increases with the loading amplitude due to the stiffness enhancement in the direction counteracting to mass movement by the heating pulse. The increase in pre-displacement results in a reduction in SDC. At pre-displacement above 2 mm, there is an increase in the damping ratio where as the SDC

decreases indicating a reduction in low amplitude oscillation with the application of heating pulse. The enhanced actuation force of the spiral device at high pre-displacement is responsible for reduced low amplitude oscillation. The spiral damper device is suitable for active damping applications involving small masses up to a few grams.

Collaborative simulation model of SMA: The experimentally determined material parameters are utilized by the project partner to develop the simulation model of SMA which is capable of predicting both macroscopic and mesoscopic SMA behaviour under various loading conditions. The model predicted the pre-strain dependence of energy dissipation for various loading amplitudes [111]. A drift in the stress-strain behaviour is observed in pseudoelastic material under harmonic loading near to the resonance condition arising due to the accumulation of martensite phases [112].

Active vibration control: The actuation of one-way SMA is exploited to implement vibration control of a proof mass, moving on a linear guidance, using two counteracting SMA actuators. The stabilization of the proof mass is only effective when excited within the stroke length of the actuator. The vibration control using two SMA strips actuated along the out-of-plane direction stabilized the proof mass against harmonic excitation by reducing the excitation amplitude by 60%. An effective stroke length of about 0.5 mm is observed after pre-straining to about 2.5%. An increased effective stroke length of about 1 mm is obtained using folded beam actuator. A high amplitude reduction of 83% is achieved under harmonic loading condition. Both strip and folded beam actuation is less effective above 0.8 Hz due to the high cooling time of the actuators. A further enhancement in vibration control requires design optimization for fast cooling and control optimization to minimize the heating pulse application on the actuators.

7.2 Outlook

The observations and understandings gained through this work could foster further research in the development of passive and active dampers using shape memory alloy. At material level, a deeper understanding of the frequency based material behavior is necessary to accurately model and predict the material and device behavior under various loading conditions. A temperature controlled testing environment with loading frequencies up to a few tens of Hz will provide more insight about the global material behavior from the force-displacement behavior. The local strain and temperature profiles measurement using high speed DIC and IR thermography will reveal the nature of material transformation under high frequency loading conditions. Besides, a quantitative information about martensite accumulation, observed in simulation, could be obtained.

In the device level operation, apart from either passive or active operation, the damping performance of the combination of these dampers have to be further investigated. Hybrid dampers, combining both active and passive SMA devices, could effectively utilize the

self-centering feature of the passive device and tunable damping property of the active device. The possibility of damping performance improvement by stiffness modulation in pseudoelastic damper device using heating pulse has to be further studied.

In damping applications using pseudoelastic SMA devices, an adaptive variation of pre-straining during the loading condition will be very effective to keep the device under optimal damping condition. During the shock loading of the SMA damper devices, there are a lot of oscillation in the elastic region of the SMA. Adjusting the pre-strain facilitates quick dissipation of elastic energy through phase transformation. A linear actuator for pre-straining along in-plane direction of the damper device would be effective in reducing the oscillations arising from shock loading along out-of-plane direction.

The active damping performance could be further improved using optimized control strategy for the heating pulse and reducing the cooling time of the damper device. In the control of SMA actuation, the practical feedback parameters are displacement, velocity or acceleration. The measurement of stress and temperature in miniature SMA actuators are rather challenging in a dynamic loading condition. Besides, the behavior of SMA is significantly affected by ageing. Therefore, a robust control method with self-calibration and parameter adaptation for the heating pulse are essential. By optimal heating pulse the operation frequency of the SMA actuator could be extended to a few Hz. A further enhancement in operation frequency to about 10 Hz requires a faster cooling of SMA actuators. The film based SMA actuators have the possibility of faster cooling by scaling down the physical dimensions of the actuators.

The SMA actuators are prospective for multi-DoF vibration damping and control application. The rotational and translational DoFs allow for 6 axis stabilization of proof mass using SMA actuators. The design of actuator is crucial while designing a multi-DoF stabilizing platform. The SMA bridge actuators are not so suitable for multi-DoF stabilization due to its high stiffness and low stroke length along in-plane direction. The folded beam actuator has the advantage of large stroke and can support a proof mass of a few tens of grams. An optimized design of folded beam actuator to facilitate faster cooling time could be used as the actuator for multi-DoF stabilizing platforms.

Acknowledgement

The journey during the research was made memorable, exciting and productive by the support of many people. I would like to thank each one of them for their effective contribution.

First of all, I would like to express profound gratitude to Prof. Dr. Manfred Kohl for providing me with the oportunity to work on this interesting and challenging research topic and guiding me with effective suggestions and deeper insight in this topic. Prof. Kohl informed me about the reputed international conferences in this domain and supported for my participation in it. I am also grateful to the efforts of Prof. Kohl in proof reading the manuscripts. Next, I thank Prof. Dr. Thomas Sattel for his kind acceptance to co-referee this research and supporting for a collaborative research.

I thank Dr. Frank Wendler, the principal investigator of the project, for the valuable suggestions related to experimental testing conditions. I thank and acknowledge the efforts of Shahabeddin Ahmadi for ensuring a close collaboration during this work through effective discussion to plan experiments for material parameter identification. I owe thanks to Florian Brüderlin for the insightful discussions about test setups and support in lab maintenance and milling operation. I specially thank Sanaz Rastjoo, Randy Fechner, Joel Joseph, Xi Chen and Lena Seigner for keeping a very lively environment within the research group. I thank and acknowledge Dr. Marcel Gültig, Dr. Hinnerk Ossmer and Dr. Christof Megnin of Memetis GmbH for the informative technical discussions, laser micromachining of the samples and introducing to fabrication procedure using optical lithography for SMA. I thank Dr. Klaus Feit for providing a detailed insight about DSC equipment and measuring procedure. I appreciate the efforts of Bachelor/Master students: Adina Händel, Carina Ludwig, Akash Sharma and Aditya Shah.

I am grateful to Heike Fornaiser for the support in fabrication of devices and etching procedures, Alexandra Moritz and her team for the manufacturing of test stage components and Giuseppe Papagno for the manufacturing of ceramic parts. I am thankful to Nina Giraud for helping in ordereing the components, Dr. Markus Guttmann, Birgit Hübner and Deski Beri for assisting in the etching operation and solution preparation, Sagar Wadhwa and Ronald Kampmann for the laser cutting of samples.

This work could not be fulfilled without support of my family. I am thankful to my dear wife Riya for her constant support and understanding which enabled me with greater work flexibility. I express heartfelt gratitude to my parents, Late Prof. Jacob Sebastian and Lizy

Jacob, for their invaluable care and guidance in my life journey. I thank my siblings, Arun and Keerthi, and their families for the support and encouragement.

I express my gratitude to DFG for funding this research as part of priority programme – SPP 1897 and appreciate the contribution of all other research groups within this programme for the friendly discussions and knowledge sharing at ‚doktorandentreffen‘ and ‚Jahrestreffen‘.

Bibliography

[1] Shabana AA. Theory of vibration: an introduction. Springer International Publishing, Cham, Switzerland, 2018. DOI: 10.1007/978-3-319-94271-1.

[2] Pérez-Díaz JL, Valiente-Blanco I, Cristache C. Z-Damper: a new paradigm for attenuation of vibrations. Machines. 2016 Jun;4(2):12. DOI: 10.3390/machines4020012.

[3] A. Preumont, Vibration Control of Active Structures, vol. 246. Springer International Publishing, Cham, Switzerland, 2018. DOI: 10.1007/978-3-319-72296-2.

[4] Chung, D.D.L. Review: Materials for vibration damping. Journal of Materials Science 36, 5733–5737 (2001). DOI: 10.1023/A:1012999616049.

[5] Ghareeb N, Farhat M. Smart Materials and Structures: State of the Art and Applications. Nano Res. Appl. 2018;4:1-5. ISSN 2639-9466.

[6] D. C. Lagoudas, Shape Memory Alloys: modeling and engineering applications. Springer-Verlag, New York, US, 2008. DOI: 10.1007/978-0-387-47685-8.

[7] Yang J. Vibration analysis on multi-mesh gear-trains under combined deterministic and random excitations. Mechanism and Machine Theory. 2013 Jan 1;59:20-33. DOI: 10.1016/j.mechmachtheory.2012.08.005.

[8] A. Sinha, Vibration of Mechanical Systems, Cambridge University Press, Cambridge, UK, 2010. ISBN 978-0-521-51873-4.

[9] Harris, Cyril M., and Allan G. Piersol. Harris' shock and vibration handbook. Vol. 5. New York: McGraw-Hill, 2002. ISBN 0-07-137081-1.

[10] C. De Silva, Vibration damping, control, and design. 2007, CRC press, Boca Raton, Florida. ISBN-13:978-1-4200-5321-0.

[11] Zener C. Internal friction in solids. Proceedings of the Physical Society. 1940;52(1):152. DOI: 10.1088/0959-5309/52/1/322.

[12] Akay A., Carcaterra A. Damping Mechanisms. In: Hagedorn P., Spelsberg-Korspeter G. (eds) Active and Passive Vibration Control of Structures. CISM International Centre for Mechanical Sciences, vol 558. Springer, Vienna, 2014. DOI: 10.1007/978-3-7091-1821-4_6.

[13] Zener C. Internal friction in solids II. General theory of thermoelastic internal friction. Physical review. 1938 Jan 1;53(1):90. DOI: 10.1103/PhysRev.53.90.

[14] Li Y, He Y, Liu Z. A viscoelastic constitutive model for shape memory polymers based on multiplicative decompositions of the deformation gradient. International

Journal of Plasticity. 2017 Apr 1;91:300-317. DOI: 10.1016/j.ijplas.2017.04.004.

[15] He Y, Guo S, Liu Z, Liew KM. Pattern transformation of thermo-responsive shape memory polymer periodic cellular structures. International Journal of Solids and Structures. 2015 Oct 1;71:194-205. DOI: 10.1016/j.ijsolstr.2015.06.022.

[16] Dos Reis RP, Silva PC, Senko R, Silva AA, De Araújo CJ. Methodology for the estimation of material damping as applied to pseudoelastic shape memory alloy mini-springs. Materials & Design. 2019 Jan 5;161:124-135. DOI:10.1016/j.matdes.2018.11.012.

[17] Wolons D, Gandhi F, Malovrh B. Experimental investigation of the pseudoelastic hysteresis damping characteristics of shape memory alloy wires. Journal of Intelligent Material Systems and Structures. 1998 Feb;9(2):116-126. DOI: 10.1177/1045389X9800900205.

[18] Beards C. Engineering vibration analysis with application to control systems. Edward Arnold, London, Great Britain, 1995. ISBN: 0-340-63183-X.

[19] Liu YF, Li J, Zhang ZM, Hu XH, Zhang WJ. Experimental comparison of five friction models on the same test-bed of the micro stick-slip motion system. Mechanical Sciences. 2015;6(1):15. DOI: 10.5194/ms-6-15-2015.

[20] Zou X, Li Z, Zhao X, Sun T, Zhang K. Study on the auto-leveling adjustment vibration isolation system for the ultra-precision machine tool. In 7th International Symposium on Advanced Optical Manufacturing and Testing Technologies: Advanced Optical Manufacturing Technologies, Harbin, China, 2014 Aug 6 (Vol. 9281, p. 92812L). Proc. SPIE 9281. DOI: 10.1117/12.2069463.

[21] Ölander A. The crystal structure of AuCd. Zeitschrift für Kristallographie-Crystalline Materials. 1932 Dec 1;83(1-6):145-148. DOI: 10.1524/zkri.1932.83.1.145.

[22] Chang LC, Read TA. Plastic deformation and diffusionless phase changes in metals—The gold-cadmium beta phase. JOM.- The Journal of The Minerals, Metals & Materials Society. 1951 Jan 1;3(1):47-52. DOI: 10.1007/bf03398954.

[23] Buehler WJ, Gilfrich JV, Wiley RC. Effect of low-temperature phase changes on the mechanical properties of alloys near composition TiNi. Journal of applied physics. 1963 May;34(5):1475-1477. DOI: 10.1063/1.1729603.

[24] Pereloma E, Edmonds DV, editors. Phase transformations in steels: Diffusionless transformations, high strength steels, modelling and advanced analytical techniques, Woodhead Publishing, Cambridge, UK, 2012. ISBN: 978-1-84569-971-0.

[25] S. Miyazaki, Y. Q. Fu, and W. M. Huang, Thin film shape memory alloys: Fundamentals and device applications. Cambridge University Press, New York, 2009. ISBN: 978-0-521-88576-8.

[26] Lie ZH. Texture Development and Anisotropic Behaviour in a Ti-45Ni-5Cu (at.%) Shape Memory Alloy, Ph.D. Thesis, University of Twente, 1997. ISBN: 90-9011069-0.

[27] Miyazaki S, Kim HY. Shape Memory and Pseudoelastic Alloys. Woodhead Publishing, Cambridge, UK. 2011 Jan 1 (pp. 15-42) DOI: 10.1533/ 978085709 2625.1.15.

[28] Miyazaki S, Otsuka K. Deformation and transition behavior associated with the R-phase in Ti-Ni alloys. Metallurgical Transactions A. 1986 Jan 1;17(1):53-63. DOI: 10.1007/BF02644442.

[29] Saburi T, Tatsumi T, Nenno S. Effects of heat treatment on mechanical behavior of Ti-Ni alloys. Le Journal de Physique Colloques. ICOMAT, Leuven, Belgium, 1982 Dec 1;43(C4):C4-261. DOI: 10.1051/ jphyscol:1982435.

[30] Miyazaki S, Ohmi Y, Otsuka K, Suzuki Y. Characteristics of deformation and transformation pseudoelasticity in Ti-Ni alloys. Le Journal de Physique Colloques. ICOMAT, Leuven, Belgium, 1982 Dec 1;43(C4):C4-255. DOI: 10.1051/jphyscol:1982434.

[31] Hwang CM, Wayman CM. Compositional dependence of transformation temperatures in ternary TiNiAl and TiNiFe alloys. Scripta metallurgica. 1983 Mar 1;17(3):381-384. DOI: 10.1016/0036-9748(83)90177-1.

[32] Miyazaki S, Kimura S, Otsuka K, Suzuki Y. The habit plane and transformation strains associated with the martensitic transformation in Ti-Ni single crystals. Scripta metallurgica. 1984 Sep 1;18(9):883-888. DOI: 10.1016/0036-9748(84)90254-0.

[33] Otsuka K, Wayman CM, editors. Shape memory materials. Cambridge university press, Cambridge, UK. 1999. ISBN: 0-521-663849.

[34] Tobushi H, Kimura K, Sawada T, Hattori T, Lin PH. Recovery stress associated with R-phase transformation in TiNi shape memory alloy: properties under constant residual strain. JSME international journal. Ser. A, Mechanics and material engineering. 1994 Apr 15;37(2):138-142. DOI: 10.1299/ jsmea1993.37.2_138.

[35] Qiu Y, Young ML, Nie X. High strain rate compression of martensitic NiTi shape memory alloys. Shape Memory and Pseudoelasticity. 2015 Sep 1;1(3):310-318. DOI: 10.1007/ s40830015-0035-y.

[36] Shaw JA. Tips and tricks for characterizing shape memory alloy wire: part 1—differential scanning calorimetry and basic phenomena. Society for Experimental Mechanics- Experimental Techniques, 2008, 32(5):55–62. DOI: 10.1111/j.1747-1567.2008.00410.x.

[37] Lieberman DS, Wechsler MS, Read TA. Cubic to orthorhombic diffusionless phase change—experimental and theoretical studies of AuCd. Journal of Applied

Physics. 1955 Apr;26(4):473-484. DOI: 10.1063/1.1722021.

[38] M.S. Wechsler, D.S. Lieberman, T.A. Read, On the theory of the formation of martensite, Journal of Metals. 1953, vol. 197, pp. 1503-1515. OCLC Nummer: 35087891.

[39] Bowles JS, Mackenzie JK. The crystallography of martensite transformations I. Acta metallurgica. 1954 Jan 1;2(1):129-137. DOI: 10.1016/0001-6160(54)90102-9.

[40] Matsumoto O, Miyazaki S, Otsuka K, Tamura H. Crystallography of martensitic transformation in Ti Ni single crystals. Acta Metallurgica. 1987 Aug 1;35(8):2137-2144. DOI: 10.1016/0001-6160(87)90042-3.

[41] Bhattacharya K. Self-accommodation in martensite. Archive for Rational Mechanics and Analysis. 1992 Sep 1;120(3):201-244. DOI: 10.1007/BF00375026.

[42] Shayanfard P, Kadkhodaei M, Safaee S. Proposition of R-phase transformation strip in the phase diagram of Ni-Ti shape memory alloy using electromechanical experiments. Journal of Intelligent Material Systems and Structures. 2017 Nov;28(19):2757-2768. DOI: 10.1177/1045389X17698587.

[43] Wilson SA, Jourdain RP, Zhang Q, Dorey RA, Bowen CR, Willander M, Wahab QU, Al-hilli SM, Nur O, Quandt E, Johansson C. New materials for micro-scale sensors and actuators: An engineering review. Materials Science and Engineering: R: Reports. 2007 Jun 21;56(1-6):1-29. DOI: 10.1016/j.mser.2007.03.001.

[44] Nespoli A, Besseghini S, Pittaccio S, Villa E, Viscuso S. The high potential of shape memory alloys in developing miniature mechanical devices: A review on shape memory alloy mini-actuators. Sensors and Actuators A: Physical. 2010 Mar 1;158(1):149-160. DOI: 10.1016/j.sna.2009.12.020.

[45] Jani JM, Leary M, Subic A, Gibson MA. A review of shape memory alloy research, applications and opportunities. Materials & Design (1980-2015). 2014 Apr 1;56:1078-1113. DOI: 10.1016/j.matdes.2013.11.084.

[46] Zainal MA, Sahlan S, Ali MS. Micromachined shape-memory-alloy microactuators and their application in biomedical devices. Micromachines. 2015 Jul;6(7):879-901. DOI: 10.3390/mi6070879.

[47] Kohl M, Krevet B, Just E. SMA microgripper system. Sensors and Actuators A: Physical. 2002 Apr 1;97:646-652. DOI: 10.1016/S0924-4247(01)00803-2.

[48] Otsuka K, Ren X. Recent developments in the research of shape memory alloys. Intermetallics. 1999 May 1;7(5):511-528. DOI: 10.1016/S0966-9795(98)00070-3.

[49] Machado LG, Savi MA. Medical applications of shape memory alloys. Brazilian journal of medical and biological research. 2003 Jun;36(6):683-691. DOI: 10.1590/S0100-879X2003000600001.

[50] Morgan NB. Medical shape memory alloy applications—the market and its

products. Materials Science and Engineering: A. 2004 Jul 25;378(1-2):16-23. DOI: 10.1016/j.msea.2003.10.326.

[51] Han YL, Li QS, Li AQ, Leung AY, Lin PH. Structural vibration control by shape memory alloy damper. Earthquake engineering & structural dynamics. 2003 Mar;32(3):483-494. DOI: 10.1002/eqe.243.

[52] Duerig T, Pelton A, Stöckel D. An overview of nitinol medical applications. Materials Science and Engineering: A. 1999 Dec 15;273:149-160. DOI: 10.1016/s0921-5093(99)00294-4.

[53] Bengisu, M. and Ferrara, M., 2018. Materials that move: smart materials, intelligent design. Springer International Publishing, Cham, Switzerland. ISBN 978-3-319-76889-2.

[54] Yan B, Wang K, Hu Z, Wu C, Zhang X. Shunt damping vibration control technology: A review. Applied Sciences. 2017 May;7(5):494. DOI: 10.3390/app7050494.

[55] Marakakis K, Tairidis GK, Koutsianitis P, Stavroulakis GE. Shunt piezoelectric systems for noise and vibration control: A review. Frontiers in Built Environment. 2019 May 15;5:64. DOI: 10.3389/fbuil.2019.00064.

[56] De Marneffe B, Preumont A. Vibration damping with negative capacitance shunts: theory and experiment. Smart Materials and Structures. 2008 Apr 8;17(3):035015. DOI: 10.1088/0964-1726/17/3/035015.

[57] Lim SC, Choi SB. Vibration control of an HDD disk-spindle system utilizing piezoelectric bimorph shunt damping: I. Dynamic analysis and modeling of the shunted drive. Smart materials and structures. 2007 May 15;16(3):891. DOI: 10.1088/0964-1726/16/3/039.

[58] Lim SC, Choi SB. Vibration control of an HDD disk-spindle system using piezoelectric bimorph shunt damping: II. Optimal design and shunt damping implementation. Smart materials and structures. 2007 May 15;16(3):901. DOI: 10.1088/0964-1726/16/3/040.

[59] Sun H, Yang Z, Li K, Li B, Xie J, Wu D, Zhang L. Vibration suppression of a hard disk driver actuator arm using piezoelectric shunt damping with a topology-optimized PZT transducer. Smart Materials and Structures. 2009 May 6;18(6):065010. DOI: 10.1088/0964-1726/18/6/065010.

[60] Paikaw E, Vichienchom K, Pojprapai S. Piezoelectric microactuator testing using heat-assisted capacitance measurement. In 2016 13th International Conference on Electrical Engineering/Electronics, Computer, Telecommunications and Information Technology (ECTI-CON) 2016, Chiang Mai, Thailand, Jun 28 (pp. 1-4). IEEE. DOI: 10.1109/ECTICon.2016.7561439.

[61] Shevtsov S, Soloviev A, Acopyan V, Samochenko I. Helicopter rotor blade vibration control on the basis of active/passive piezoelectric damping approach. In

Proc. on tne 4th Int. Conf. Physics and Control (PhysCon-2009) September, 1- 4 2009, Catania, Italy, pp. 9.

[62] Fairbairn MW, Moheimani SR, Fleming AJ. Improving the scan rate and image quality in tapping mode atomic force microscopy with piezoelectric shunt control. In 2011 Australian Control Conference, Melbourne 2011, Nov 10 : 26-31. IEEE Xplore. ISBN: 978-0-85825-884-6

[63] Alaluf D, Mokrani B, Wang K, Preumont A. Damping of piezoelectric space instruments: application to an active optics deformable mirror. CEAS Space Journal. 2019 Dec 1;11(4):543-551. DOI: 10.1007/s12567-019-00278-4.

[64] Takács G. Smart Materials in Active Vibration Control. InModel Predictive Vibration Control 2012 (pp. 65-103). Springer, London. DOI: 10.1007/978-1-4471-2333-0_3

[65] Deng Z, Dapino MJ. Review of magnetostrictive materials for structural vibration control. Smart Materials and Structures. 2018 Oct 23;27(11):113001. DOI: 10.1088/1361-665X/aadff5.

[66] Clark AE, Wun-Fogle M, Restorff JB, Lograsso TA. Magnetostrictive properties of Galfenol alloys under compressive stress. Materials transactions. 2002;43(5):881-886. DOI: 10.2320/matertrans.43.881.

[67] Scheidler JJ, Dapino MJ. Mechanically induced magnetic diffusion in cylindrical magnetoelastic materials. Journal of Magnetism and Magnetic Materials. 2016 Jan 1;397:233-239. DOI: 10.1016/j.jmmm.2015.08.074.

[68] Kellogg RA, Flatau A, Clark AE, Wun-Fogle M, Lograsso T. Quasi-static transduction characterization of galfenol. In ASME International Mechanical Engineering Congress and Exposition , Washington, DC, USA. 2003 Jan 1 (Vol. 37076, pp. 273-280). DOI: 10.1115/IMECE2003-43140.

[69] Kellogg R, Flatau A. Experimental investigation of Terfenol-D's elastic modulus. Journal of Intelligent Material Systems and Structures. 2008 May;19(5):583-595. DOI: 10.1177/1045389X07077854.

[70] Mahapatra DR, Gopalakrishnan S, Balachandran B. Active feedback control of multiple waves in helicopter gearbox support struts. Smart materials and structures. 2001 Oct 9;10(5):1046. doi: 10.1088/0964-1726/10/5/321.

[71] Hathaway KB, Clark AE, Teter JP. Magnetomechanical damping in giant magnetostriction alloys. Metallurgical and Materials Transactions A. 1995 Nov 1;26(11):2797-2801. DOI: 10.1007/BF02669638.

[72] Liu YD, Choi HJ. Electrorheological fluids: smart soft matter and characteristics. Soft Matter. 2012;8(48):11961-11978. DOI: 10.1039/C2SM26179K.

[73] Hao T. Electrorheological fluids. Advanced Materials. 2001 Dec;13(24):1847-1857. DOI: 10.1002/1521-4095(200112)13:24<1847::AID-ADMA

1847>3.0.CO;2-A.

[74] Sheng P, Wen W. Electrorheological fluids: mechanisms, dynamics, and microfluidics applications. Annual review of fluid mechanics. 2012 Jan 21;44:143-174. DOI: 10.1146/annurev-fluid-120710-101024.

[75] Wen W, Huang X, Yang S, Lu K, Sheng P. The giant electrorheological effect in suspensions of nanoparticles. Nature materials. 2003 Nov;2(11):727-730. DOI: 10.1038/nmat993.

[76] Ashtiani M, Hashemabadi SH, Ghaffari A. A review on the magnetorheological fluid preparation and stabilization. Journal of magnetism and Magnetic Materials. 2015 Jan 15;374:716-730. DOI: 10.1016/j.jmmm.2014.09.020.

[77] Kumar JS, Paul PS, Raghunathan G, Alex DG. A review of challenges and solutions in the preparation and use of magnetorheological fluids. International Journal of Mechanical and Materials Engineering. 2019 Dec 1;14(1):13. DOI: 10.1186/s40712-019-0109-2.

[78] Spaggiari A. Properties and applications of Magnetorheological fluids. Frattura ed Integrità Strutturale. 2013;7(23):48-61. DOI: 10.3221/IGF-ESIS.23.06.

[79] Muhammad A, Yao XL, Deng ZC. Review of magnetorheological (MR) fluids and its applications in vibration control. Journal of Marine Science and Application. 2006 Sep 1;5(3):17-29. DOI: 10.1007/s11804-006-0010-2.

[80] Sarkar C, Hirani H, Sasane A. Magnetorheological smart automotive engine mount. International Journal of Current Engineering and Technology. 2015;5(1):419-428. E-ISSN 2277 – 4106, P-ISSN 2347 – 5161.

[81] Bar-Cohen Y. Electroactive polymers: current capabilities and challenges. In Smart Structures and Materials 2002: Electroactive Polymer Actuators and Devices (EAPAD), San Diego, California, United States, 2002 Jul 11 (Vol. 4695, pp. 1-7). International Society for Optics and Photonics. DOI: 10.1117/12.475159.

[82] Zhao Z, Shuai C, Gao Y, Rustighi E, Xuan Y. An application review of dielectric electroactive polymer actuators in acoustics and vibration control. In Journal of Physics: Conference Series, Southampton, UK 2016 Sep (Vol. 744, No. 1, p. 012162). DOI: doi.org/10.1088/1742-6596/744/1/012162.

[83] Madden JD, Vandesteeg NA, Anquetil PA, Madden PG, Takshi A, Pytel RZ, Lafontaine SR, Wieringa PA, Hunter IW. Artificial muscle technology: physical principles and naval prospects. IEEE Journal of oceanic engineering. 2004 Nov 8;29(3):706-728. DOI: 10.1109/JOE.2004.833135.

[84] Su J, Harrison JS, St Clair T. Novel polymeric elastomers for actuation. In ISAF 2000. Proceedings of the 2000 12th IEEE International Symposium on Applications of Ferroelectrics (IEEE Cat. No. 00CH37076), Honolulu, HI, USA, 2000 Jul 21 (Vol. 2, pp. 811-814). IEEE Xplore. DOI: 10.1109/isaf.2000.942442.

[85] Kim KJ, Tadokoro S. Electroactive polymers for robotic applications. Artificial Muscles and Sensors. Springer, London, 2007. ISBN 978-1-84628-372-7.

[86] Heydt R, Kornbluh R, Eckerle J, Pelrine R. Sound radiation properties of dielectric elastomer electroactive polymer loudspeakers. In Smart structures and materials 2006: Electroactive polymer actuators and devices (eapad), San Diego, California, United States, 2006 Mar 22 (Vol. 6168, p. 61681M). Proc. SPIE 6168. DOI: 10.1117/12.659700.

[87] Bar-Cohen Y. Electroactive polymers as artificial muscles: capabilities, potentials and challenges. In Fourth International Conference and Exposition on Robotics for Challenging Situations and Environments, Albuquerque, New Mexico, United States 2000 (pp. 188-196). DOI: 10.1061/40476(299)24.

[88] Krishen K. Space applications for ionic polymer-metal composite sensors, actuators, and artificial muscles. Acta Astronautica. 2009 Jun 1;64(11-12):1160-1166. DOI: 10.1016/j.actaastro.2009.01.008.

[89] Bandopadhya D, Bhogadi DK, Bhattacharya B, Dutta A. Active vibration suppression of a flexible link using ionic polymer metal composite. In IEEE conference on robotics, automation and mechatronics, Bangkok, Thailand 2006 Jun 1 (pp. 1-6). IEEE Xplore. DOI: 10.1109/RAMECH.2006.252638.

[90] Piedboeuf MC, Gauvin R, Thomas M. Damping behaviour of shape memory alloys: strain amplitude, frequency and temperature effects. Journal of Sound and Vibration. 1998 Jul 30;214(5):885-901. DOI: 10.1006/jsvi.1998.1578.

[91] Dolce M, Cardone D. Mechanical behaviour of shape memory alloys for seismic applications 2. Austenite NiTi wires subjected to tension. International journal of mechanical sciences. 2001 Nov 1;43(11):2657-2677. DOI: 10.1016/S0020-7403(01)00050-9.

[92] Ozbulut OE, Hurlebaus S. Energy-balance assessment of shape memory alloy-based seismic isolation devices. Smart Structures and Systems. 2011 Oct 1;8(4):399-412. DOI: 10.12989/sss.2011.8.4.399.

[93] Graesser EJ, Cozzarelli FA. Shape-memory alloys as new materials for aseismic isolation. Journal of engineering mechanics. 1991 Nov;117(11):2590-2608. DOI: 10.1061/(ASCE)0733-9399(1991)117:11(2590).

[94] Wilde K, Gardoni P, Fujino Y. Base isolation system with shape memory alloy device for elevated highway bridges. Engineering structures. 2000 Mar 1;22(3):222-229. DOI: 10.1016/S0141-0296(98)00097-2.

[95] Dolce M, Cardone D, Marnetto R. Implementation and testing of passive control devices based on shape memory alloys. Earthquake engineering & structural dynamics. 2000 Jul;29(7):945-968. DOI: 10.1002/1096-9845(200007)29:7<945:: aid-eqe958> 3.0.co;2-%23.

[96] Kaur N, Kaur D. NiTiCu/AlN/NiTiCu shape memory thin film heterostructures for vibration damping in MEMS. Journal of alloys and compounds. 2014 Mar 25;590:116-124. DOI: 10.1016/j.jallcom.2013.11.052.

[97] Castellano MG, Indirli M, Martelli A, Azevedo J, Sincraian G, Tirelli D, Renda V, Croci G, Biritognolo M, Bonci A, Viskovic A. Seismic protection of cultural heritage using shape memory alloy devices—an EC funded project (ISTECH). In Proceedings of the International Post-SMiRT Conference Seminar on Seismic Isolation, Passive Energy Dissipation and Active Control of Vibrations of Structures, Cheju, Korea, August 2–25 1999 Aug 23 (pp. 417-443).

[98] Van Humbeeck J, Kustov S. Active and passive damping of noise and vibrations through shape memory alloys: applications and mechanisms. Smart materials and structures. 2005 Aug 24;14(5):S171. DOI: 10.1088/0964-1726/14/5/001.

[99] Ellis RL, Lalande F, Jia H, Rogers CA. Ballistic impact resistance of SMA and spectra hybrid graphite composites. Journal of reinforced plastics and composites. 1998 Jan;17(2):147-164. DOI: 10.1177/073168449801700205.

[100] Baz AJ, Imam K, McCoy J. Active vibration control of flexible beams using shape memory actuators. Journal of Sound and Vibration. 1990 Aug 8;140(3):437-456. DOI: 10.1016/0022-460X(90)90760-W.

[101] Calkins F, Butler G, Mabe J. Variable geometry chevrons for jet noise reduction. In12th AIAA/CEAS Aeroacoustics Conference (27th AIAA Aeroacoustics Conference), Cambridge, Massachusetts, 2006 May (p. 2546). DOI: 10.2514/6.2006-2546.

[102] Rogers CA. Active vibration and structural acoustic control of shape memory alloy hybrid composites: experimental results. The Journal of the Acoustical Society of America. 1990 Dec;88(6):2803-2811. DOI: 10.1121/1.399683.

[103] Gotthardt R, Parlinska M. Vibrational properties of adaptive polymer matrix composites with embedded shape-memory alloy wires. In Materials Science Forum 2002 (Vol. 394, pp. 475-482). Trans Tech Publications Ltd, Switzerland. DOI: 10.4028/www.scientific.net/msf.394-395.475.

[104] Kazi A, Honold M, Rimkus W, Lokner T, Baeuml M, Koepfer M. SMA Actuator for Optical Image Stabilization. In ACTUATOR 2018; 16th International Conference on New Actuators, Bremen, Germany, 2018 Jun 25 (pp. 1-4). IEEE Xplore. ISBN: 978-3-8007-4675-0

[105] Wendler F, Ossmer H, Chluba C, Quandt E, Kohl M. Mesoscale simulation of elastocaloric cooling in SMA films. Acta Materialia. 2017 Sep 1;136:105-117. DOI: 10.1016/j.actamat.2017.06.044.

[106] Inoue H, Miwa N, Inakazu N. Texture and shape memory strain in TiNi alloy sheets. Acta Materialia. 1996 Dec 1;44(12):4825-4834. DOI: 10.1016/S1359-6454(96)00120-6.

[107] Liu Y, Xie ZL, Van Humbeeck J, Delaey L. Effect of texture orientation on the martensite deformation of NiTi shape memory alloy sheet. Acta materialia. 1999 Jan 15;47(2):645-660. DOI: 10.1016/S1359-6454(98)00376-0.

[108] Williams KR, Gupta K, Wasilik M. Etch rates for micromachining processing-Part II. Journal of microelectromechanical systems. 2003 Dec;12(6):761-778. DOI: 10.1109/JMEMS.2003.820936.

[109] Braun S, Sandstrom N, Stemme G, van der Wijngaart W. Wafer-scale manufacturing of bulk shape-memory-alloy microactuators based on adhesive bonding of titanium–nickel sheets to structured silicon wafers. Journal of microelectromechanical systems. 2009 Dec 1;18(6):1309-1317. DOI: 10.1109/JMEMS.2009.2035368.

[110] Jacob K, Ahmadi S, Wendler F, Miyazaki S, Kohl M. Vibration Damping of Portable Devices by Pseudoelastic SMA Foils. In ACTUATOR 2018; 16th International Conference on New Actuators, Bremen, Germany. 2018 Jun 25 (pp. 1-5). IEEE Xplore. ISBN: 978-3-8007-4675-0.

[111] Ahmadi S, Jacob K, Wendler F, Kohl M. Shape memory alloy film damping for smart miniature systems. International Journal of Smart and Nano Materials. 2018 Jul 3;9(3):199-215. DOI: 10.1080/19475411.2018.1496953.

[112] Ahmadi S, Jacob K, Wendler F, Kohl M. Mesoscale Simulation of Shape Memory Alloy Film Damping. Proceedings in Applied Mathematics and Mechanics" (PAMM) , Munich, Germany. 2018 Dec;18(1):e201800409. DOI: 10.1002/pamm.201800409.

[113] Maia, N. Reflections on the hysteretic damping model. Shock and Vibration, 16(5), pp.529-542, 2009. DOI 10.3233/SAV-2009-0486